輔仁學誌－理工類

目　錄

FU JEN STUDIES

SCIENCE AND ENGINEERING

NO. 42, Dec. 2008

CONTENTS

Page

Diffusion Effect of p-Laplacian Operators

Mao-Sheng Chang   Shu-Cheng Lee   Chien-Chang Yen[1]

Department of Mathematics, Fu Jen Catholic University, Taipei, Taiwan

Abstract

We investigate the diffusion effect of p-Laplacian operators by numerical studies of de-noising images, phase transition diffusion systems, and spike-Layers in diffusion systems. For $p = 2$, it is the traditional Laplacian operator and the diffusion is global homogeneous. The other cases, $p > 2$, are local homogeneous.

For de-noising images, the diffusion effect of p-Laplacian operators is decreasing as the value p is increasing. For phase transition diffusion system, the result is consistent to the de-noising images and the fact is also used to explain the mechanism for de-nosing images. In the contrast to the previous two cases, the spike waves could propagate farther away from the origin when p is larger for spike-Layers in diffusion systems.

Keywords : p-Laplacian operators, de-noising images, diffusion, spike-Layer

Section 1. Introduction

The p-Laplacian operator is defined as

$$\Delta_p u = \nabla \cdot \left(\left\| \nabla u \right\|^{p-2} \nabla u \right)$$

[1] Corresponding author: Tel :886-2-2905-3547
Fax :886-2-2904-4509
E-mail address: yen@math.fju.edu.tw

with $p \neq 2$ can be used in non-Neumann fluids, in some reaction-diffusion problems as well as in flow through porous media [3]. The motivation is risen from [2], which remarks that the relation of kinetic and potential energies by Young's inequality. To study the diffusion effect of p-Laplacian operators is an essential work for the goal in the near future. The strategy of probing the diffusion effect is by investigating the behaviors in three topics: de-noising images, phase transition diffusion systems, and spike-Layers in diffusion systems.

The corresponding numerical schemes are as the follows: A simple forward explicit Euler method is used for de-noising images. For large diffusion coefficients, the explicit methods often encounter the numerical instability. We have to discrete the phase transition systems by an implicit approach and similar for the case of spike-Layers in diffusion systems. However, if the diffusion coefficients are too large, it still requires advanced studies.

This paper is organized as the following: de-noising images by p-Laplacian operators in section 2, phase transition diffusion systems in section 3, spike-Layers in diffusion systems in section 4, and section 5 gives the conclusion and discussion.

Section 2. De-nosing images by p-Laplacian operators

An image is a collection of curves with equal values. Total variation (TV) method is known as for de-noising and edge-preserving effect. p-Laplacian operators are regarded as a generalization of the TV method by taking a general L_p norm of the gradients instead of the L_1 norm. Consider an image U on the domain Ω and the total energy

$$E(U) = \int_\Omega \frac{1}{p} \|\nabla U\|^p, \quad p \geq 1.$$

The case of $p = 2$ represents the functional as traditional energy. Minimizing the energy E among suitable function spaces with appropriate boundary conditions gives the Euler-Lagrange equation

$$\nabla \cdot \left(\|\nabla U\|^{p-2} \nabla U \right) = 0.$$

A dynamical system is obtained by a direct approach

$$U_t = \nabla \cdot \left(\|\nabla U\|^{p-2} \nabla U \right),$$
$$U(0) = U_0.$$

The numerical method is the simplest explicit forward Euler method

$$\frac{U_{i,j}^{n+1} - U_{i,j}^{n}}{\Delta t} = D^- \cdot \left(\left\| D^+ U_{i,j} \right\|^{p-2} D^+ U_{i,j} \right)$$

where D^- and D^+ are the backward and forward difference operators in both directions, respectively.

A noisy Lena image is produced by the origin with one-third standard deviation noise and is used as the initial data for investigating the diffusion effect. The updating increment is less than 10% compared with the maximum intensity of the image. The number of evolution is 100. Figure 1 shows us the global homogeneous diffusion coefficients quickly blur the images. To observe the high qualities can compare the details on hair and eye-lash. The local homogeneous cases are $p=3,4,10$. It gives that the best effect for de-noising is the case $p=10$.

The shown example is an unconstraint approach. An extra condition, so called variance constraint has been used to obtain the better quality, that is,

$$I = \int_\Omega \frac{1}{2} (U - U_0)^2 dx \equiv \sigma^2$$

The corresponding Euler-Lagrangian equation obtained by Lagrangian multiplier becomes

$$\nabla \cdot \left(\|\nabla U\|^{p-2} \nabla U \right) + \lambda (U - U_0) = 0,$$
$$\lambda = -\frac{\left\langle \nabla \cdot \left(\|\nabla U\|^{p-2} \nabla U \right), (U - U_0) \right\rangle}{\|U - U_0\|^2},$$

where $\langle \bullet, \bullet \rangle$ denotes the inner product given by

$$\langle U, V \rangle = \sum_{i=1}^{N} \sum_{j=1}^{N} U_{i,j} V_{i,j},$$

and $\|U\|^2 = \langle U, U \rangle$.   The results are shown in Figure 2.

Figure 1.   The profiles at the top row are the origin (left) and the one with one-third standard deviation noise (right). The second and last row from left to right are for $p=2,3,4,10$.

Figure 2.   The top-left profile is the origin with noise. The top-right is for *p=3*. The bottom profiles are
             p=4 (left) and *p=10* (right). These results show the case of variance constraint.

The advanced approach [4] has represented *p*-Laplacian operators as Gauge coordinates are locally set such that the *v* direction is tangent to the curve of an edge and the *w* direction points in the direction of the gradient vector. The purpose of this paper is rather to see the *p*-Laplacian diffusion effect than to compare the results between the above two methods. The next section is to study phase transition diffusion in one dimension and the result could be used to explain the mechanism of the de-noising process.

Section 3. Phase transition diffusion

In paper [2], we have shown the existence of minimizer and gamma-convergence of generalized Allen-Chan functional

$$E_\varepsilon(u) = \int_\Omega \left\{ W(u(x)) + \varepsilon \| \nabla u(x) \|^p \right\} dx, \quad \text{for all } p > 1, \varepsilon > 0$$

with Neumann boundary condition and the mass constraint

$$\int_{\Omega} u(x)dx = m\,|\,\Omega\,| \quad where \quad 0 < m < 1.$$

For $p=2$, the method of Gamma-convergence was introduced by De Giorgi in the early 1970. Modica and Mortola proved it in 1970. In 1987 [5], Modica has applied the Gamma-convergence theory to solve the minimal interface problem in the Van der Waals-Cahn-Hilliard theory of phase transitions. In the process of proof in [2], it indicates the relations of the potential and kinetic energies through Young's inequality. The Euler-Lagrange equation for Allen-Chan functional is

$$\frac{W'(u(x))}{q} - \varepsilon^p \nabla \cdot \left(\left\| \nabla u(x) \right\|^{p-2} \nabla u(x) \right) = 0, \; for \; all \; x \in \Omega,$$

where $\dfrac{1}{p} + \dfrac{1}{q} = 1$. Now, we would like to see the effect of diffusion and the one-dimensional problem considered here.

$$u_t = \Delta_p u - f(u), \quad where \quad f(u) = W'(u)$$
$$u(x,0) = u_0(x), \quad x \in [0,1]$$

The implicit scheme is used for p-Laplacian operators and the explicit scheme for evaluation of reaction function.

$$\frac{u_k^{n+1} - u_k^n}{\Delta t} = \frac{\left\| D^+ u_k^n \right\|^{p-2} D^+ u_k^{n+1} - \left\| D^+ u_{k-1}^n \right\|^{p-2} D^+ u_{k-1}^{n+1}}{(\Delta x)^2} - f(u_k^n) \; in \; [0,1] \times (0,\infty)$$

The initial data is assumed there are two positive sine waves.

$$u_0(x) = 2\sin(5\pi(x - 0.2))\chi_{[0.2,0.4]}(x) + 10\sin(200\pi(x - 0.8))\chi_{[0.8,0.805]}(x)$$

The narrow one can be regarded as the noise and the wider one as real signal. The number of grid points is 512 and the stop time is 0.01. The fast diffusion is the global homogeneous, that is, $p=2$. (see Figure 3). The phase transition effect is shaper as large p. This case also indicates us the mechanism of de-noising because the noise diffuses quicker than the real signal and the edge-preserving is well for real signal. It seems that the p-Laplacian operator has been understood well. Now, we investigate the spike-Layers in diffusion systems to demonstrate the result is reverse in next section.

Section 4. Spike-Layers in Diffusion System

A spike-Layers in diffusion system has been introduced in [6]. Here, we generalized p-Laplacian operator from Laplacian operators and it is described as

$$U_t = d_1 \Delta_p U - U + U^a / V^b \ \ in \ \Omega \times (0, \infty)$$

$$\tau V_t = d_2 \Delta_p V - V + U^r / V^s \ \ in \ \Omega \times (0, \infty)$$

$$\frac{\partial U}{\partial n} = 0 = \frac{\partial V}{\partial n}, \ \ on \ \ \partial \Omega \times (0, \infty)$$
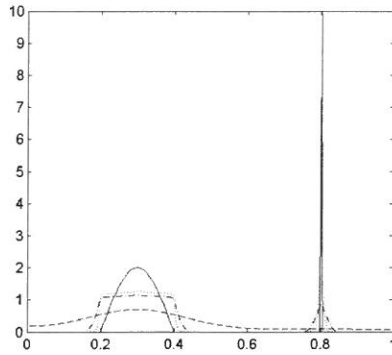

Figure 3. The initial data (solid line) consists of sine waves. The dashed line is for $p=2$ and it is the most diffusive. The dash-dot and dotted lines are for $p=3$ and $p=5$, respectively. The result demonstrates that the noise signal decays fast and real signals becomes sharp for large p.

where d_1, d_2, a, b, r, τ are all positive constants and s is a non-negative constant with

$$0 < \frac{a-1}{b} < \frac{r}{s+1}.$$

The spike-Layers in diffusion system is isolated due to the Nuemann boundary conditions. The solutions quickly become smooth and converges to a constant as time tends to infinity for the case $p=2$. We also believe the same results for general case $p>1$, but it is required the further investigation.

In order to develop the numerical simulation, we observe the stable kinetic system

$$U_t = -U + U^a / V^b \ in \ \Omega \times (0,\infty)$$
$$\tau V_t = -V + U^t / V^s \ in \ \Omega \times (0,\infty)$$

with the steady state $(U,V) = (1,1)$. See below Figure 4. The diffusion coefficients d_1 is small and d_2 is large. The steady state $(U,V)=(1,1)$ becomes unstable and bifurcation. Such phenomenon is called Turing's diffusion-driven instability. The large diffusion coefficient is difficult for numerical explicit method. We employ the implicit numerical scheme to solve the spike-Layers system in one dimension. The numerical method is introduced as the following
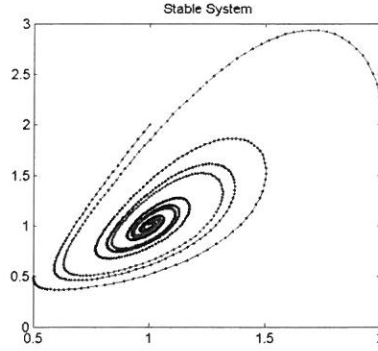

Figure 4. A stable kinetic system with steady state *(U, V)=(1,1)*. There are three initial data *(U, V)=(2,2)*, *(1,2)* and *(0.5,0.5)* corresponding to the red, blue and black line.

$$\frac{U_k^{n+1} - U_k^n}{\Delta t} = d_1 \frac{\left\| D^+ U_k^n \right\|^{p-2} D^+ U_k^{n+1} - \left\| D^+ U_{k-1}^n \right\|^{p-2} D^+ U_{k-1}^{n+1}}{(\Delta x)^2}$$
$$- U_k^{\ n} + (U_k^{\ n})^a / (V_k^{\ n})^b \ in \ [0,1] \times (0,\infty)$$

$$\tau \frac{V_k^{n+1} - V_k^n}{\Delta t} = d_2 \frac{\left\| D^+ V_k^n \right\|^{p-2} D^+ V_k^{n+1} - \left\| D^+ V_{k-1}^n \right\|^{p-2} D^+ V_{k-1}^{n+1}}{(\Delta x)^2}$$
$$- V_k^{\ n} + (U_k^{\ n})^t / (V_k^{\ n})^s \ in \ [0,1] \times (0,\infty)$$

The numerical solution is for the activator U with $d_1 = 0.0001$, $d_2 = 10$, $a = 2, b = 1$, $r = 2, s = 0, \tau = 0.7$. Then the initial data is given

$$U(x,0) = \begin{cases} 1.1 - x & 0 \le x \le 0.1, \\ 1, & 0.1 \le x \le 1, \end{cases} \quad and \quad V(x,0) = 1, 0 \le x \le 1.$$

The number of grid is 512. The numerical result $p=2$ is the same as the paper [6], but the location is different. These results show that the decay of the case $p=2$ is faster than $p=2.5$ (see Figure 5.) and the spike waves can go far away from the origin for $p=2.5$.

Section 5. Conclusion and Discussion

This paper has investigated diffusion effect of p-Laplacian operators in de-noising images, phase transition diffusion systems, and spike layers in diffusion systems. We conclude that the behavior of diffusion of the p-Laplacian operators is quite different for $p=2$ or $p>2$. The reason is that the case $p=2$ means that the global homogeneous diffusion and $p>2$ means that the local homogeneous diffusion coefficients. The global homogeneous diffusion will diffuse fast.
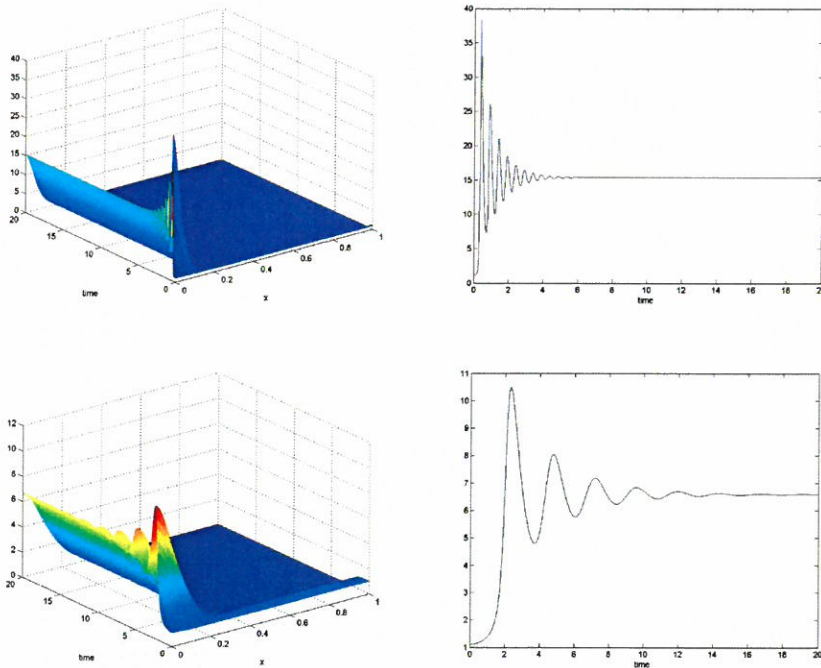

Figure 5. The top-left profile shows the solution on space and time and the top-right is the peak of the solution at $U(0,t)$, where $0<=t<=20$ for the case $p=2$. The corresponding results for $p=2.5$ are shown in the bottom. The result demonstrates that the spike wave can propagate farther away.

The phase transition diffusion system demonstrates the same behavior as the de-noising images. The noise signal diffuses faster than the real signals. It may be employed this observation to explain the mechanism of the de-noising images. For large p, it is more suitable for de-nosing.

Spike-Layers in diffusion system shows the spike waves with $p>2$ can propagate farther away from the origin than the one with $p=2$. In this case, the spike wave with $p=2$ can grow higher than the cases with $p>2$. It is not always consistent to the observation in de-noising images and phase transition diffusion systems. The reason could be the interaction of kinetic system and diffusion system. In this case, the results are more complicated than the previous one.

Numerical simulations are the explicit scheme for small diffusion and implicit scheme for large diffusion coefficients. The spike-Layers in diffusion system can provide an opportunity for us to study deeply. The difficulty for numerical simulations is the case p for being large enough. Therefore, the theoretical approaches are also used to probe the effect of p-Laplacian operators.

Finally, for the case $1 < p < 2$ not considered here, the reason is that the direction of diffusion process is from the condense region to other regions. On the other case of infinity, the p-Laplacian operators will become infinity Laplacian operator as the value p tends to infinity in the viscosity sense [1].

References

[1] M. G. Grandal, L.C. Evans, R. F. Gariepy, *Optimal Lipschitz extenstions and the infinity Laplacian*, Calc. Var. 13, 123-139 (2001).

[2] M. S. Chang, S. C. Lee, and C. C. Yen, Minimizer and Gamma Convergence of energy functionals derived from p-Laplacian equation, Taiwanese Journal of Mathematics (2008 accepted)

[3] Y. X. Huang, On eigenvalue problems of the p-Laplacian with Neumann boundary conditions, proceedings of the American Mathematical Socity, Vol. 109 (1990), No. 1, (May, 1990), 177-184.

[4] A. Kuijper, p-Lapalcian driven image processing, ICIP 2007, V. 257-260.

[5] L. Modica, The Gradient Theory of Phase Transitions and the Minimal Interface Criterion, Arch. Rational Mech. Anal. 98, (1987), 123-142.

[6] W. M. Ni, Diffusion, Cross-Diffusion, and Their Spike-Layer Steady States, Notices of the AMS, Vol 45, No. 1, (Jan, 1998), 9-18.

p-Laplacian 算子的擴散效果

張茂盛　李樹政　嚴健彰

輔仁大學數學系

摘　　要

我們利用數值方法且基於透過觀察影像去雜訊，相位轉換及棘波邊界層等擴散系統，研究 *p*-Laplacian 算子的擴散行為。對於 *p=2*，是原先的 Laplacian 算子，其擴散效應是全域均勻性的，其它 *p>2* 的例子，則是局部性的。

對影像去雜訊方面，隨著 *p* 值增加，*p*-Laplacian 算子的擴散效果呈現遞減。針對相位轉換擴散系統，其結果和影像去雜訊的結果是一致，進一步我們利用已得的結論，成功地解釋影像去雜訊的機制。事實上，對於 *p*-Laplacian 算子的擴散是相當複雜的，透過觀察棘波的傳遞，我們得到相反的結果，亦即，當 *p* 較大時，波的傳遞卻反而更遠離棘波發生的位置。

關鍵詞：*p*-Laplacian 算子，影像去雜訊，擴散系統，棘波邊界層

Computational Algorithms for Estimation of Fatigue Life under Random Loading

Horng-Yith Liou[1] and Lung Tsai

Dept. of Mechanical Engineering, Ching-Yun University, Zhong-Li, Taiwan

Abstract

This article is primarily centered on the derivation of mathematical formulas that can be used for the prediction of fatigue life under the fluctuating load of random nature. By the incorporation of random vibration theory as well as Morrow's nonlinear damage rule into the traditional *S-N* relationship, a key mathematical formula can thus be generated. Through the adequate handling of this formula, more compact computational algorithms can be induced subsequently. With a view to determining the maximum stress needed in applying the necessary formula, either Gumbel's asymptotic theory of statistical extremes or Lambert's empirical assumption is included. The accuracy of all computational algorithms for the prediction of fatigue life under random loading is surveyed by the experimental data of a batch of specimens made of 7075-T651 aluminum alloy. Aside from the above, the fatigue reliability assessment is made, where the parametric model is under study. Finally, some conclusions are drawn about the feasibility of derived formulas, the effects of parameters on the accuracy and the important role that the reliability assessment plays in life prediction.

Keywords : atigue life, Damage accumulation rule, Random vibration, Reliability.

[1] Corresponding author: Fax:+886-3-468-3301.
E-mail address: hyliou@cyu.edu.tw

1. Introduction

Research on fatigue under the fluctuating load of random nature has become an utmost important issue since this type of fracture mode frequently caused catastrophic damage in the real engineering applications. As is often the case with theoretical handling of the fatigue issue, the establishment of mathematical models has led to lots of ready-to-use formulas for the life assessments. Those often applied for the above purpose include random vibration theory, damage rules, and so forth. Random vibration theory (Crandall, 1963; Lin, 1973; Newland, 1993) has been introduced for the past several decades to tackle all kinds of vibration behavior when random nature is taken into account, the application of which on fatigue has made life prediction to be of the important concern in almost any random vibration book. Among the fatigue damage rules, two most frequently used are the linear rule (Miner, 1945) and nonlinear plastic work interaction rule (Morrow, 1986). The distinction between them is that Morrow's rule modifies Miner's rule by multiplying a given stress level's cycle ratio damage term by a nonlinear factor to accommodate the sequence or memory effect originating in overloads or overstrains during a variable-amplitude loading history. Furthermore, Lambert (Lambert, 1988) has extended Morrow's plastic work interaction damage rule to the case of a continuously distributed random stress history as usually considered in many random vibration books. Suppose the necessary statistical/probabilistic properties of different types of random load are known beforehand, the expected fatigue life can be estimated based on formulas derived by the combination of theories/rules stated above.

The present paper focuses on the derivation of a "key formula", from which formulas of fatigue life prediction under the random loading are generated. Gumbel's asymptotic theory of statistical extremes and Lambert's empirical assumption are herein proposed to determine the maximum stress during the loading history. A batch of test specimens made of 7075-T761 aluminum alloy has been used for the fatigue experiment to verify the applicability of the derived algorithms. Besides, in order to make the full use of the experimental life data, the reliability assessment that involves parametric investigation is to aid in obtaining further information.

2. Model Establishment

2.1 Prediction of Fatigue Life

In the present study, the main framework is constructed on the basis of S-N relationship (Bannantine et al., 1990), which is expressed in the following form

$$N_f \sigma^p = C,$$ (1)

where σ is constant-amplitude stress, N_f represents the fatigue life at the stress level σ, and p and C are fitting constants.

In a variable-amplitude stress condition, according to Morrow's plastic work interaction rule, the fatigue damage done by the stress of amplitude σ_i can be written as

$$D_i = \frac{n_i}{N_{fi}}(\frac{\sigma_i}{\sigma_m})^d,$$ (2)

in which σ_m is the maximum stress amplitude in the stress history considered, n_i is the number of stress peak at level σ_i, N_{fi} is the number of stress peak to cause failure if constant amplitude σ_i is considered, and d is Morrow's plastic work interaction exponent. The exponent can be elucidated as the material's sensitivity to the variable-amplitude stress history. From eq. (2), if all different cyclic stresses are taken into account, the cumulative fatigue damage becomes

$$D = \sum_i D_i = \sum_i \frac{n_i}{N_{fi}}(\frac{\sigma_i}{\sigma_m})^d,$$ (3)

where the fatigue failure occurs when the damage index D reaches unity. If the exponent d is chosen to be zero, the above nonlinear damage rule can be reduced to the famous Miner's rule, i.e.

$$D = \sum_{i=1}^{n} \frac{n_i}{N_{fi}}.$$ (4)

In accordance with random vibration theory, under a narrow-band process, the expected total fatigue damage of a component in time T can be estimated by the following integral

$$E[D(T)] = v_0^+ T \int_0^\infty \frac{p(\sigma)}{N_f(\sigma)} (\frac{\sigma}{\sigma_m})^d d\sigma , \tag{5}$$

in which $E[\bullet]$ is the expected value of the bracketed quantity, v_0^+ is the expected number of the zero up-crossing rate which can be considered as the expected number of stress cycle per unit time for a narrow-band random process, $p(\sigma)$ is the probability density function of stress amplitudes, and $N_f(\sigma)$ is now distributed as a function of stress amplitude.

According to random vibration theory, if the stress history is a zero-mean, narrow-band Gaussian random process, then the probability density function of the stress amplitudes is distributed in Rayleigh form

$$p(\sigma) = \frac{\sigma}{\sigma_{rms}^2} \exp(-\frac{\sigma^2}{2\sigma_{rms}^2}), \sigma > 0 \tag{6}$$

in which σ_{rms} is the standard deviation of the random stress process (but not stress amplitudes). Substitution of eqs. (1) and (6) into eq. (5) yields the following equation

$$E[D(T)] = \frac{v_0^+ T}{C\sigma_{rms}^2} \int_0^\infty \frac{\sigma^{p+d+1}}{\sigma_m^d} \exp(-\frac{\sigma^2}{2\sigma_{rms}^2}) d\sigma . \tag{7}$$

The integration in eq. (7) is performed from zero to infinity, which includes all possible values of the stress amplitude. However, it is by no means the real case.

When experimental fatigue tests are performed in the laboratory, a clipping stress is usually assigned for the generated random loading history so as to protect the test machine. Under this circumstance, the clipping stress becomes the maximum stress amplitude in eq. (7) and, when the numerical integration is carried out, all stress amplitudes exceeding the maximum stress should be treated as the maximum stress. Therefore, eq. (7) should be modified as

$$E[D(T)] = \frac{v_0^+ T}{C\sigma_m^d} (\sqrt{2}\sigma_{rms})^{p+d} \gamma(\frac{p+d}{2}+1, \rho) + \frac{v_0^+ T}{C} (\sigma_m)^{p-d} (\sqrt{2}\sigma_{rms})^d [\Gamma(\frac{d}{2}+1) - \gamma(\frac{d}{2}+1, \rho)], \tag{8}$$

in which $\rho = \sigma_m^2 / 2\sigma_{rms}^2$, and the special functions Γ and γ represent Gamma and incomplete Gamma functions, respectively.

The above eq. (8) is named "key formula" in the present study, which not only can encompass a number of analogous formulas derived by past researchers but also can, to a certain extent, improve the accuracy of prediction.

When Morrow's plastic interaction exponent is selected to be zero, the expression of eq. (8) becomes

$$E[D(T)] = \frac{v_0^+ T}{C}(\sqrt{2}\sigma_{rms})^p \gamma(\frac{p}{2}+1, \rho) + \frac{v_0^+ T}{C}\sigma_m^p \exp(-\rho).$$ (9)

Eq. (9) is a special case in which Miner's rule is considered.

The term $v_0^+ T$ in eqs. (8) and (9) is hereafter replaced by N, which indicates the number of stress cycles. While the expected total damage at the left-hand side of these two equations reaches unity, the unknown N can be thus solved for the prediction of fatigue life.

So far, a significant problem has arisen from how to determine the clipping stress. One way is based on Gumbel's asymptotic theory of statistical extremes. According to Gumbel, the probability distribution of the largest value among a sequence of N identically distributed random values can be determined by the theory of standard order statistics. In the problem under current consideration, let σ_1, σ_2, ... and σ_N be the stress amplitudes which are identically distributed such as the one shown in eq. (6), if N is sufficiently large, then the cumulative distribution of the maximum amplitude approaches to the following Type I asymptotic distribution of the largest value

$$F_{\Sigma_m}(\sigma_m) = \exp\{-\exp[-\alpha_N(\sigma_m - \mu_N)]\},$$ (10)

in which F indicates the cumulative distribution function, μ_N is the characteristic parameter, and α_N is an inverse measure of dispersion. The expected value of the maximum amplitude can therefore be derived based on eq. (10) as well as the cumulative distribution function $F(\sigma)$. In particular, if eq. (6) is considered, the expected maximum amplitude is shown as

$$E[\Sigma_m] = \sigma_{rms}(\sqrt{2\ln N} + \frac{0.577}{\sqrt{2\ln N}}) = \sigma_m,$$ (11)

where 0.577 is a truncated Euler's constant. Eq. (11) is interpreted as the theoretically derived "expected" maximum stress amplitude.

In the case of high stress level, i.e., large σ_m or ρ, eq. (8) can be approximated as

$$E[D(T)] = \frac{v_0^+ T}{C \sigma_m^d} (\sqrt{2}\sigma_{rms})^{p+d} \, \Gamma(\frac{p+d}{2} + 1) \tag{12}$$

and with the term $\dfrac{0.577}{\sqrt{2\ln N}}$ dropped, the expression of eq. (11) becomes

$$E[\Sigma_m] = \sigma_{rms}(\sqrt{2\ln N}) = \sigma_m . \tag{13}$$

Combination of both eqs. (12) and (13) yields

$$\frac{(\sqrt{\ln N})^d}{N} = \Gamma(\frac{p+d}{2} + 1) \cdot \frac{1}{C} \cdot (\sqrt{2}\sigma_{rms})^p , \tag{14}$$

where $E[D(T)]=1$ and $v_0^+ T = N$ are set in eq. (12). When d is selected to be zero, the expression of eq. (14) becomes

$$\frac{1}{N} = \Gamma(\frac{p}{2} + 1) \cdot \frac{1}{C} \cdot (\sqrt{2}\sigma_{rms})^p , \tag{15}$$

as is the case with Miner's rule taken into account again. Such formulas as analogous to eq. (15) can be found in the relevant books, while the expression of eq. (14) is presented by the authors of this article for the first time.

The second way of dealing with the clipping stress is based on Lambert's empirical assumption. Lambert suggested that σ_m be 4~7 times the value of σ_{rms}. If the clipping ratio is defined as

$$r = \frac{\sigma_m}{\sigma_{rms}} , \tag{16}$$

then eq. (11) can be rewritten as

$$r = (\sqrt{2\ln N} + \frac{\gamma}{\sqrt{2\ln N}}) , \tag{17}$$

where γ (=0.577) is a truncated Euler's constant. The fatigue life N in terms of r can be induced from eq. (17)

$$N = \exp[0.25 \cdot (r^2 - 1.154 + r\sqrt{r^2 - 2.308})]. \tag{18}$$

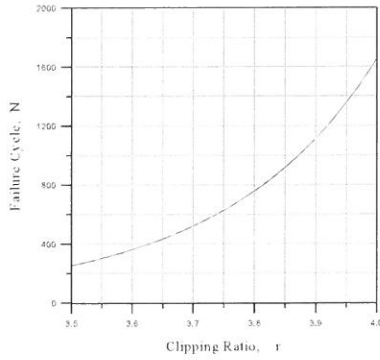Fig. 1(a)~ 1(d) show N-r plots with r ranging from 3.5 to 7.
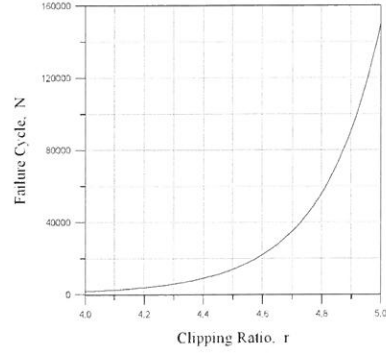

Fig. 1   (a) N-r plot ($r = 3.5\text{~}4.0$)

Fig. 1(b) N-r plot ($r = 4.0\text{~}5.0$)
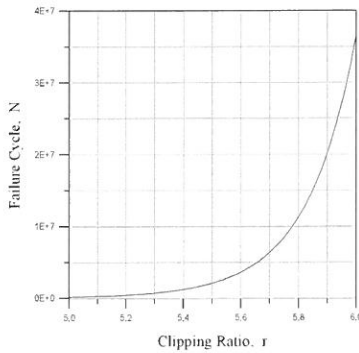
Fig. 1(c) N-r plot ($r = 5.0\text{~}6.0$)
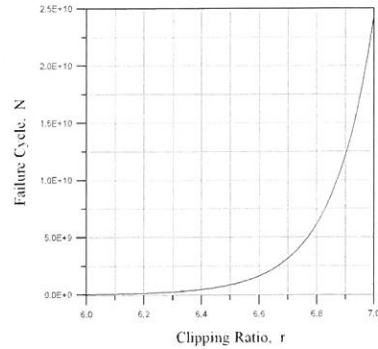
Fig. 1(d) N-r plot ($r = 6.0\text{~}7.0$)

Additionally, from an engineering point of view, a more straightforward solution to the clipping stress is based on the maximum tensile strength of a tested material. As can be seen in the later section, it indeed yields a good effect in the numerical calculation according to this argument.

2.2 Fatigue Reliability Assessment (Kapur et al., 1977; Leemis, 1995)

At present, in order to get further information on the fatigue life data available, reliability

assessment is made. Hence, our current concern lies in the parametric analysis of a complete data set, in that the fatigue test under the present study is carried out until all the specimens fracture. A brief introduction to the model is made as follows.

The life data are fitted by specified probability distributions, and chi-square tests are then employed to examine the goodness-of-fits for all plots. The detailed procedure for the foregoing analysis has been standardized and documented in many related books. However, special emphasis is herein stressed on the Weibull probability function since it has been proved to be the best among these competitive models in the present study.

The four lifetime distribution representations for the Weibull distribution are

$$f(t) = \kappa \lambda^{\kappa} t^{\kappa-1} e^{-(\lambda t)^{\kappa}}, \quad R(t) = e^{-(\lambda t)^{\kappa}}, \quad h(t) = \kappa \lambda^{\kappa} t^{\kappa-1} \quad \text{and} \quad H(t) = (\lambda t)^{\kappa}, \tag{19}$$

where $f(t)$ is the probability density function, $R(t)$ is the survivor function, $h(t)$ is the hazard function and $H(t)$ is the cumulative hazard function, and $\lambda > 0$, $\kappa > 0$ represent the scale and shape parameters, respectively. When there are n observed lifetimes for a complete data set, say t_i ($i = 1 \sim n$), the natural logarithm likelihood function is expressed as

$$\ln L(\lambda, \kappa) = n \ln \kappa + \kappa n \ln \lambda + (\kappa - 1) \sum_{i=1}^{n} \ln t_i - \lambda^{\kappa} \sum_{i=1}^{n} t_i^{\kappa}. \tag{20}$$

Partial differentiations of $\ln L(\lambda, \kappa)$ with respect to λ and κ yield

$$\frac{\partial \ln L(\lambda, \kappa)}{\partial \lambda} = \frac{\kappa n}{\lambda} - \kappa \lambda^{\kappa-1} \sum_{i=1}^{n} t_i^{\kappa} \tag{21}$$

and

$$\frac{\partial \ln L(\lambda, \kappa)}{\partial \kappa} = \frac{n}{\kappa} + n \ln \lambda + \sum_{i=1}^{n} \ln t_i - \sum_{i=1}^{n} (\lambda t_i)^{\kappa} \ln(\lambda t_i). \tag{22}$$

When the above eqs. (21) and (22) are set equal to zero, the simultaneous equations have no closed-form solution

$$\lambda = \left[\frac{n}{\sum_{i=1}^{n} t_i^{\kappa}} \right]^{1/\kappa} \tag{23}$$

and

$$\frac{n}{\kappa} + \sum_{i=1}^{n} \ln t_i - \frac{n \sum_{i=1}^{n} t_i^{\kappa} \ln t_i}{\sum_{i=1}^{n} t_i^{\kappa}} = 0 . \tag{24}$$

Here let $\hat{\lambda}$ and $\hat{\kappa}$ be the numerical solutions of λ and κ, respectively. Once $\hat{\kappa}$ is attained from eq. (24) by the numerical scheme, substitution of $\hat{\kappa}$ back into eq. (23) will yield $\hat{\lambda}$. Based on the known $\hat{\kappa}$ and $\hat{\lambda}$, the empirical lifetime functions associated with the Weibull fit can be determined according to eq. (19).

With the object of getting a further comprehension of the confidence intervals about λ and κ, the procedure is undergone in such a way as stated below. The second-order partial derivatives of $\ln L(\lambda, \kappa)$ are

$$\frac{-\partial^2 \ln L(\lambda, \kappa)}{\partial \lambda^2} = \frac{\kappa \cdot n}{\lambda^2} + \kappa(\kappa-1)\lambda^{\kappa-2} \sum_{i=1}^{n} t_i^{\kappa} ,$$

$$\frac{-\partial^2 \ln L(\lambda, \kappa)}{\partial \lambda \partial \kappa} = -\frac{n}{\lambda} + \lambda^{\kappa-1} \left[\kappa \sum_{i=1}^{n} t_i^{\kappa} \ln t_i + (1 + \kappa \ln \lambda) \sum_{i=1}^{n} t_i^{\kappa} \right] ,$$

$$\frac{-\partial^2 \ln L(\lambda, \kappa)}{\partial \kappa^2} = \frac{n}{\kappa^2} + \sum_{i=1}^{n} (\lambda t_i)^{\kappa} (\ln \lambda t_i)^2 . \tag{25}$$

The observed information matrix in accordance with eq. (25) is established as

$$O(\hat{\lambda}, \hat{\kappa}) = \left[\begin{array}{cc} \dfrac{-\partial^2 \ln L(\lambda, \kappa)}{\partial \lambda^2} & \dfrac{-\partial^2 \ln L(\lambda, \kappa)}{\partial \lambda \partial \kappa} \\ \dfrac{-\partial^2 \ln L(\lambda, \kappa)}{\partial \lambda \partial \kappa} & \dfrac{-\partial^2 \ln L(\lambda, \kappa)}{\partial^2 \kappa} \end{array} \right]_{\lambda = \hat{\lambda},\ \kappa = \hat{\kappa}} . \tag{26}$$

The variances (or standard deviations) of both the parameter estimators, i.e. $\hat{\kappa}$ and $\hat{\lambda}$,

can be computed using the inverse of the observed information matrix $O^{-1}(\hat{\lambda}, \hat{\kappa})$. The confidence intervals with respect to λ and κ can be obtained accordingly.

3. Experimental Work

In order to check the feasibility of the formulas derived in the preceding section, fatigue experiment has been performed in the present study. Only a brief description is presented here and readers are suggested to consult the relevant reference (Xie, 1995) for detailed depictions. The test specimens were made of 7075-T761 aluminum alloys and prepared in conformity with ASTM E606 standard. The shape and dimensions of the specimen are indicated in Fig. 2. The material has a yield stress of 512 MPa, ultimate strength of 627 MPa, and Young's modulus of 73.5 GPa, which are all revealed in a mean sense. An MTS axial-torsional servo-hydraulic test machine was used to execute the experiment. During the first phase of the experiment, fully reversed, constant-amplitude, strain-controlled, low-cycle fatigue tests were performed. The strain-life curves (Bannantine et al., 1990) were plotted and the result was used to obtain the material constants needed for the subsequent computations. The total strain range (ε) was composed of an elastic part (ε_e) and a plastic part (ε_p). And for all test specimens, the empirical strain-life relationship is

$$\varepsilon = \varepsilon_e + \varepsilon_p = \frac{\sigma_f}{E}(2N_f)^b + \varepsilon_f(2N_f)^c , \tag{27}$$

where σ_f is the fatigue strength coefficient, ε_f is the fatigue ductility coefficient, b is the fatigue strength exponent and c is the fatigue ductility exponent. If the elastic strain dominates for a greater portion of life range, the relationship in eq. (27) can be revised as

$$\varepsilon_e = \frac{\sigma}{E} = \frac{\sigma_f}{E}(2N_f)^b \tag{28}$$

which, in fact, exhibits a Basquin's equation of

$$\sigma = \sigma_f(2N_f)^b . \tag{29}$$

Comparing eq. (29) with eq. (1), it can be shown that $C = 1/2\sigma_f^{1/b}$ and $p = -1/b$.
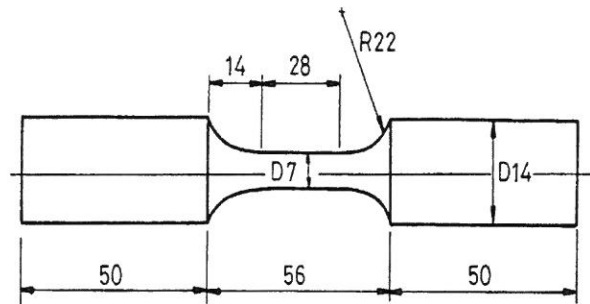
Fig. 2 The test specimen (in mm)

After fundamental fatigue data were obtained from the test result, stress-controlled random fatigue tests were performed in the second phase of the experiment. During the test processes, stress histories and fatigue lives were recorded for the future analysis. Fifteen stress histories such as the one shown in Fig. 3 were generated, and each applied to a specimen until the specimen fractured. The fatigue lives of specimens under random loading are tabulated in Table 1, where the specimens are numbered in the first column and the corresponding fracture cycles are indicated in the second column.
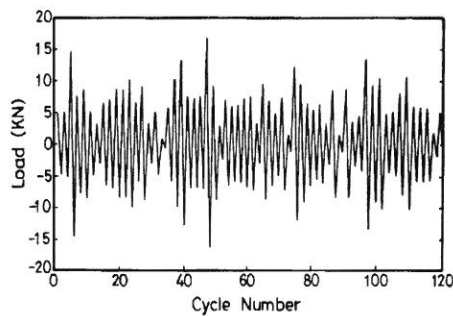

Fig. 3 A segment of random loading history

Table 1   Fatigue lives of test specimens

Specimen No.	No. of Cycles to Failure
ART- 1	10803
ART- 2	9783
ART- 3	10419
ART- 4	10441
ART- 5	10102
ART- 6	9921
ART- 7	10381
ART- 8	9732
ART- 9	10146
ART- 10	9978
ART- 11	9836
ART- 12	10237
ART- 13	10292
ART- 14	9344
ART- 15	10533
Mean	10131
Std.	324.51

4. Results and Discussion

In the present study, the strain-life curve is constructed as shown in Fig. 4, from which it is found that $\sigma_f = 1286.7601\,\text{MPa}$, $b = -0.1486$, $\varepsilon_f = 0.116$ and $c = -0.776$. The empirical constants needed in applying eq.(1) are found to be $p = 6.7290$ and $C = 4.2097 \times 10^{20}$ accordingly.
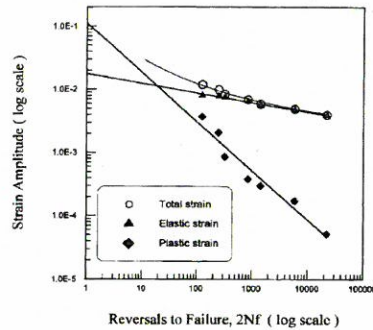
Fig. 4 Strain-life curve

The computational results associated with experimental set when subjected to the constant clipping ratio r are tabulated in Table 2 and all predicted results should be viewed in an average sense. As exhibited in Table 2, the plastic work interaction rule (for $d=-0.25$, -0.35 and -0.45) indeed improves the prediction over the widely used Miner's rule (for $d=0$). The degree of improvement is contingent upon the selection of exponent d that can only be determined on a trial basis so far, and the adoption of the minimum d yields the best result. Furthermore, the increase in the value of r will render a trend of more conservative life prediction. Both the mean and standard deviation for the experimental data are also listed in the same table.

Table 2   Computational results under constant σ_m / σ_{rms}

Applied Equation	Eq.(8)			
Fatigue Life Const σ_m / σ_{rms}	$d = 0$	$d = -0.25$	$d = -0.35$	$d = -0.45$
$\sigma_m = 630\, MPa$ $\sigma_{rms} = 142.53\, MPa$	13624	12104	11531	10978
$\sigma_m / \sigma_{rms} = 4$	13846	12589	12106	11633
$\sigma_m / \sigma_{rms} = 5$	13557	11686	10999	10346
$\sigma_m / \sigma_{rms} = 6$	13548	11591	10314	9526
$\sigma_m / \sigma_{rms} = 7$	13548	10737	9772	8888
Remark: The mean is 10131 and the standard deviation 324.51 for the experimental data.				

If the maximum clipping stress is not known beforehand, an accurate result can be attained through the use of Gumbel's asymptotic theory of statistical extremes. The results under Gumbel's theory are shown in Table 3. Again, all predicted results should be interpreted in averages. Observed from Table 3, all predictions based on Morrow's nonlinear damage rule are better than those on Miner's linear rule in accuracy. The incorporation of statistics of extremes, i.e. eq. (11), into "key formula", i.e. eq. (8), yields an improving effect. In the same table, a good prediction effect is achieved as well in accordance with eq. (14).

Table 3   Computational results under Gumbel's asymptotic theory

Applied Equation (Based on $\sigma_{rms} = 142.53\,MPa$)	Eq.(8)+Eq.(11)	Eq.(14)
$d = 0$	13606	13548
$d = -0.25$	12061	12103
$d = -0.35$	11490	11565
$d = -0.45$	10944	11050
Remark: The mean is 10131 and the standard deviation 324.51 for the experimental data.		

Another approach is proceeded such that the clipping stress, σ_m, is taken as the maximum tensile stress of the material under experiment, say 630 MPa. By eq.(16), r can be calculated as 4.4201. Substituting this value into eq.(18), we can obtain N, which approximates 9727. An alternative estimation is referred to Fig.1(b), from which the same result can also be yielded. The prediction of fatigue life in this way seems slightly conservative compared with the experimental life average, 10131. Nevertheless, it indeed yields a good prediction effect.

Presented below are the results of reliability analysis. In order to carry out the parametric analysis for the present study, the life data are fitted by the normal, log-normal and Weibull probability distributions at first and then chi-square tests are used to check the goodness-of-fits. It is found that the Weibull fit is superior to the other two fits. Following the procedure described in the section 2.2, let eqs. (21) and (22) be set equal to zero simultaneously and the fitted Weibull distribution has maximum likelihood estimators $\hat{\lambda} = 9.7086 \times 10^{-5}$, $\hat{k} = 31.3013$.

These maximum likelihood estimators were determined using a computer program.

Substitution of $\hat{\lambda}$ and $\hat{\kappa}$ into eqs. (25) and (26) yields the observed information matrix as

$$O(\hat{\lambda}, \hat{k}) = \begin{bmatrix} 1.5592 \times 10^{12} & 70809.2 \\ 70809.2 & 0.0302 \end{bmatrix}.$$

The inverse of the observed information matrix $O^{-1}(\hat{\lambda}, \hat{\kappa})$ can be obtained as

$$O^{-1}(\hat{\lambda}, \hat{k}) = \begin{bmatrix} 7.1785 \times 10^{-13} & -1.6841 \times 10^{-6} \\ -1.6841 \times 10^{-6} & 37.0833 \end{bmatrix}.$$

The standard deviations of both the parameter estimators, i.e. $\hat{\kappa}$ and $\hat{\lambda}$, in terms of the inverse of the observed information matrix $O^{-1}(\hat{\lambda}, \hat{\kappa})$ are computed to be $\hat{\sigma}_{\lambda} = 8.4726 \times 10^{-7}$ and $\hat{\sigma}_{k} = 6.0896$, respectively. A 95% confidence region for the parameters is satisfied by

$$9.52691 \times 10^{-5} < \lambda < 9.89035 \times 10^{-5}$$

and $18.2404 < k < 44.3622.$
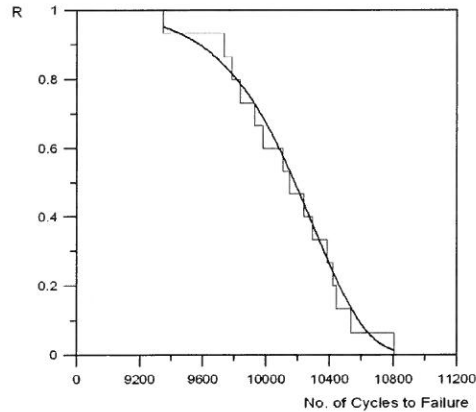
The Weibull fit for the present case is shown in Fig. 5.

Fig. 5 The Weibull fit for parametric analysis

5. Conclusions

In accordance with the present study, some conclusions can be drawn with regard to the

fatigue life of a component when random loading is taken into account.

1. An approach to fatigue life based on the establishment of mathematical models is comparatively feasible for quick prediction, despite the fact that the computational process may be somewhat tedious occasionally. In the present paper, emphasis is stressed on the key formula, through which lots of formulas derived past in this field can be stemmed systematically. Furthermore, the key formula not only can, to a certain extent, improve the accuracy but also can extend the life prediction downward to an order of 10^3 in cycle with still remaining an acceptable accuracy. Alternatively, all formulas in this paper can be used for the calculation of fatigue damage, the discussion of which is beyond our concern and spared in the present paper.

2. The plastic work interaction exponent, d, evidently dominates the accuracy of the life estimation. For most cases in which longer fatigue lives are considered, the results computed based on Miner's rule ($d=0$) show the severe deviation from the real data and the selection of the lowest value of d gives rise to the most conservative outcomes. For the special case which allows for very short lives, the selection of d scarcely has any influence on life prediction. The increase in the value of the clipping ratio r elucidates a trend of more conservative life prediction. The decrease in the value of d leads to a more perceptible variation in the life estimation when the different clipping ratios r is considered. In the case of longer fatigue life prediction, regardless of whether Lambert's empirical assumption or Gumbel's statistical extreme is applied, all formulas on the whole yield satisfactory prediction results. However, the use of Gumbel's statistical extreme in the case of shorter lives will overly induce conservative estimations. A criterion proposed for surveying the applicability of computational algorithms under Gumbel's theory is up to the clipping ratio r, which can be yielded by eq. (17). It is found that the predicted life will get less accurate when the corresponding value of r is smaller than 4, and that the degree of inaccuracy increases with the distance of r-value from 4.

3. Reliability assessment can serve as an alternative approach to fatigue issue by measuring the probability of a component's life that can survive over a specified time. It assists researchers in obtaining more information according to the life data available, allowing a further penetration of the fatigue scatter feature. Under the current learning, the reliability analysis is made in such a way that adequate lifetime distribution functions are established

through a set of known experimental data. Conversely, the experimental data is simply used to justify the applicability of mathematical formulas formerly derived such as eq. (8), eq. (14), and so forth.

References

[1] Bannantine, J. A., Comer, J. J. and Handrock, J. L., Fundamentals of Metal Fatigue Analysis, Prentice-Hall, New Jersey (1990).

[2] Crandall, S. H., and Mark, W. D., Random Vibration in Mechanical Systems, Academic Press, New York (1963).

[3] Kapur, K. C. and Lamberson, L. R., Reliability in Engineering Design, John Wiley & Sons, Inc., New York (1977).

[4] Lambert, R. G., "Plastic Work Interaction Damage Rule Applied to Narrow-Band Gaussian Random Stress Situations," J. Pressure Vessel Technology, Trans. of ASME, Vol. 110, pp. 88-90 (1988).

[5] Leemis, L. M., Reliability, Prentice-Hall, New Jersey (1995).

[6] Lin, Y. K., Probabilistic Theory of Structural Dynamics, McGraw-Hill, New York (1973).

[7] Miner, M. A., "Cumulative Damage in Fatigue", J. Appl. Mechanics, Trans. of ASME, Vol.12, pp. 159-164 (1945).

[8] Morrow, J. D., "The Effect of Selected Subcycle Sequences in Fatigue Loading Histories", Random Fatigue Life Predictions, ASME, PVP Vol. 72, pp. 43-60 (1986).

[9] Newland, D. E., An Introduction to Random Vibration, Spectral & Wavelet Analysis, Longman Scientific & Technical, John Wiley & Sons, Inc., New York (1993).

[10] Wu, W. F. and Huang, T. H., "A Statistical Nonlinear Cumulative Damage Rule and Fatigue Life Prediction Under Random Loading", J. Pressure Vessels & Piping, Vol. 47, pp. 1-16 (1991).

[11] Xie, H. C., "Research of Low-Cycle Fatigue of 7075-T651 Aluminum Under Random Loading", Master Thesis, Department of Mechanical Engineering, National Taiwan University, Taipei, Taiwan (1995).

隨機負載下疲勞壽命估測之數學導式

劉宏毅　　蔡龍

私立清雲科技大學

機械工程學系

桃園縣中壢市健行路 229 號

摘　　要

　　本篇文章乃著眼於在隨機負載下疲勞壽命估測之數學公式推導及其應用。經由一藉隨機振動理論及 Morrow 非線性損傷法則帶入 *S-N* 疲勞關係式所發展得到之核心公式，可衍生一連串之估測數學式。為了決定核心公式中所需之最大應力值，吾人應用 Gumbel 之漸近極值理論或 Lambert 之經驗公式。所推導而得之數學公式的準確性則由一批 7075-T651 鋁合金加以驗證，而藉不同之數學公式計算所得到結果亦在本文章中加以比較。此外，應用參數化模式之可靠度估測亦被提出。最後，對於導出之數學公式的可行性、參數對於準確性之影響及可靠度對於疲勞壽命評估所扮演之重要角色作出簡要之結論。

關鍵詞：疲勞壽命；疲勞損傷法則；隨機振動；可靠度。

廣義貝它分佈參數之模擬研究

陳威弟　　陳思勉[1]

輔仁大學數學研究所及數學系

smchen@math.fju.edu.tw

摘　　要

理論上，貝氏估計式為貝氏風險下的最佳解，然本研究討論若以平方誤損失函數下之風險函數為比較準則時，廣義貝它分佈參數之數種估計式的表現。

關鍵字：*G3B*；*Lindley approximation*；*importance sampling.*

1. 簡介

　　M. Sahinoglu 及 D. L. Libby 於 1981 年同時提出三參數廣義貝它分佈 $G3B(\alpha,\beta,\gamma)$。1982 年，Libby 與 Novick 導出 G3B 的各階動差與邊際分佈，條件分佈。1984 年，Chen 與 Novick 應用 G3B 在 Binomial 模型上，而且當兩個形狀參數皆大於 1 時，導出眾數之具體解。在應用上，Bonnie Kegan 與 Webster West (2005) 應用此分佈於傳染病研究上。M. Sahinoglu，D. L. Libby 與 S. R. Das (2005) 則將這個機率模型應用在研究網路可靠度的問題。

　　假設隨機變數 X 的機率密度函數（pdf）為 $f_X(x) = \dfrac{\gamma^\alpha x^{\alpha-1}(1-x)^{\beta-1}}{B(\alpha,\beta)\{1-(1-\gamma)x\}^{\alpha+\beta}}$，當 $0 < x < 1$ 時，其中 $\alpha,\beta,\gamma > 0$，$B(\alpha,\beta) = \int_0^1 t^{\alpha-1}(1-t)^{\beta-1}dt$，則稱 X 為服從三參數廣義貝它

分佈 $G3B(\alpha,\beta,\gamma)$。當 $\gamma=1$ 時，$G3B(\alpha,\beta,\gamma)$ 分佈即爲標準貝它分佈。本文第二節將介紹 $G3B(\alpha,\beta,\gamma)$ 分佈參數之貝氏估計式；第三節爲模擬研究，第四節爲結論。

2. 貝氏估計式

根據貝氏統計，如果損失函數爲對稱型的平方誤損失函數(squared error loss function)，則參數 θ 的貝氏估計式爲事後期望值，即 $\hat{\theta}_{bs}=E(\theta\,|\,\underline{X})$；然而平方誤損失函數在許多情況下並不適用，舉例來說，對於農作物的農藥殘留檢測上，低估殘留劑量對人體所導致的危險性比高估殘留劑量對人體所導致的危險性來得嚴重；相同的對於氣象預報，尤其在雨季，低估降雨量所導致的財務損失是比高估降雨量所導致的財務損失來得嚴重。此時非對稱型的損失函數較爲恰當。針對此類現象 Zellner(1986) 提出一個非對稱型損失函數 $L(\Delta)=b[e^{a\Delta}-a\Delta-1]$，$a\neq0$，$b>0$，其中 $\Delta=\hat{\theta}-\theta$（俗稱 LINEX 損失函數）。當損失函數爲 LINEX 損失函數時，其貝氏估計式可表示爲 $\hat{\theta}_{bl}=-\dfrac{1}{a}\ln\{E(e^{-a\theta}\,|\,\underline{X})$。理論上貝氏估計式是在貝氏風險下的最佳解，因此本文不就此論點做驗證。反之我們想研究若以在均方誤風險函數爲比較準則，幾種參數估計式的表現。換言之，我們想要了解貝氏估計式是否穩健(Robust)。

在貝氏統計研究中，有許多選擇事前分佈的方法。本文中我們僅就未知參數具有 improper-informative 的事前分佈 $\Pi(\theta)=\dfrac{1}{\theta},\theta>0$ 來討論。此外，我們假設參數 α,β,γ 相互獨立。

2.1 當一個參數未知時

當參數 θ 是未知且假設其事前分佈爲 $\pi(\theta)=1/\theta$，$\theta>0$，則在平方誤損失函數下，當 $\displaystyle\int_0^\infty\dfrac{p(\theta\,|\,x)}{\theta}d\theta=c$ 收斂時，貝氏估計式 $\hat{\theta}_{bs}=\dfrac{\displaystyle\int_0^\infty p(\theta|x)d\theta}{c}$，而在 LINEX 損失函數下貝氏估計式爲 $\hat{\theta}_{bl}=-\dfrac{1}{a}\ln\{\dfrac{1}{c}\displaystyle\int_0^\infty\dfrac{p(\theta\,|\,x)}{\theta}e^{-a\theta}d\theta\}$，其中 $p(\theta\,|\,\underline{x})=p(\alpha,\beta,\gamma\,|\,\underline{x})=\displaystyle\prod_{i=1}^n\dfrac{\gamma^\alpha x_i^{\alpha-1}(1-x_i)^{\beta-1}}{B(\alpha,\beta)[1-(1-\gamma)x_i]^{\alpha+\beta}}$，$\theta$ 爲三個參數 α,β,γ 中未知的參數。

2.2 當兩個參數未知時

當其中兩個參數未知且相互獨立並具有前所設的事前分佈時，貝氏估計式爲兩個複雜的雙重積分相除，爲了處理這個問題，我們引用 Lindley 於 1980 年所提出的方法求貝氏估計式之近似解。

(一)當 α, β 未知時，兩者之貝氏估計式 $\hat{\alpha}_{bs}$, $\hat{\beta}_{bs}$ 及 $\hat{\alpha}_{bl}$, $\hat{\beta}_{bl}$ 的近似解分別爲

$$\hat{\alpha}_{bs} \approx \alpha - \frac{\tau_{11}}{\alpha} - \frac{\tau_{12}}{\beta} + \frac{1}{2}\Phi_1 \; ; \qquad\qquad \hat{\beta}_{bs} \approx \beta - \frac{\tau_{21}}{\alpha} - \frac{\tau_{22}}{\beta} + \frac{1}{2}\Phi_2 \; ;$$

$$\hat{\alpha}_{bl} \approx \alpha - \frac{1}{a}\ln(1 + \frac{a\tau_{11}}{\alpha} + \frac{a\tau_{12}}{\beta} + \frac{1}{2}\Phi_3) \; ; \qquad \hat{\beta}_{bl} \approx \beta - \frac{1}{a}\ln(1 + \frac{a\tau_{21}}{\alpha} + \frac{a\tau_{22}}{\beta} + \frac{1}{2}\Phi_4)$$

其中

$$\Phi_1 = I_{30}\tau_{11}^2 + I_{03}\tau_{21}\tau_{22} + I_{21}(3\tau_{11}\tau_{12} + \tau_{11}\tau_{22} + 2\tau_{21}) \; ;$$

$$\Phi_2 = I_{03}\tau_{22}^2 + I_{30}\tau_{12}\tau_{11} + I_{21}(3\tau_{22}\tau_{21} + \tau_{11}\tau_{22} + 2\tau_{12}^2) \; ;$$

$$\Phi_3 = -a[-a\tau_{11} + I_{30}\tau_{11}^2 + I_{03}\tau_{21}\tau_{22} + I_{12}(3\tau_{11}\tau_{12} + \tau_{11}\tau_{22} + 2\tau_{21}^2)] \; ;$$

$$\Phi_4 = -a[-a\tau_{22} + I_{03}\tau_{22}^2 + I_{30}\tau_{12}\tau_{11} + I_{21}(3\tau_{22}\tau_{21} + \tau_{11}\tau_{22} + 2\tau_{12}^2)] \; ;$$

$$I_{12} = n\Psi_2(\alpha + \beta) = I_{21} \; ;$$

$$I_{30} = -n[\Psi_2(\alpha) - \Psi_2(\alpha + \beta)] \; ; \quad I_{03} = -n[\Psi_2(\beta) - \Psi_2(\alpha + \beta)] \; ;$$

τ_{ij} 爲 $\begin{bmatrix} n[\Psi_1(\alpha) - \Psi_1(\alpha + \beta)] & -n\Psi_1(\alpha + \beta) \\ -n\Psi_1(\alpha + \beta) & n[\Psi_1(\beta) - \Psi_1(\alpha + \beta)] \end{bmatrix}$ 的反矩陣中第 ij 個元素。

(二)當 α, γ 未知並假設其事前分佈如式子(1)時兩者之貝氏估計式的近似解爲

$$\hat{\alpha}_{bs} \approx \alpha - \frac{\tau_{11}}{\alpha} - \frac{\tau_{12}}{\gamma} + \frac{1}{2}\Phi_1 \; ; \qquad\qquad \hat{\gamma}_{bs} \approx \gamma - \frac{\tau_{21}}{\alpha} - \frac{\tau_{22}}{\gamma} + \frac{1}{2}\Phi_2 \; ;$$

$$\hat{\alpha}_{bl} \approx \alpha - \frac{1}{a}\ln(1 + \frac{a\tau_{11}}{\alpha} + \frac{a\tau_{12}}{\gamma} + \frac{1}{2}\Phi_3) \; ; \quad \hat{\gamma}_{bl} \approx \gamma - \frac{1}{a}\ln(1 + \frac{a\tau_{21}}{\alpha} + \frac{a\tau_{22}}{\gamma} + \frac{1}{2}\Phi_4) \; ;$$

其中

$$\Phi_1 = I_{30}\tau_{11}^2 + I_{03}\tau_{21}\tau_{22} + I_{12}(\tau_{11}\tau_{22} + 2\tau_{21}^2) \; ;$$

$$\Phi_2 = I_{03}\tau_{22}^2 + I_{30}\tau_{12}\tau_{11} + 3I_{12}\tau_{21}\tau_{22} \; ;$$

$$\Phi_3 = -a[-a\tau_{11} + I_{30}\tau_{11}^2 + I_{03}\tau_{21}\tau_{22} + I_{12}(\tau_{11}\tau_{22} + 2\tau_{21}^2)] \; ;$$

$$\Phi_4 = -a[-a\tau_{22} + I_{03}\tau_{22}^2 + I_{30}\tau_{12}\tau_{11} + 3I_{12}\tau_{21}\tau_{22}] \; ;$$

$$l_{12} = -\frac{n}{\gamma^2} + \sum_{i=1}^{n}(\frac{x_i}{1-(1-\gamma)x_i})^2 \quad ; \qquad l_{21} = 0 \quad ;$$

$$l_{30} = -n[\Psi_2(\alpha) - \Psi_2(\alpha+\beta)] \quad ; \qquad l_{03} = \frac{2n\alpha}{\gamma^3} - 2(\alpha+\beta)\sum_{i=1}^{n}(\frac{x_i}{1-(1-\gamma)x_i})^3 \quad ;$$

τ_{ij} 爲
$$\begin{bmatrix} n[\Psi_1(\alpha) - \Psi_1(\alpha+\beta)] & -\frac{n}{\gamma} + \sum_{i=1}^{n}\frac{x_i}{1-(1-\gamma)x_i} \\ -\frac{n}{\gamma} + \sum_{i=1}^{n}\frac{x_i}{1-(1-\gamma)x_i} & \frac{n\alpha}{\gamma^2} - (\alpha+\beta)\sum_{i=1}^{n}\left(\frac{x_i}{1-(1-\gamma)x_i}\right)^2 \end{bmatrix}$$
的反矩陣中第 ij 個元

素。

(三) 當 β, γ 未知並假設其事前分佈如式子(1)時兩者之貝氏估計式的近似解爲

$$\hat{\beta}_{bs} \approx \beta - \frac{\tau_{11}}{\beta} - \frac{\tau_{12}}{\gamma} + \frac{1}{2}\Phi_1 \quad ; \qquad \hat{\gamma}_{bs} \approx \gamma - \frac{\tau_{21}}{\beta} - \frac{\tau_{22}}{\gamma} + \frac{1}{2}\Phi_2 \quad ;$$

$$\hat{\beta}_{bl} \approx \beta - \frac{1}{a}\ln(1 + \frac{a\tau_{11}}{\beta} + \frac{a\tau_{12}}{\gamma} + \frac{1}{2}\Phi_3) \quad ; \qquad \hat{\gamma}_{bl} \approx \gamma - \frac{1}{a}\ln(1 + \frac{a\tau_{21}}{\beta} + \frac{a\tau_{22}}{\gamma} + \frac{1}{2}\Phi_4) \quad ;$$

其中

$$\Phi_1 = l_{30}\tau_{11}^2 + l_{03}\tau_{21}\tau_{22} + l_{12}(\tau_{11}\tau_{22} + 2\tau_{21}^2) \quad ;$$

$$\Phi_2 = l_{03}\tau_{22}^2 + l_{30}\tau_{12}\tau_{11} + 3l_{12}\tau_{21}\tau_{22} \quad ;$$

$$\Phi_3 = -a[-a\tau_{11} + l_{30}\tau_{11}^2 + l_{03}\tau_{21}\tau_{22} + l_{12}(\tau_{11}\tau_{22} + 2\tau_{21}^2)] \quad ;$$

$$\Phi_4 = -a[-a\tau_{22} + l_{03}\tau_{22}^2 + l_{30}\tau_{12}\tau_{11} + 3l_{12}\tau_{21}\tau_{22}] \quad ;$$

$$l_{12} = \sum_{i=1}^{n}(\frac{x_i}{1-(1-\gamma)x_i})^2 \quad ; \qquad l_{21} = 0 \quad ;$$

$$l_{30} = -n[\Psi_2(\beta) - \Psi_2(\alpha+\beta)] \quad ; \qquad l_{03} = \frac{2n\alpha}{\gamma^3} - 2(\alpha+\beta)\sum_{i=1}^{n}(\frac{x_i}{1-(1-\gamma)x_i})^3 \quad ;$$

τ_{ij} 爲
$$\begin{bmatrix} n[\Psi_1(\beta) - \Psi_1(\alpha+\beta)] & \sum_{i=1}^{n}\frac{x_i}{1-(1-\gamma)x_i} \\ \sum_{i=1}^{n}\frac{x_i}{1-(1-\gamma)x_i} & \frac{n\alpha}{\gamma^2} - (\alpha+\beta)\sum_{i=1}^{n}\left(\frac{x_i}{1-(1-\gamma)x_i}\right)^2 \end{bmatrix}$$
的反矩陣中第 ij 個

元素。

　　Lindley 當初的想法是如果 MLE 不難找時可透過其求得貝氏估計式，因此將事後分佈對著 MLE 展開求之，故在以上所有貝氏估計式的表示法中，有關未知參數的部份均以其最大概似估計式代入。

3. 模擬研究

當三個參數均未知且相互獨立並具有前所設的事前分佈時，貝氏估計式為兩個複雜的三重積分相除，目前尚未導得較好的近似結果，因此本模擬研究將只針對一個或兩個參數均未知的情形討論。

3.1 參數設定

有關模擬實驗中樣本生成的部分，首先生成服從貝它分佈 $\text{Beta}(\alpha, \beta)$ 的亂數 W，再做 $\dfrac{W}{(1-\gamma)W + \gamma}$ 的轉換即得服從 $\text{G3B}(\alpha, \beta, \gamma)$ 分佈的亂數。模擬過程中我們考慮十種參數值，分別為 0.3、0.6、0.8、1.2、1.5、1.8、2、2.5、3、3.5；七種貝氏估計式分別以符號 BL(-10)、BL(-3)、BL(-1)、BS、BL(1)、BL(3)、BL(10)代表之，其中 BL(a_0)代表在 LINEX 損失函數定義中 a 的取值為 a_0 時所得的貝氏估計式；BS 代表在平方誤損失函數下的貝氏估計式。至於樣本數為 30, 50, 100, 300, 500；迭代次數為 1000。

本模擬實驗中，我們想探討如果決策者忽略了理論結果而選定均方差為風險函數之依據時，各種貝氏估計式所導致之相對風險 RMSE，其中 RMSE 定義為 MSE 除以真正的參數值。在本文圖表中我們亦將 MLE 一併列出。以下將對一個及二個參數未知的情況逐一討論。

在一個參數未知的情況下，有關於積分的部份我們採用 importance sampling[8]方法來估計，即

$$\hat{\theta}_{bs} = \frac{\int_0^\infty p(\theta|\underline{x})d\theta}{c} \approx \sum_{j=1}^m \frac{p(\theta_j|\underline{x})}{g(\theta_j)} \Big/ \sum_{j=1}^m \frac{p(\theta_j|\underline{x})}{\theta_j g(\theta_j)} \ ,$$

$$\hat{\theta}_{bl} = -\frac{1}{a}\ln\{\frac{1}{c}\int_0^\infty \frac{p(\theta|\underline{x})}{\theta}e^{-a\theta}d\theta\} \approx -\frac{1}{a}\ln\{\sum_{j=1}^m \frac{p(\theta_j|\underline{x})e^{-a\theta_j}}{\theta_j g(\theta_j)} \Big/ \sum_{j=1}^m \frac{p(\theta_j|\underline{x})}{\theta_j g(\theta_j)}\} \ ,$$

其中 g 是參數為 1 的指數分佈的 pdf；m 取 50000。

在兩個未知參數的情況下，因為在估計式的表示法中牽涉到兩個複雜的雙重積分比，因此我們使用 Lindley[7] 的近似方法來求得貝氏估計式。在貝氏估計式的表示法中，未知參數的部份均以最大概似估計式代入。

3.2 模擬結果

3.2.1 一個參數未知

圖 1 為一個參數未知的情況下在不同的樣本數時八種估計式之 RMSE 的模擬結果,其中 x 軸為估計式（軸上分別以 1,… ,8 來表示 MLE，BL(-10), …,BL(10)等八種估計式），y軸為未知參數之真正值，z 軸為各估計式之 RMSE。圖 1 中第一，二，三欄分別代表當未知參數分別為 α, β, γ 時，在各種樣本數之下估計式之 RMSE。但在 γ 未知的情形之下，因 BL(-10)及 BL(-3)所算出之 RMSE 較其他六種估計式所得之 RMSE 大很多，為了圖示方便起見，在第三欄的五個圖中均未畫出這兩個估計式的相對位置。

總而言之，根據模擬的結果，七種貝氏估計式所得之 RMSE 的最大值總是出現於估計式 BL(-10)；當參數值較小時，各估計式的 RMSE 值均相當接近。當未知參數之真正值越大時，其 RMSE 圖形逐漸呈 U 型曲線。根據模擬數據，我們發現隨著參數值的增加，最佳貝氏估計式將由 BL(10)慢慢的轉變為 BL(1)，即最佳貝氏估計式會隨著參數值的不同而有所改變。

其次觀察特定的估計式，當最後的風險比較準則所憑藉之損失函數改變時其相對風險的變化。由圖 2，我們發現相對風險曲線呈現 W 型，即當損失函數從平方誤損失函數換成 LINEX 損失函數 LX(-1)及 LX(1)時，相對風險值將稍微降低，但若是採用 LINEX 損失函數 LX(-3)及 LX(3)時，相對風險值將較前三者為大；也就是說若決策者以 LINEX 損失函數為基礎時，針對同一個估計式與採用平方誤損失函數相較，所得之 RMSE 值有可能產生高估或低估的結果。

因此除了慎選估計式之外，決策者必須也要衡量風險函數對最後決策所產生的影響。

圖 3 為樣本數為 500 時，八種估計式之盒狀圖。我們發現估計式 BL(-10)、BL(-3)、BL(-1)的中位數均大於真正值，且隨著 a_0 的增加偏差值(bias)越小。而 BL(1)、BL(3)、BL(10)的中位數均小於參數的真正值且隨著 a_0 值的增加差異越大，這意味著當 $a_0 < 0$ 時，LINEX 型的貝氏估計式將會有高估的可能；而當 $a_0 > 0$ 時 LINEX 型的貝氏估計式將會有低估的可能。另一方面，當 $|a_0|$ 的值愈大時，其高低估的情形將會更嚴重。之前我們提到七種貝氏估計式的 RMSE 圖形呈現 U 型曲線，在這裡的現象可以得到合理的解釋。至於估計式 BS 所造成的偏差雖大部分為正，但其偏差值似乎都在可忽略的範圍內。至於小樣本，如樣本數為 30 時，除了其四分位距(mid-range)較大樣本時為大，資料較分散且具有較多之離群點(outlier)外，其餘現象與大樣本時無異。
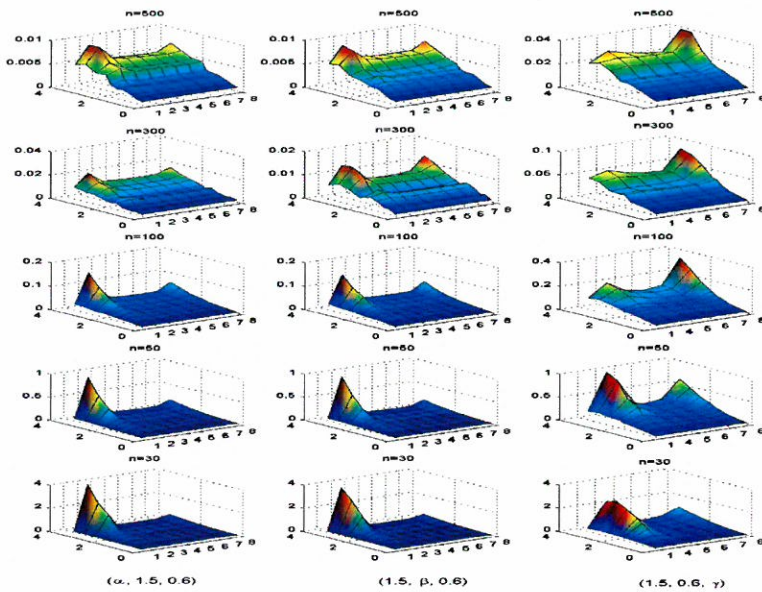
圖一　當一個參數未知時各估計式的 RMSE

註： (1) x 軸代表八種估計式(1～8)；y 軸代表參數值(0～4)；z 軸代表 RMSE 值。
　　 (2) 第一行的五個小圖為 α 未知，β =1.5，γ =0.6 的結果。
　　 (3) 第二行的五個小圖為 β 未知，α =1.5，γ =0.6 的結果。
　　 (4) 第三行的五個小圖為 γ 未知，α =1.5，β =0.6 的結果；由於估計式 BL(-10)（代號：2）與 BL(-3)（代號：3）的 RMSE 值太大，所以並未放入圖中。
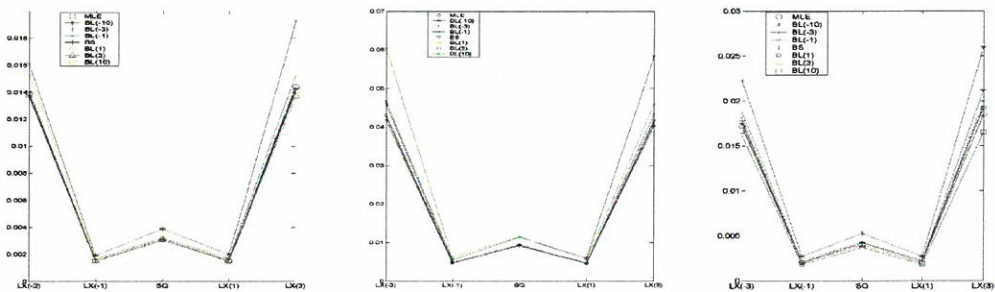
(c): α 未知（真正值為 1.5）　　(b): β 未知（真正值為 2.5）　　(c): γ 未知（真正值為 1.2）
　　β =1.5, γ =0.6　　　　　　　　α =1.5, γ =0.6　　　　　　　　α =1.5, β =0.6

圖二：一個參數未知，同一估計式在不同損失函數下其相對風險之比較

註：x 軸上有五種損失函數，LX(a_0)代表 LINEX 損失函數中參數 $a = a_0$；SQ 代表平方誤損失函數。y 軸為相對風險值。樣本數為 500。

3.2.2 兩個參數未知

　　圖 4～圖 6 為兩個參數未知且樣本數分別為 30，50 及 100 時的情形。圖中 x 軸仍代表估計式，y 軸則為其中一個未知參數，而不同的圖則表示另一個未知參數不同假設值之情形，z 軸仍表示在各種組合情形下的 RMSE。有關顏色的部分，紅色區域代表 RMSE 值較大的地方，反之藍色代表 RMSE 值較小的地方。

　　當 α, β 未知時根據圖 4 可以發現當 γ =2 時，不同的 (α, β) 之組合所得之圖形其 z 軸的最大刻度隨著樣本數的增加而減小，這代表各估計式所產生之 RMSE 的確受到樣本數影響著；此外，不難發現每張圖紅色的區域最常出現在估計式 2，3 或 4，且當參數值越大時這種情形越明顯，這代表 BL(-10)、BL(-3)、BL(-1)的估計效果是比其他估計式的效果來得差；最小值發生的地方則隨著參數值的不同而改變，但這點從圖中較難看出。表 1 則為不同參數範圍下且樣本數各為 50 與 500 時最佳貝氏估計式（即 RMSE 最小者）與 MLE 的比較：我們不難發現隨著參數值的增大，最佳貝氏估計式由 BL(10)逐漸換成 BL(1)或者 BS。這顯示出當參數值愈大時，損失函數不對稱性的現象愈弱；即當參數值大時，平方誤損失函數應是個適當的選擇。至於最大概似估計式，雖然其 RMSE 相對來說比最佳貝氏估計式來得大些，但是透過模擬結果顯示，當樣本數增加時，MLE 與最佳貝氏估計式所得之 RMSE 的差距逐漸縮小，如在樣本數為 500 時，兩者之差距最多僅在千分位而已；因為模擬過程相當耗時，在本研究中並未持續加大樣本數，但可以預料到的，當樣本數大到某個程度時 MLE 與最佳貝氏估計式的估計效果應相當才是。

表 1：當 γ =2 時，(α, β)的最佳貝氏估計式,及該估計式與最大概似估計式之 RMSE 之比較

樣本數=30	β 範圍			
α 範圍	0～1	1～2	2～3	3～3.5
0～1	BL(10) or BL(3) (+,.06)	BL(3) (+,.15)	BL(3) or BL(1) (+,.17)	BL(1) (+,.01)
1～2	BL(3) (+,.16)	BL(3) (+,.13)	BL(1) (+,.12)	BS (+,.01)
2～3	BL(1) (+,.11)	BL(1) (+,.12)	BL(1) (+,.14)	BL(1) or BS (+,.03)
3～3.5	BL(1) (+, .11)	BL(1) (+, .12)	BL(1) (+, .14)	BL(1) or BS (+, .03)

樣本數=500	β 範圍			
α 範圍	0～1	1～2	2～3	3～3.5
0～1	BL(10) (+,.0014)	BL(10) or BL(3) (+,.0012)	BL(3) (+, .0016)	BL(3) or BL(1) (+,.0014)
1～2	BL(10) or BL(3) (+,.0011)	BL(3) (+,.0007)	BL(1) (+,.0008)	BL(1) (+,.0007)
2～3	BL(3) (+,.002)	BL(3) or BL(1) (+,.001)	BL(3) or BL(1) (+,.001)	BL(1) (+,.001)
3～3.5	BL(1) (+,.001)	BL(1) (+,.0006)	BL(1) (+,.0008)	BL(1) (+,.0008)

註[*]：BL()代表 7 個貝氏估計式中具有最小 RMSE 值之估計式，即最佳貝氏估計式。

註[**]：$(\pm, d)$ +代表 MLE 的 RMSE 大於最佳貝氏估計式的 RMSE；\\

　　　-代表 MLE 的 RMSE 小於最佳貝氏估計式的 RMSE；\\

　　　$\pm$ 代表兩類估計式無特定大小關係；\\

　　　d 代表|MLE 的 RMSE - 最佳貝氏估計式的 RMSE|。
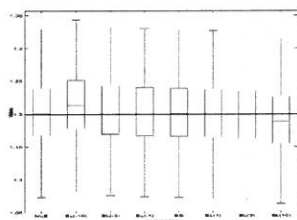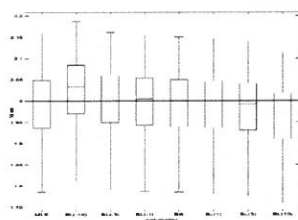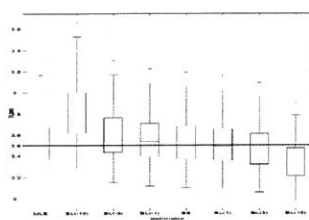
(a): α 未知, β =1.5, γ =0.6　　(b): β 未知, α =1.5, γ =0.6　　(c): γ 未知, α =1.5, β =0.6

圖三：一個參數未知，樣本數為 500 且迭代次數 1000 時八種估計式之盒狀圖

註：圖中水平線代表未知參數的真正值。

　　當 α, γ 未知時，所呈現的結果與上述情形類似。根據圖 5，發現在小樣本如 30 或 50 時，紅色區域發生在估計式 3、4、5、這代表在小樣本時 BL(-3)、BL(-1)、BS 的估計效果是比其他估計式來得差；而當大樣本時，紅色區域則出現於估計式 2、3、4，這表示 BL(-10)、BL(-3)、BL(-1)的估計效果是比其他估計式來得差。表 2 則列出不同參數範圍下之最佳貝氏估計式，我們發現最佳貝氏估計式隨著參數值的增大而由 BL(10)轉變成

BL(1)；MLE 的估計效果雖然還是比最佳貝氏估計式的估計效果差，但是其差距至多爲百分之三。相信只要持續加大樣本數，MLE 的估計效果應可媲美最佳貝氏估計式。

表 2：當 $\beta=2$ 時，α,γ 的最佳貝氏估計式，及該估計式與最大概似估計式 RMSE 之比較

樣本數=30	γ 範圍			
α 範圍	0~1	1~2	2~3	3~3.5
0~1	BL(10) or BL(3) (+, .35)	BL(3) or BL(1) (+, .41)	BL(1) (+, .2)	BS (±, .02)
1~2	BL(3) (+, .73)	BL(3) or BL(1) (+, 1)	BL(1) (+, .4)	BL(1) or BS (±, .1)
2~3	BL(10) or BL(3) (+, .33)	BL(1) (+, .8)	BL(1) (+, .6)	BL(1) (−, .07)
3~3.5	BL(1) (−, .09)	BL(1) (±, .03)	BL(1) (+, .15)	BL(1) (+, .03)
樣本數=500	γ 範圍			
α 範圍	0~1	1~2	2~3	3~3.5
0~1	BL(10) (+, .0023)	BL(3) (+, .005)	BL(3) or BL(1) (+, .007)	BL(1) (+, .0015)
1~2	BL(10) or BL(3) (+, .0004)	BL(3) (+, .012)	BL(3) (+, .02)	BL(1) (+, .003)
2~3	BL(3) (+, .018)	BL(3) (+, .02)	BL(3) (+, .03)	BL(1) (+, .007)
3~3.5	BL(1) (+, .004)	BL(1) (+, .006)	BL(3) or BL(1) (+, .02)	BL(1) (+, .02)

註[*]：BL()代表 7 個貝氏估計式中具有最小 RMSE 值之估計式，即最佳貝氏估計式。

註[**]：$(\pm. d)$ +代表 MLE 的 RMSE 大於最佳貝氏估計式的 RMSE；

　　　　-代表 MLE 的 RMSE 小於最佳貝氏估計式的 RMSE；

　　　　± 代表兩類估計式無特定大小關係；

　　　　d 代表|MLE 的 RMSE - 最佳貝氏估計式的 RMSE|。

　　當 β, γ 未知時，根據圖 6，發現在小樣本如 30 或 50 時，紅色區域發生在估計式 3、4、5 這代表 BL(-3)、BL(-1)、BS 的估計效果是比其他估計式來得差；而當大樣本時，紅色區域則出現於估計式 2、3、4 這表示 BL(-10)、BL(-3)、BL(-1)的估計效果是比其他估計式來得差，這與 α, γ 未知時的估計相同。由模擬數據我們不難發現隨著參數值的增大，最佳貝氏估計式將由 BL(10)換成 BL(1)，值得注意的是這種情形在樣本數為 30 時並不穩定；而 MLE 的估計效果則明顯的表現於大樣本時，雖然還是比貝氏估計式中的最小值大，但是其差距至多為百分之二。

　　因為考慮兩個未知參數，所以估計式的分佈圖應該為一個 x,y 軸為兩未知參數，z 軸為估計值個數的 3D 圖，但若將此圖投影至 x-y 平面，則會與散佈圖的輪廓類似。圖 7，圖 8，圖 9 分別代表 α, β 未知，α, γ 未知，β, γ 未知下，樣本數為 500，八種估計式的散佈圖，橫軸與縱軸為兩未知參數。由於資料過多且其圖型趨勢皆類似，故我們只展示出兩種參數組合的情況。首先從散佈圖的形狀來看，圖 7 與圖 8 圖形似乎為長軸斜率大於 0 的橢圓，這代表 α, β 未知時 $\hat{\alpha}$ 與 $\hat{\beta}$ 呈現正相關，α, γ 未知時 $\hat{\alpha}$ 與 $\hat{\gamma}$ 呈現正相關；圖 9-(b)的圖形與長軸斜率小於 0 的橢圓有些差距，不過其兩未知參數的真正值頗大，顯示出需要更多的樣本數才能使其估計效果更佳；而估計式 BL(-10)、BL(-3)、BL(-1)、BL(3)、BL(10)幾乎完全偏離真正值，這與前文所提的當參數愈大時，最佳估計式逐漸換成 BS 或 BL(1)的結果一致。

4. 結論

　　根據理論，貝氏估計式乃是具有最小貝氏風險者，本文不對此做驗證。本文主要討論若決策者選取一般的風險函數而非討論貝氏風險的情形下，八種估計式中是否存在最佳估計式（即 RMSE 最小者）。根據模擬的結果，無論是一個參數未知或者兩個參數未知時，我們發現最佳貝氏估計式會隨著未知參數真正值的大小而改變，而最大概似估計式的 RMSE 與最佳貝氏估計式之 RMSE 的差距亦隨著樣本數的增加而減小，當樣本數為 500 時，最大概似估計式與最佳貝氏估計式的估計效果相當。換言之，對於所有未知參數的可能值並不存在最佳估計式。若樣本數夠大時，因為最大概似估計式與最佳貝氏估計式表現相當，所以在不同估計式所需的運算時間考量之下，尋找某參數的最佳估計式時，我們傾向推薦最大概似估計式。

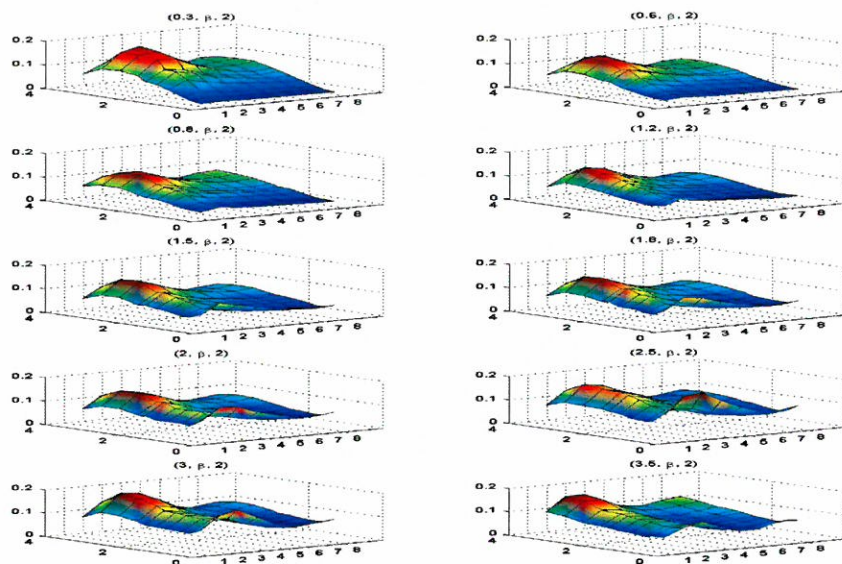　　因為對於貝氏估計式我們只考慮 improper-informative prior，所以我們並無法得知如果參數的事前分佈為其它種情形時，結論是否也相同。然而，若決策者能根據過去的經

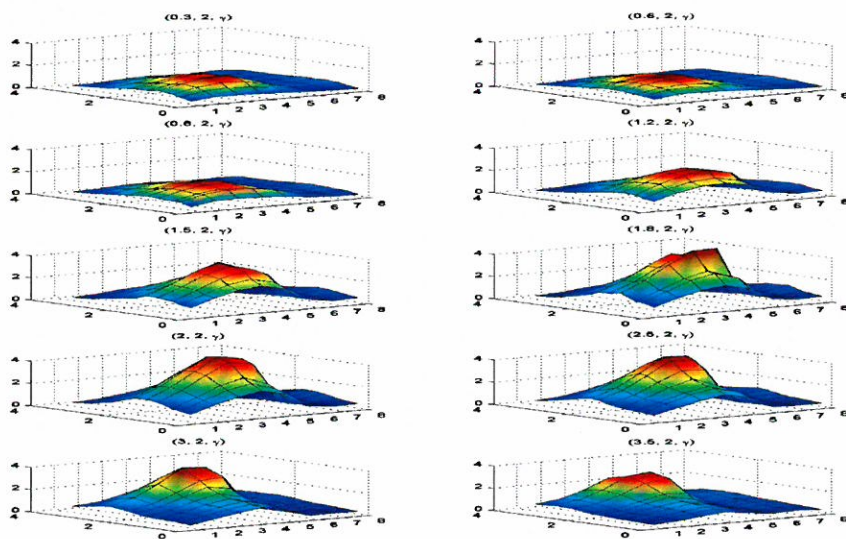驗選定適當的事前分佈後，仍然可依本文的分析方式討論以取得最合適的估計式。
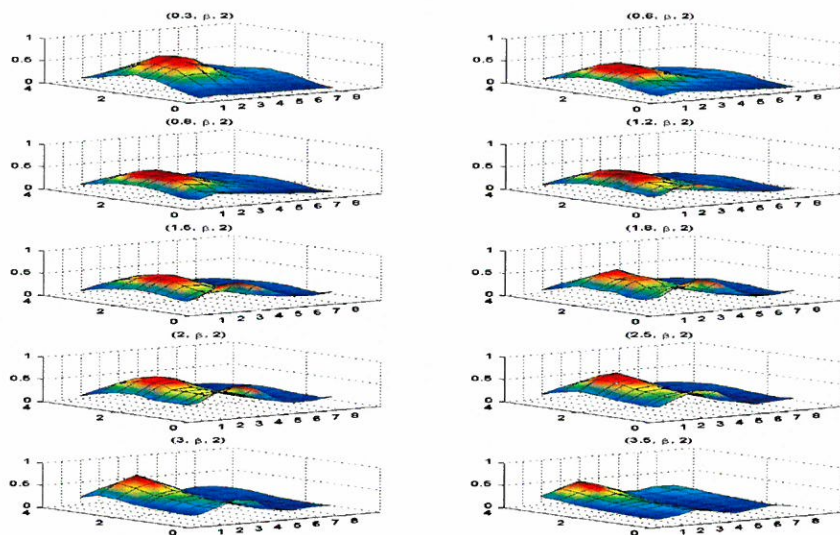
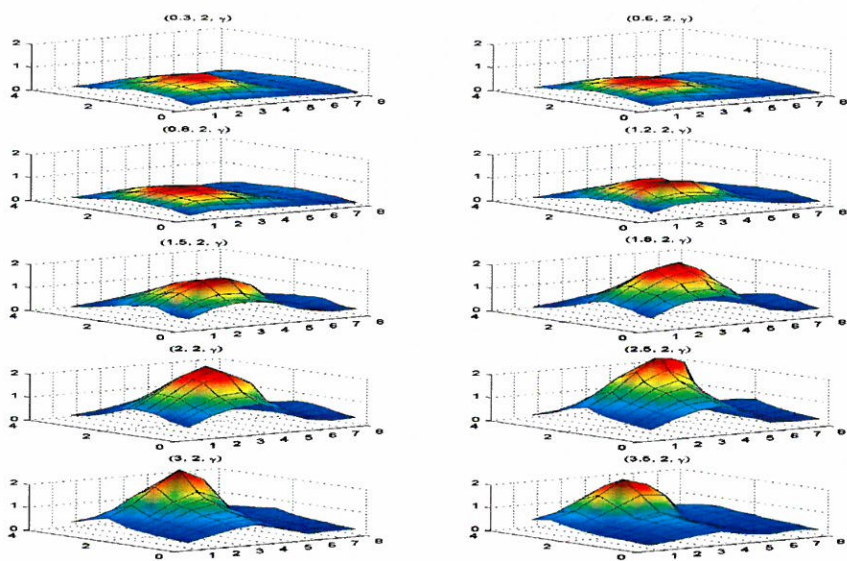圖四-(a)　樣本數為 30
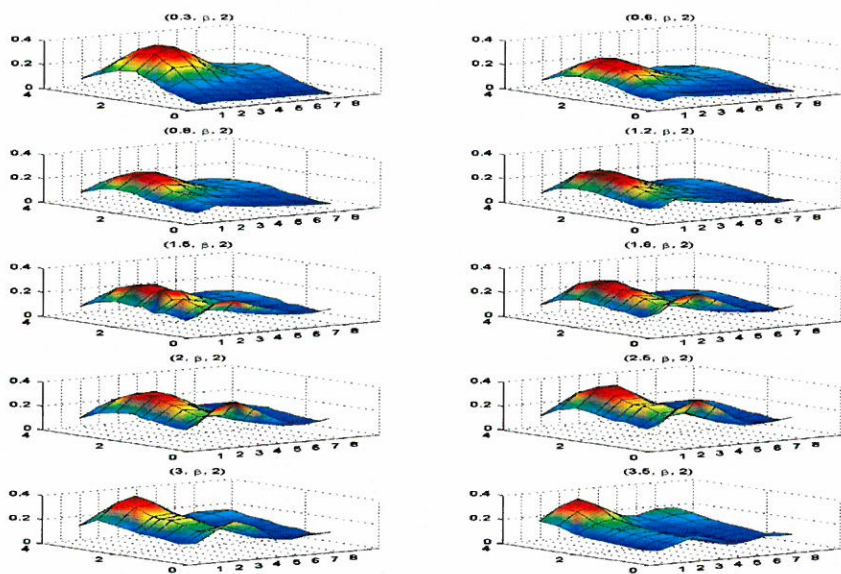
圖四-(b)　樣本數為 50

圖四-(c)　　樣本數為 100

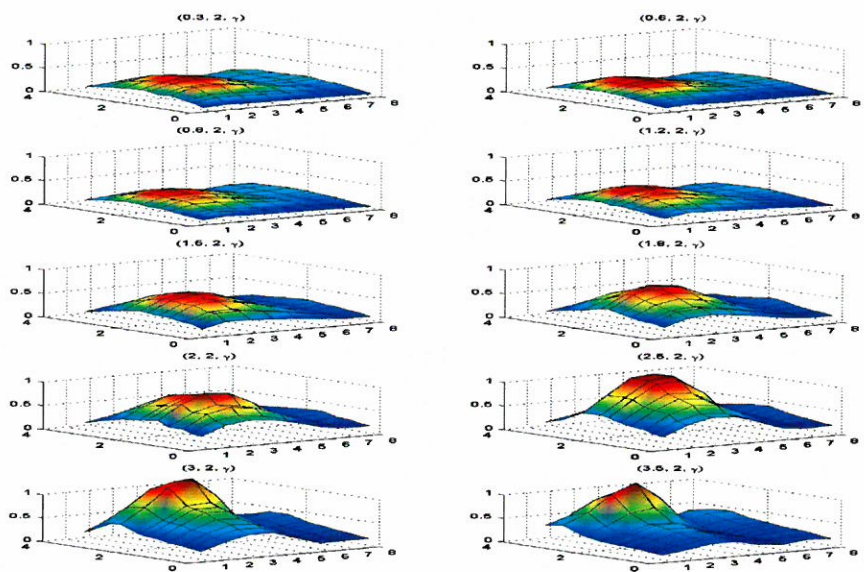圖四　　$\gamma = 2$ 且 α, β 未知時，八種估計式之 RMSE 比較

【註：圖四我們考慮 α, β =0.3, 0.6, 0.8, 1.2, 1.5, 1.8, 2.0, 2.5, 3.0, 3.5 的情形。】
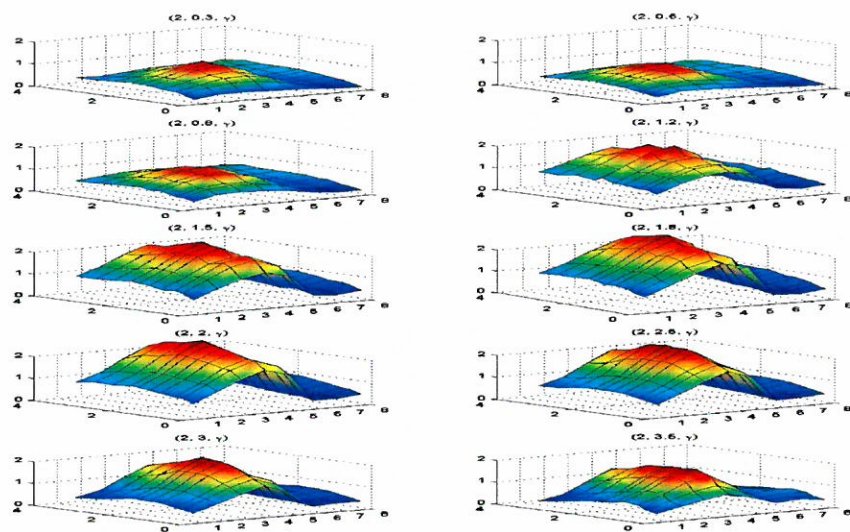

圖五-(a)　　樣本數為 30

圖五-(b)　　樣本數為 50

圖五-(c)　　樣本數為 100
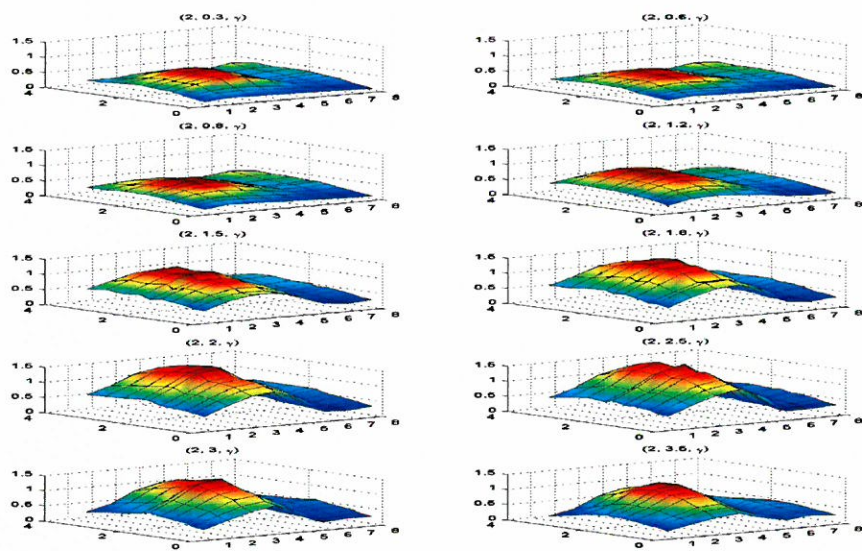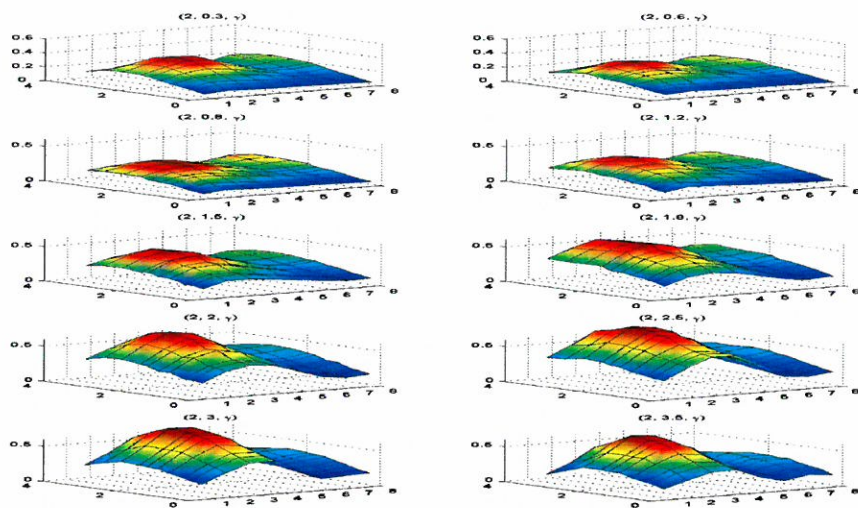
圖五　　β =2 且 α, γ 未知時八種估計式之 RMSE 比較

【註　　圖五我們考慮 α, γ =0.3, 0.6, 0.8, 1.2, 1.5, 1.8, 2.0, 2.5, 3.0, 3.5。】
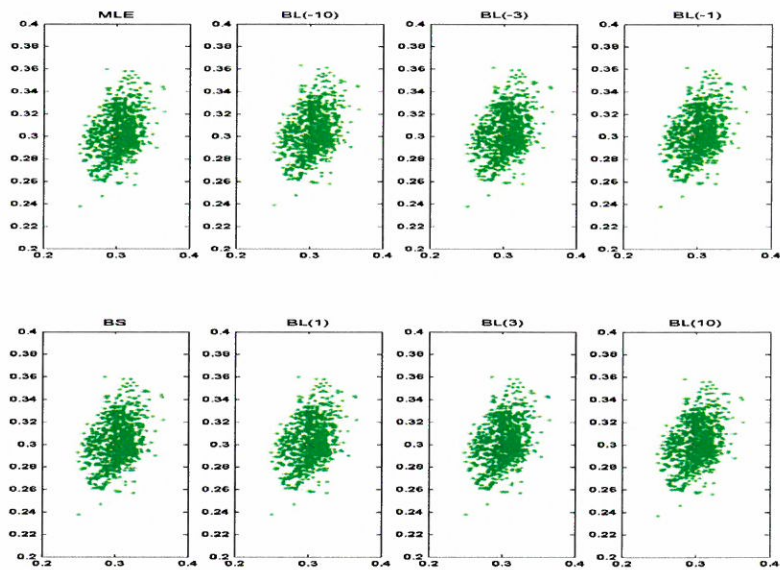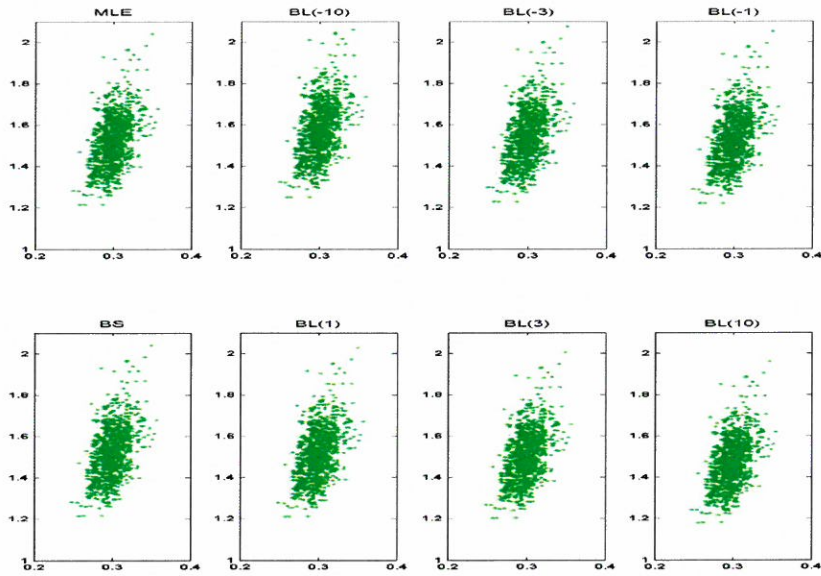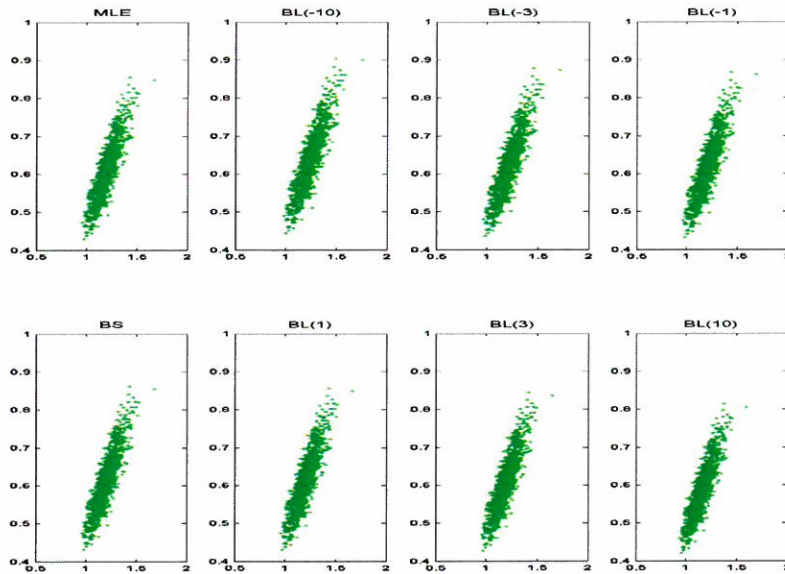
圖六-(a)　　樣本數為 30

圖六-(b)　　樣本數為 50

圖六-(c)　樣本數為 100

圖六　α =2 且 β, γ 未知時八種估計式之 RMSE 比較

【註　圖六考慮 β, γ　=0.3, 0.6, 0.8, 1.2, 1.5, 1.8, 2.0, 2.5, 3.0, 3.5】

圖七-(a)　(α, β)=(0.3,0.3)【註：$sd(\hat{\alpha}_{ML}) = sd(\hat{\beta}_{ML})$ =0.0168】．

圖七-(b) $(\alpha, \beta)=(0.3,1.5)$【註：x 軸為 α 值，y 軸為 β 值；sd 為標準差。】

【註：$sd(\hat{\alpha}_{ML})$ =0.0151，$sd(\hat{\beta}_{ML})$ =0.1152. γ =2 且 α, β 未知時八種估計式之散佈圖，樣本數為 500】

圖八-(a) $(\alpha, \gamma)=(1.2,0.6)$【註：$sd(\hat{\alpha}_{ML})$ =0.0959, $sd(\hat{\gamma}_{ML})$ =0.0723】
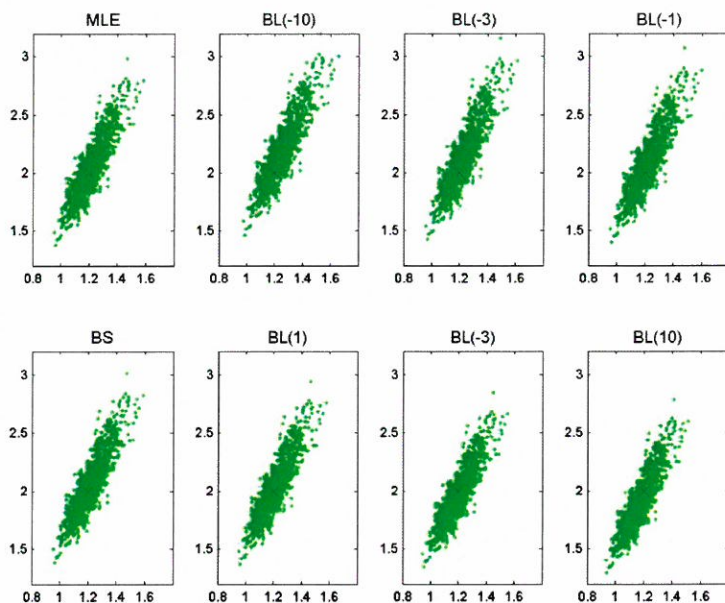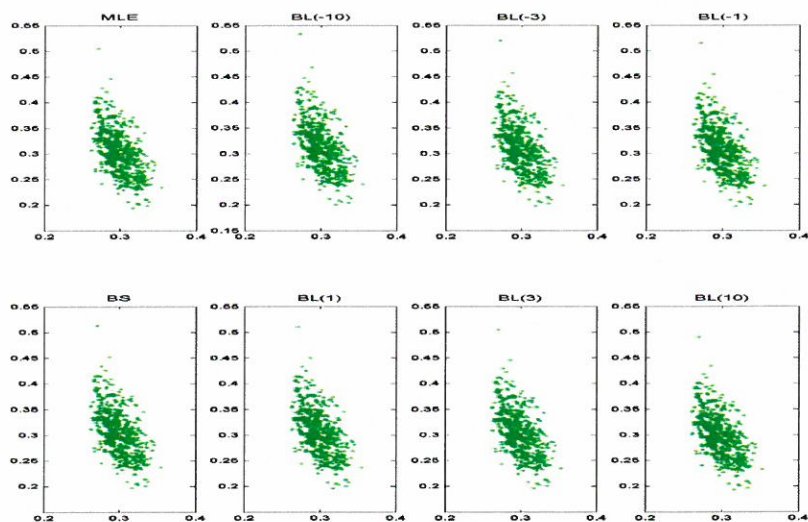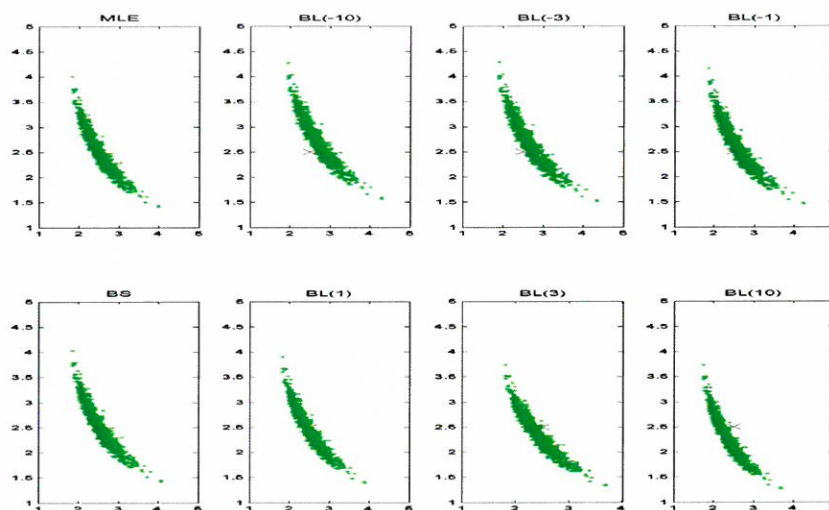
圖八-(b)　(α,γ)=(1.2,2.0)【註：x 軸為 α 值，y 軸為 γ 值；sd 為標準差。】

【註：$sd(\hat{\alpha}_{ML})$=0.0958,　$sd(\hat{\gamma}_{ML})$=0.2407. β=2 且 α,γ 未知時八種估計式之散佈圖，樣本數為 500】

圖九-(a): (β,γ)=(0.3,0.3)【註: $sd(\hat{\beta}_{ML})$=0.0163,　$sd(\hat{\gamma}_{ML})$ =0.0392】

圖九(b): (β, γ)=(2.5,2.5)【註: x 軸為 β 值, y 軸為 γ 值; sd 為標準差。】

【註: $sd(\hat{\beta}_{ML})$ =0.2867, $sd(\hat{\gamma}_{ML})$ =0.3695. α =2 且 β , γ 未知時八種估計式之散佈圖,樣本數為 500】

參考文獻

[1] Abramowitz, M. and I. A. Stegun (1965), Handbook of Mathematical Functions, Dover Publications, Sections 6.3 and 6.4。

[2] J. J. Chen and M. R. Novick (1984),``Bayesian analysis for binomial models with generalized beta prior distribution'', Journal of Educational Statistics, 9, 163-175。

[3] Bonnie Kegan and Webster West (2005), ``Modeling the simple epidemic with deterministic differential equations and random initial conditions'', Mathematical Biosciences, 195, 179-193。

[4] D. L. Libby (1981), ``Multivariate fixed state utility assemessment'', PhD dissertation, University of Iowa, Iowa City。

[5] D. L. Libby and M. R. Novick (1982), ``Multivariate generalized beta distributions with applications to utility assessment'', Journal of Educational Statistics, 7(4), 271-294。

[6] E. L. Lehmann (1983), Theory of point estimation, New York Wiley。

[7] D. V. Lindley (1980), "Approximate Bayesian methods", Trabajos Estadistica, 31, 223-237。

[8]　Christian P. Robert and George Casella (2004), Monte Carlo Statistical Methods, second edition, Springer。

[9]　M. Sahinoglu (1981), ``Statistical inference on the reliability performance index for electric power generation systems", PhD dissertation, Institute of statistics, College Station, Texas A&M University。

[10] M. Sahinoglu and D. L. Libby and S. R. Das (2005), ``Measuring Availability Indices with Small Samples for Component and Network Reliability using the Sahinoglu-Libby Probability Model", IEEE, Instrumentation and Measurement, 54(3), June。

[11] A. Zellner (1986), ``Bayesian estimation and prediction using asymmetric loss function", Journal of the American Statistical Association, 81(394), 446-451。

An Estimating Problem on Generalized Beta Distribution

Wei-Ti Chen and Sy-Mien Chen

Institute of Mathematics and Department of Mathematics

Fu-Jen Catholic University, Taipei, Taiwan, R.O.C.

Abstract

As we know, the Bayes estimator is optimal under Bayes risk. In this research, we study the performance of several estimators of G3B parameters based on the risk under squared error loss function.

可依據影像特性自我調適之皮膚檢測系統

孫宏明　　王意婷[1]

開南大學資訊管理學系

摘　　要

當影像曝光過度（太亮）或不足（太暗）時，會影響膚色的呈現，因而造成皮膚檢測率的降低。為了解決這個問題，我們提出了一個可自我調適的皮膚檢測方法。它藉由收集影像中最有可能是皮膚的像素，並根據這些像素來適度地調整膚色模型，以克服在不同的曝光條件之下，膚色會有不同變化的問題。藉由測試超過 13000 張的影像（包含訓練和測試的影像），實驗結果顯示我們方法的準確性明顯優於原來的方法。

關鍵字：皮膚檢測；膚色模型；顏色分類；貝式分類法

1.前　言

當要分析影像中的人體時，第一個處理步驟通常就是皮膚檢測，目的是為了找出影像中的人體以便進行分析，它的應用包括人臉檢測和辨識、姿勢分析、影像內容分類…等。在理論上來說，許多不同的特徵，像是顏色、形狀和紋理，都可以用來在影像中找到有關人體的目標。但是人類的皮膚在影像中，通常不會呈現明顯的紋理特徵。而且由於身體姿勢的不同、穿著衣服的方式和可能會擋住皮膚的周圍物體（像是一些飾品），都可能使得身體皮膚的形狀會有較多不同的變化，相較之下，人體的膚色變化則比較穩定和容易預測。雖然人體皮膚的顏色可能根據種族、環境、曝光條件和陰影而有所不同，但是之前的研究中指出[1,2]，人體皮膚的顏色一般集中在色彩空間中的一定範圍之

內，而且有規則的分佈在色彩空間之中。此外，Storring 等人[3]的研究指出，在不同曝光條件下的皮膚顏色可以用物理的方法來表示。因此，與皮膚的形狀和紋理等特徵相比，膚色是比較可靠且穩定的特徵，所以在大部份的皮膚檢測技術中，都會採用膚色來作為檢測皮膚的依據。

皮膚檢測基本上是一個二元分類的問題：影像中的每個像素，根據特定的決策模式，指派給皮膚類別或是非皮膚類別。在相關的文獻中，我們可以找到許多分類的方法都可以用來解決這個問題，包括設定皮膚色彩臨界值、貝式分類法、類神經網路、最大亂度分類法……等[4]。

設定皮膚色彩臨界值[5-7]是一種簡單的皮膚檢測技術，它定義出皮膚顏色存在於色彩空間中的一個區域或是多個區域，如果某個像素的顏色落入這個區域，這個像素就會被標示為皮膚。這是一種非常快速的方法，而且它只需要很少的記憶體儲存空間，因為只有幾個分類的決策規則需要加以儲存和檢查。但是這個方法有一個缺點，由於決策規則在系統中是固定的，所以這種辨識方式比較缺乏彈性。

類神經網路則利用訓練的方式，讓系統自動學習如何進行資料分類[8-10]。它的效能取決於每個隱藏層中的節點數目，為了要得到最佳的效果，網路的結構需要仔細的調整。此外，如果要訓練的資料量很大（舉例來說，在我們的皮膚和非皮膚影像資料庫中，有將近 20 億個像素），在訓練類神經網路的過程中，將會花費大量的時間。Zheng 等人[11]採用最大亂度模型來檢測影像中的皮膚，藉由在每個像素之鄰接像素的色彩梯度加上限制條件，和使用貝斯樹狀表示法(Bethe tree approximation)以及信賴度傳遞演算法(belief propagation algorithm)來計算像素可能為皮膚的機率，這個方法需要處理六個色彩的直方圖，因此比較耗費記憶體空間。

與上述的技術相比，貝式分類法提供了一個更適合用來處理大量訓練資料的方法。貝氏分類法的決策策略是根據兩個類別的概似函數做計算，因為皮膚類別和非皮膚類別的概似函數（也就是色彩空間中的統計分佈模型），只需要掃描一次訓練資料即可求得，所以它的訓練過程是非常快速的。

Jones 等人[1]從網際網路上收集了 18696 張照片，總共包含將近 20 億個像素，並以人工的方式來分離包含皮膚和不包含皮膚的影像，並標示出皮膚影像中的皮膚像素，然後藉由分別掃描所有的皮膚像素和非皮膚像素，最後計算出膚色和非膚色的色彩分佈模型。當給定一個色彩時，藉由計算其膚色概似值與非膚色概似值的比率並和一個臨界值做比較，來決定此色彩是否為膚色。這是一個執行速度很快的方法。不過這個方法需要

一些記憶體空間來儲存膚色和非膚色的色彩分佈模型。許多其他的皮膚檢測系統也有採用類似的做法[12-14]。

為了要減少記憶體需求，並能從少量的訓練資料中得到一般化的分佈模型，一些研究[15-17]也使用高斯函數來表示皮膚和非皮膚的色彩分佈模型。使用高斯函數表示膚色和非膚色的分佈模型稱為參數化建模；而前述基於統計分佈模型的方法則是所謂的非參數建模。在文獻中也針對參數化建模和非參數建模的效果加以比較[1，18]，實驗顯示當訓練的資料數量較少的時候，參數化建模的準確性比較好；但是當訓練的資料數量較多的時候，非參數化建模則較佳。

在早期有關皮膚檢測的研究文獻中，不論是處理曝光過度（太亮）、曝光正常或是曝光不足（太暗）的影像，都是使用同一個膚色模型，如此將導致影像太亮和太暗時，正確率便會明顯降低。因為無論是參數或非參數建模方法，皮膚和非皮膚的色彩分佈模型的計算，皆來自整個影像資料庫中的訓練樣本。換句話說，皮膚和非皮膚色彩分佈模型是總體的統計資料，當應用它們為影像中的皮膚做檢測的時候，其準確性會因為影像的亮度而改變，如果影像的曝光條件良好，那麼其中的皮膚色彩分佈和總體統計得到的皮膚和非皮膚的色彩模型會比較吻合，使得皮膚檢測的準確性較佳；相反地，如果影像的曝光條件不良，皮膚檢測的準確性將會明顯的降低，因為皮膚顏色的分佈與總體統計出來的資料有著明顯的差異。為了能夠處理不同的曝光條件下所導致皮膚色彩模型的變化，我們可以使用動態調適技術。

Yang 等人[2]提出一個用來在影片中做人臉追蹤的可調適皮膚色彩模型。他們使用 Q-Q plot 方法，以驗證皮膚色彩分佈是否真的符合多變量高斯分佈。在人臉追蹤的過程中，則以一組權重因子，依照前一個影格的皮膚色彩分佈情況，使用最大概似值準則來計算高斯分佈的線性組合。Mckenna 等人[19]使用高斯混合模型在 HS 色彩空間中表示人臉的色彩分佈。這個模型會隨著處理過程而演變。在影格 t 中，藉由將一特定矩形搜尋區域內的色彩機率加上影格 t-1 中的平均值和標準差來求得。Sigal 等人[20]所提出的方法是藉由目前的檢測結果和一個二階 Markov 模型的輸出，來動態更新皮膚色彩分佈模型。皮膚色彩分佈模型的演變是以平移、縮放和旋轉的參數表示。Oliver 等人[21]的皮膚色彩分佈則是由分割出的皮膚區塊中取得，並以混合高斯分佈模型表示。一個漸近式的 EM 演算法用來在人臉追蹤期間持續地更新高斯混合模型的參數。上述的方法是利用連續影格之間的關聯性來調整膚色分佈模型。但是對於任意兩個獨立的影像來說，他們之間通常不具備關聯性，因此，唯一可以使用的資訊，只有在影像本身中。

　　Bergasa 等人[22]提出一個可調適的皮膚檢測方法，他們先從像素的分類開始。爲了簡化分類程序，事先假設膚色是影像中的主要色彩之一，且每個色彩群組的共變異矩陣是相等的。根據以上兩個假設，分類可以透過一組辨識函式來完成，且每個辨識函式的組成皆只有平均向量。Chahir 等人[23]使用和 Bergasa 等人類似的方法，首先透過改良的 Fuzzy c-means 演算法將影像中的像素分成數個群組，分組過程中所使用的特徵包括 HSV 色彩值和光譜分佈。將像素依色彩分組之後，再挑出屬於皮膚的群組。

　　Lee 等人[24]使用一個合併／分組演算法，從所收集的裸體影像中的皮膚色彩獲得五個皮膚的色彩群組。然後從這五個皮膚色彩群組產生五個皮膚色彩分佈模型。對於一個輸入的影像，先在五個固定的區域內抽取特徵值，這些特徵值再輸入五個預先訓練好的類神經網路，去決定出一個適合的皮膚色彩分佈模型。這個方法的正確性取決於從五個固定的區域所取得的色彩樣本。如果在這些區域中沒有皮膚或只有少量的皮膚存在，則可能會選擇出不正確的膚色分佈模型。

　　本篇論文提出了一個在單一影像中檢測皮膚的新方法，這個方法能適應由不同的曝光條件或種族所造成不同的膚色。首先，從大量的訓練影像資料庫中建構出皮膚和非皮膚色彩模型，並且將這兩個模型稱爲初步訓練的色彩模型。這兩個模型可以用來在一個影像中，挑選出最有可能是皮膚的像素，然後我們再利用所選取的皮膚像素，建立一個新的膚色模型，最後再將它整合到初步訓練的膚色模型，以檢測出所有的皮膚像素。這個方法的概念是利用影像本身的膚色模型去調整初步訓練膚色模型，使得新的膚色模型符合目前影像的特性。我們將和 Jones 等人的實驗結果作比較，以證明新方法的效果。

2. 研究方法

本研究方法可分為兩個階段：訓練階段和皮膚檢測階段。圖一為研究方法之流程圖。
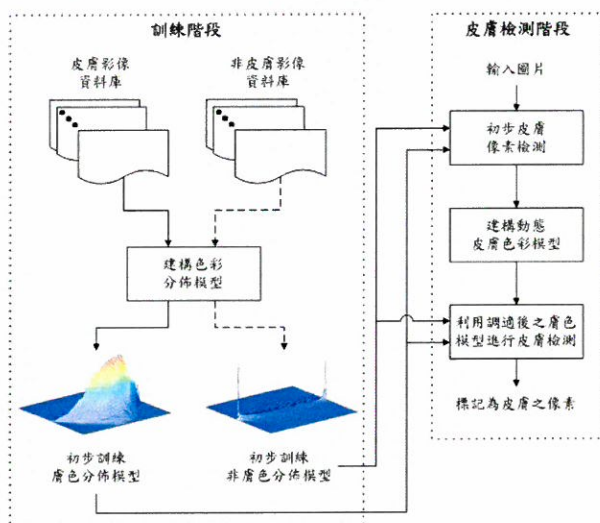
圖一 研究方法之流程圖

在訓練階段，我們從大量的皮膚和非皮膚之影像資料中，利用統計方法分別建立皮膚色彩分佈模型和非皮膚色彩分佈模型。在皮膚檢測階段再使用所建立之皮膚色彩分佈模型和非皮膚色彩分佈模型來做分析。

2.1 訓練階段

我們分別掃描皮膚影像資料庫中的影像和非皮膚影像資料庫中的影像，以記錄影像中之皮膚和非皮膚像素的色彩所出現的次數，再將最後的結果除以總次數，以了解該色彩屬於皮膚和非皮膚之概似值(likelihood)。假設在皮膚的影像資料庫中，共有 m_1 個屬於皮膚的像素，在 RGB 三維色彩空間之某個座標上的顏色，總共出現的次數為 n_1，則該顏色可能為皮膚的概似值為 n_1/m_1。假設在非皮膚之影像資料庫中，共有 m_2 個不是皮膚的像素，在 RGB 三維色彩空間之某個座標上的顏色，總共出現的次數為 n_2，則該顏色不是皮膚的概似值為 n_2/m_2，最後得到一個 RGB 皮膚色彩分佈模型和一個 RGB 非皮膚色彩分佈模型。這兩個模型的立體透視圖如圖一中所示。在後面的討論中我們也將看到其二維平面的投影圖。

2.2 皮膚檢測階段

皮膚檢測階段可以細分成三個步驟：*1.*初步皮膚像素檢測；*2.*建立動態皮膚色彩模型；*3.*使用調適後的膚色模型進行皮膚檢測。

2.2.1 初步皮膚像素檢測

此步驟之目的是要從影像中收集一些皮膚樣本，來預測影像中皮膚色彩的分佈模型。為了要達成這個目的，我們要知道較有可能為皮膚的是哪些顏色的像素，我們可以利用在訓練階段中產生之皮膚色彩分佈模型及非皮膚色彩分佈模型，來找出最有可能是皮膚的像素。

皮膚色彩分佈模型和非皮膚色彩分佈模型可以分別視為膚色和非膚色類別的概似函數。因此，針對一個像素 p，我們在這兩個分佈模型中，根據 p 的顏色，找出其皮膚概似值 L_{skin} 和非皮膚概似值 $L_{non-skin}$，所以，概似比 r 的計算公式即為

$$r = \begin{cases} \dfrac{L_{skin}}{L_{non-skin}}, & L_{non-skin} \neq 0 \\[2mm] 0, & L_{non-skin} = 0, L_{skin} = 0 \\[2mm] \infty, & L_{non-skin} = 0, L_{skin} \neq 0 \end{cases} \tag{1}$$

如果計算出之概似比 r 越大，像素 p 則越有可能為皮膚。對於每一個影像，我們可以利用以下函式計算出所有像素的概似比之累計分佈圖 h

$$h(i) = \left| \left\{ p \mid r_p \geq i \right\} \right|, 0 \leq i \leq max, i \in \mathbb{R} \tag{2}$$

h(i) 是表示影像中，所有概似比 r_p 大於或等於 i 的像素個數（在我們的實作中 i 的精確度為 1/100），r_p 是像素 p 的概似比，*max* 為我們計算 r_p 大於或等於 i 時所設定之最大值。將所計算出之累計分佈圖 *h(i)* 除以 *h(0)*（*h(0)* 為像素的總數量），即可製作成正規化累計分佈圖 *h*。假設 *h(8)/ h(0)=0.5*，即表示該影像中有 50% 的像素，其概似比 r 大於或等於 8。

圖二(c)及圖二(d)分別為圖二(a)與圖二(b)所計算出來的正規化累計分佈圖（一張有包含皮膚，另一張則沒有包含皮膚）。當 r_p 的數值越接近 *max*，表示像素 p 越可能為皮

膚。因此，如果要挑選最佳皮膚樣本的像素，我們可以藉助上述之正規化累計分佈圖。假設要挑選之皮膚像素的比率為 f, $0 \leq f \leq 1$，藉由查看累計分佈圖 h，得到 f所對應的概似比為 k，則我們應該挑選 $r_p \geq k$ 的像素當作皮膚的樣本。

(a)

(b)

(c)

(d)
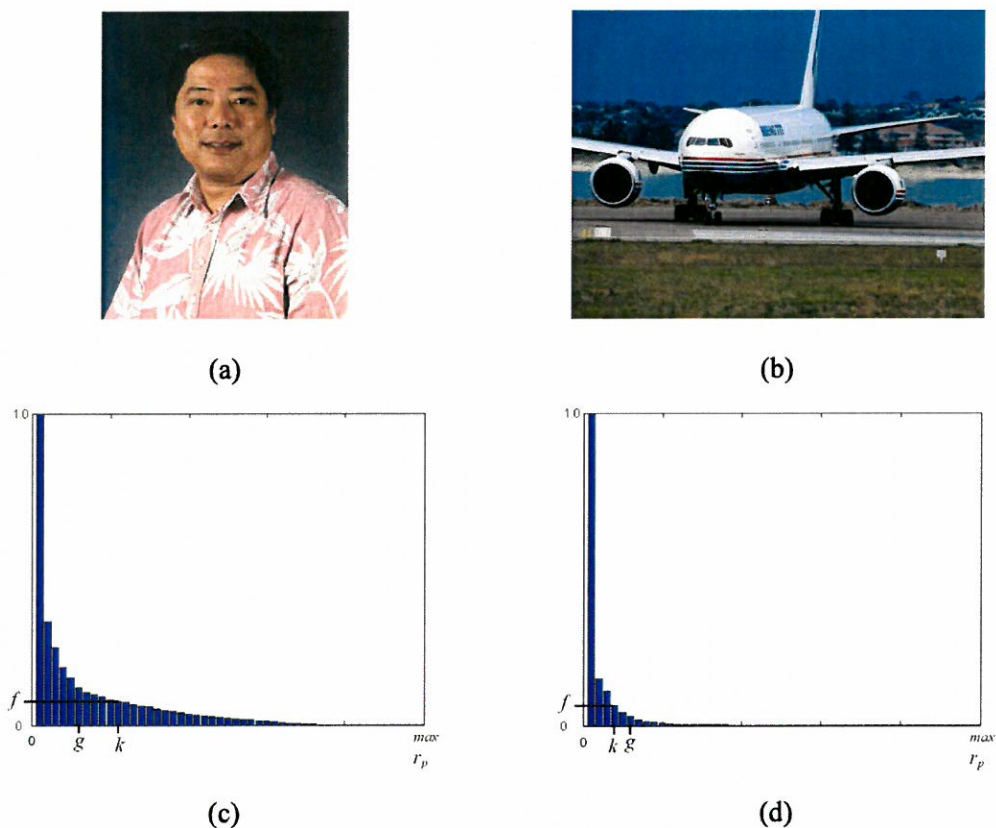
圖二　(a)包含皮膚的影像；(b)沒有包含皮膚的影像；(c)圖(a)的概似比正規化累積分佈圖（在這個例子裡 $k \geq g$）；(d)圖(b)的概似比正規化累積分佈圖（在這個例子裡 $k \leq g$）

　　然而，有些沒有包含皮膚的影像（如圖二(b)所示），像素的 r_p 值有時候會相對較小，這也就表示在這個影像中並沒有良好的皮膚樣本。為了要處理這種情況，我們在初步皮膚像素檢測的步驟中，增加一個臨界值 g（此臨界值為取樣時的最低值），使其成為如下的規則：

　　　　　假設我們要從影像中挑選一部分的皮膚像素（假設比率為 f）。藉由查看
累計分佈圖 h，找出 f 對應到 r_p 的 k 值，假如 $k \geq g$ 時，選擇 $r_p \geq k$ 的所有像
素；否則選擇 $r_p \geq g$ 的像素。

　　　　這個步驟的目的是根據整體的統計資料來挑選出最有可能是皮膚的像素。然而，我
們需要考量的問題是應該選擇多少的像素來當成皮膚樣本。選擇較多的像素可以幫助我
們對皮膚色彩分佈有較正確的估計，但在另一方面，非皮膚的像素也可能會有更多包含
在裡面；如果選擇較少的像素，雖然可以減少挑選到非皮膚的像素的機率，但是對於皮
膚色彩分佈之實際情況，卻可能無法正確的評估，這是一個兩難的問題，所以我們利用
參數 f 與 g 來控制選擇像素的比例，並透過適當的實驗來設定參數 f 與 g，我們將在第 3
節中探討相關之細節。
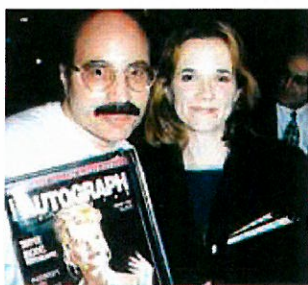
(a)
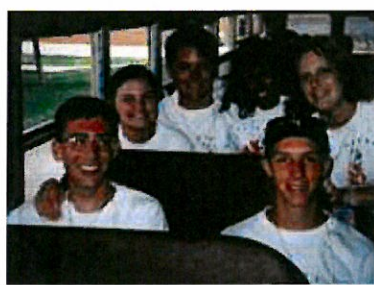
(b)

(c)
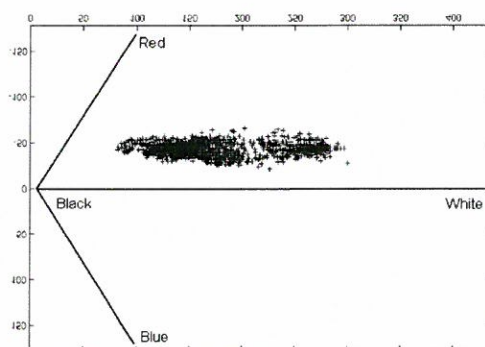
(d)

圖三　(a)曝光條件良好的膚色；(b)曝光條件不良的膚色；(c)從圖三(a)所收集的皮膚像素；(d)從
　　　圖三(b)所收集的皮膚像素

2.2.2. 動態皮膚色彩模型

根據所收集的皮膚像素，我們可以得知影像中皮膚色彩在 RGB 三維色彩空間中的分佈情況。但是由於這些皮膚樣本是根據每個像素的皮膚概似比 r 來篩選（亦即只挑選 r 較大的那些像素），而不是一個完全隨機的挑選過程，因此所得到之皮膚色彩分佈，可能不完全等於實際上在影像中之皮膚色彩分佈。儘管如此，這些收集到的皮膚像素的色彩分佈還是可以提供有用的線索，讓我們了解膚色存在的範圍。圖三顯示藉由兩個皮膚影像中收集的皮膚像素，所得到之皮膚樣本分佈圖，此分佈圖是將 RGB 三維空間依照 green-magenta 軸所做的投影結果。圖三(a)的皮膚影像為曝光條件良好時的膚色，如圖三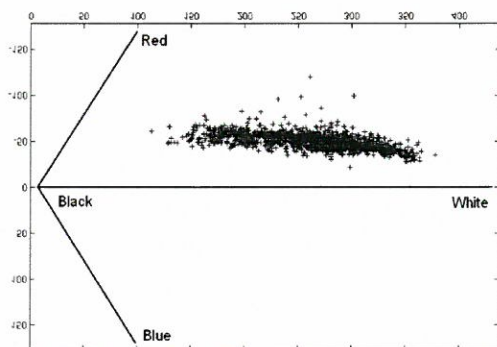(c)所顯示，在分佈圖中收集的皮膚像素群集偏向右邊。相較之下，圖三(b)為曝光條件不良時的膚色，如圖三(d)所顯示，在分佈圖中所收集的皮膚像素群集較偏左邊。藉由這個資訊，我們能夠適當地調整皮膚色彩模型，以配合影像中之皮膚分佈特性，藉此改善皮膚檢測之準確性。

要從所收集的資料樣本中，估計原始資料的分佈模型。最常使用的是EM演算法(Expectation Maximization algorithm)。它藉由混合幾個高斯機率密度函數來估計資料分佈的模型。EM演算法分為兩個步驟，計算期望值的步驟，稱為期望值步驟(Expectation Step，E-step)，以及求取最大值的步驟，稱為最大化步驟(Maximization Step，M-step)，藉由反覆執行上述兩個步驟，以得到最吻合資料樣本的資料分佈模型。

它也使用於一些採用高斯混合模型代表皮膚和非皮膚色彩模型的皮膚檢測系統[1, 2, 4, 16, 19, 21]。由於 EM 演算法需要大量的計算，所以它大部份使用在離線的訓練階段。然而，在我們的方法中，由於從挑選皮膚像素樣本到建構膚色模型的步驟都必須即時完成，所以我們需要一個執行速度更快的演算法。此外，我們所使用之高斯機率密度函數的數目，可能會根據不同的影像而有所不同，所以演算法本身必須能夠自動決定需要多少數目之高斯函數。

為了符合需求，我們使用一個兩階段的群集演算法(two-stage algorithm)，第一階段使用最大最小距離演算法(maximin distance check)決定皮膚像素群集中心的個數（也就是機率密度函數的個數）；第二階段使用 K-means 群集演算法來實際完成群集的工作。結合最大最小距離演算法和 K-means 群集演算法之後，我們所提出之演算法如下所示：

定義

　　(a) p_i, i = 1, 2, …, 為皮膚像素；

　　(b) z_j, j = 1, 2, …, 為群集中心；

　　(c) ColorDist(p_i, z_j)是 p_i 和 z_j 在色彩空間中之距離；

　　(d) T是一個用來檢驗色彩距離之臨界值。

群集演算法

　　階段1

　　　1. 設定 $z_1 = p_1$。

　　　2. 對於所有的 p_i 計算 $D_i = \min_j\{\text{ColorDist}(p_i,\ z_j)\}$，$z_j$ 為群集中心，$1 \le j \le n$。

　　　3. 假設 $D_k = \max_i\{D_i\}$，如果 $D_k > T$ 成立，那麼設定 $z_{n+1} = p_k$，並且回到步驟2；如果 $D_k > T$ 不成立，就結束階段1。

　　階段2

　　　1. 使用最小距離分類法將皮膚像素進行分類，假設所有的 k ≠ j，如果 ColorDist(p_i, z_j) < ColorDist(p_i, z_k)，就將 p_i 指派給群集 j。

　　　2. 重新計算每個群集中心 z_i，如果每個 z_i 的值在連續兩個回合的運算期間沒有變更或其改變量小於我們所預先設定的臨界值，群集工作便完成，否則就回到步驟1，繼續下一個回合的演算。

　　參數 T 的用途是為了控制群集的個數，較大的 T 值將導致較少的群集，而較小的 T 值將導致更多的群集。目前我們將系統中的 T 值設定為 80。圖四(a)和圖四(b)為圖三(c)和圖三(d)的皮膚像素套用上述群集演算法之結果。

　　我們根據所挑選出的皮膚像素，建立一個由多個高斯機率函數所組成的動態膚色模型。先利用上述之群集演算法將皮膚像素依照顏色分成幾個群組，然後將每一個群組視為獨立的高斯分佈，並計算每個群集的平均向量和共變異數矩陣，最後再利用下列公式，計算整體皮膚像素之分佈模型：

$$P_{skin}(p) = \sum_{i=1}^{N} w_i \frac{1}{(2\pi)^{3/2}|\Sigma_i|^{1/2}} \exp(-\frac{(p-\mu_i)^T \Sigma_i^{-1}(p-\mu_i)}{2}) \tag{3}$$

其中 N 是群集的數目，μ_i 和 Σ_i 是群集 i 之平均向量和共變異數矩陣，w_i 代表不同像素群集的權重，可以根據下列之公式計算：

$$w_i = \frac{群集i中皮膚像素的個數}{全部皮膚像素的個數} \tag{4}$$

圖四(c)和圖四(d)顯示由圖四(a)和四(b)的群集中分別計算出之皮膚色彩模型。

(a)   (b)

(c)   (d)
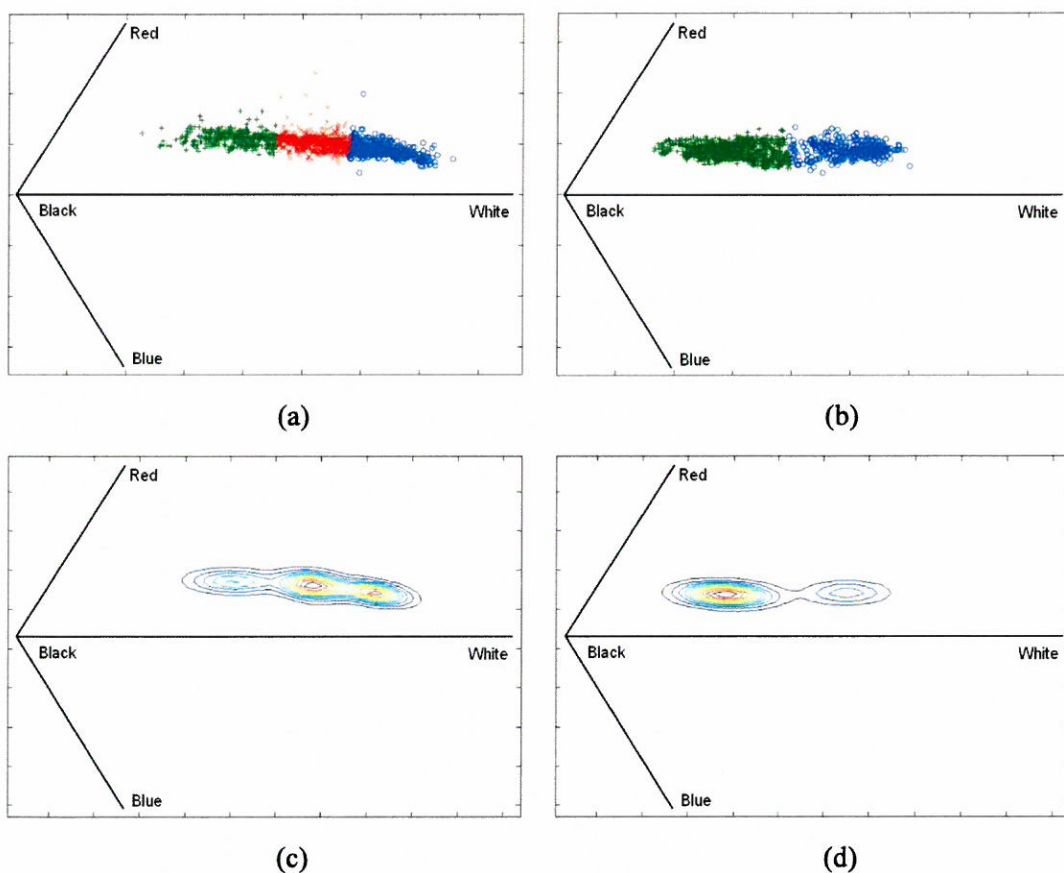
圖四　運用群集演算法產生之結果：(a)圖三(c)之群集圖；(b)圖三(d)之群集圖；(c)對應到圖四(a)的膚色模型；(d)對應到圖四(b)的膚色模型

(a)

(b)

(c)
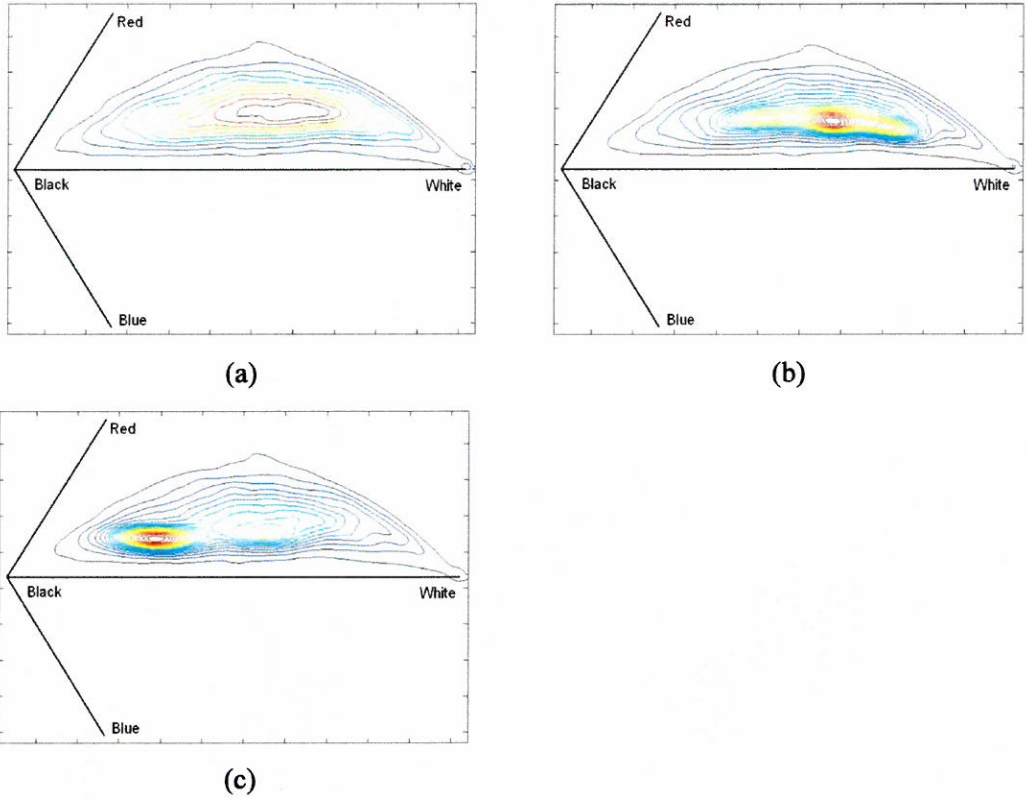
圖五　(a)在訓練階段中產生之膚色模型；(b)結合圖 4(c) 之膚色模型所得到調適後的膚色模型；
　　　(c)結合圖 4(d)之膚色模型所得到調適後的膚色模型

2.2.3. 使用調適後的膚色模型進行皮膚檢測

　　上述的影像膚色模型，讓我們可以了解該影像中膚色在色彩空間中存在的區域。然
而，就像之前所敘述的，影像膚色模型可能不會與影像中真正的皮膚色彩分佈完全相
同，但是我們可以用它來調整在訓練階段中產生之膚色模型，使其較符合影像中之皮膚
分佈特性。要做到這一點，我們可以將影像的膚色模型和在訓練階段中產生之膚色模
型，依照下列公式結合成調適後的膚色模型，並利用它來完成皮膚檢測之工作：

$$P_{adapted}(p) = u_1 P_{pre-trained}(p) + u_2 P_{skin}(p) \tag{5}$$

加權因子 u_1 和 u_2，必須滿足以下條件：

$$u_1 + u_2 = 1 \tag{6}$$

$$0 \leq u_1 \leq 1 \tag{7}$$

$$0 \leq u_2 \leq 1 \tag{8}$$

我們將在第 3 節中討論如何決定最佳的 u_1 和 u_2。圖五表示經過調適後的皮膚色彩模型。從圖中可以看出，設定加權因子 u_1=0.8 和 u_2=0.2 之後，將訓練階段中產生之膚色模型結合圖四(c)和圖四(d)之膚色模型，可發現調適後的皮膚色彩模型較符合影像中的膚色分佈區域，圖五(b)為曝光條件良好之影像的皮膚色彩模型和圖五(c)為曝光條件不良之影像的皮膚色彩模型。

根據調適後的膚色模型可以得到像素 p 的皮膚概似值 $L_{adapted}$；同時，查詢在訓練階段中產生的非膚色模型，即可找到像素 p 的非皮膚概似值 $L_{non\text{-}skin}$。然後根據貝式分類法則，將概似值 $L_{adapted}$ 除以 $L_{non\text{-}skin}$ 所得到的概似比，即可用來決定像素 p 是否為皮膚。

$$\frac{L_{adapted}}{L_{non\text{-}skin}} \geq \theta \tag{9}$$

θ 是一個預先設定好的臨界值。較大的 θ 值會使得檢測到之皮膚像素比較少，但是，在此同時我們可以降低錯誤之發生率（也就是非皮膚像素被誤認為是皮膚像素的機率）。相反的，較小的 θ 值，可以檢測出更多的皮膚像素，但是誤判率可能會提高。這種現象我們可以使用 ROC 曲線圖來描述，細節部份將在第 3 節中討論。

3.實驗結果

我們的方法並非只適用於某一個特定的色彩空間。雖然皮膚檢測技術使用在不同的色彩空間時，對於準確性和執行速度可能會有少許的差異[4, 18]。但是為了比較我們的方法與 Jones 等人所提出的方法的效果，我們使用和 Jones 等人相同的 RGB 色彩空間來測試膚色檢測的效能，我們的實驗資料庫亦與 Jones 等人相同，總共包含 8965 個非皮膚影像和 4675 個皮膚影像。

每一個皮膚影像都有一個外部檔案標示它的皮膚區域。我們隨機選擇一半的非皮膚影像及一半的皮膚影像，組成一個訓練資料庫，其餘的影像組成一個測試資料庫。利用訓練資料庫來建立「初步訓練的膚色模型」和「初步訓練的非膚色模型」。在圖五(a)中我們已經展示過「初步訓練的膚色模型」，圖六則為「初步訓練的非膚色模型」。

　　如同在第 2 節所敘述，我們的方法包含了三個重要的參數 f, g, 和 u_1 （u_2是與 u_1互有關聯的參數：$u_1 + u_2 = 1$）。爲了找出這些參數適當的設定值，我們先根據經驗爲每個參數決定兩個數值：f = (0.05, 0.1)、g = (1.2, 2.0)和 u_1 = (0.6, 0.8)，再利用它們所有可能的組合（即八個集合）來進行測試。圖七顯示八個不同參數組合所得到的 ROC 曲線與 Jones 等人的方法所得到的 ROC 曲線。

　　我們可以看出，當參數設定爲(f, g, u_1) = (0.1, 1.2, 0.8)時，可以達到最佳的準確性。與 Jones 等人的方法相比，我們的方法在低誤判率(false detection rates ,FDRs)範圍內，對於皮膚召回率(skin recall rate,SRR)有顯著的改善。舉例來說，在(0.1, 1.2, 0.8)的 ROC 曲線上，當 FDR = 0.05 時，SRR 爲 0.74。Jones 等人的方法在相同的 FDR 時，SRR 爲 0.69。然而，在較高的 FDRs 範圍內，我們的方法逐漸接近 Jones 等人的方法。
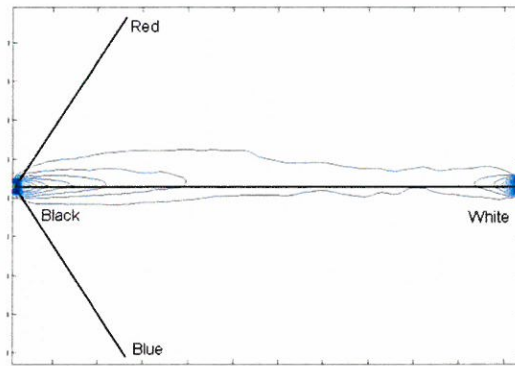
圖六　利用訓練資料庫所得到的「初步訓練的非膚色模型」
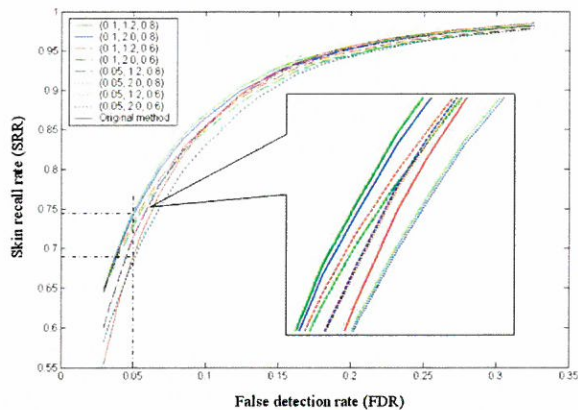
圖七　我們的方法（八個不同的參數設定）與 Jones 等人的方法(Original method)之 ROC 曲線圖
　　　（測試影像數目爲 4482 張非皮膚影像和 2337 張皮膚影像，測試環境爲 PC-P4 2.6G/WindowsXP 和以 C++實作的程式碼）

　　圖八是使用我們的方法和 Jones 等人的方法所得到的結果，在使用相同的臨界值 θ (θ = 2.5)的條件下，圖八(a)顯示了 Jones 等人的方法所檢測到的皮膚像素（標記為黑色），圖八(b)為我們的方法之結果（來源影像為圖三(a)）。在原來的影像中，女人臉部上的皮膚區域因為曝光過度，所以與正常的皮膚顏色相較起來變得太過於明亮。原來的方法在這種情況之下，會有較低的識別率（如圖八(a)所示）。相較之下，我們所提出的方法可以適應這些變化並獲得更好的識別結果（如圖八(b)所示）。圖八(c)和圖八(d)為圖三(b)的處理結果，在原來的影像中，皮膚區域發生曝光不足的情況(太暗)。從圖中可以看出，我們的方法也能適應曝光不足的情況，並產生一個比原來方法更好的結果。圖九另外提供三張影像和其處理結果以供比較。第一欄是原始影像，第二欄是我們方法的處理結果，第三欄是 Jones 等人的方法所得到的結果。第一張影像中的皮膚偏向暗紅色，實驗結果顯示我們的方法比 Jones 等人的方法能夠偵測出更多的膚色，另外由於頭髮的顏色和膚色類似，因此被認定是皮膚的比例也有增加。第二張影像是沒有皮膚的影像，但是其中含有類似膚色的景物（土地和建築物的牆）。在我們的結果中，土地被誤判成皮膚的數量比較高，因為它在膚色取樣的過程中佔了比較大的比例，但是建築物的牆被誤判成皮膚的部分反而減少了一些。第三張也是不含皮膚的影像，而且其中也沒有類似膚色的景物，在這個例子中，我們的方法和 Jones 等人的方法的處理結果差異不大。

　　如果我們仔細觀察不同的 f、g 和 u_l 的值對於 ROC 曲線的影響，我們可以發現 f = 0.1 優於 f = 0.05、g = 1.2 優於 g = 2.0 和 u_l = 0.8 優於 u_l = 0.6。這表示當我們使用較大的 f 值、較小的 g 值和較大的 u_l 值時，可能可以獲得更好的實驗結果。因此我們嘗試另外三個設定，將(f, g, u_l)設定為(0.2, 1.0, 0.85), (0.25, 0.9, 0.9) 和 (0.3, 0.8, 0.95)。圖十為實驗結果，其中包含圖七的最佳參數組合（即(0.1, 1.2, 0.8)）以方便比較。我們在圖中可以看出新的設定值的準確度比先前設定的更好。根據對實驗結果的觀察，我們推斷當(f, g, u_l) = (0.25, 0.9, 0.9)時，我們的方法可以得到最佳的識別率。

(a)　　　　　　　　　　　　　　　　　　(b)

(d)　　　　　　　　　　　　　　　　　　(c)
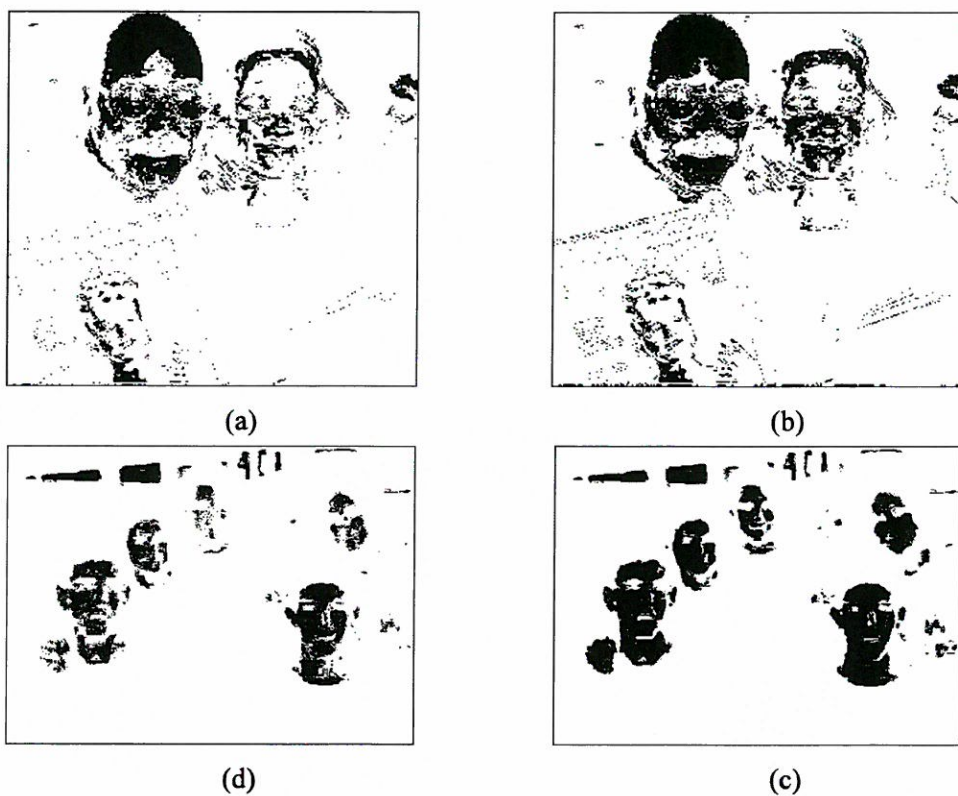
圖八　我們的方法與 Jones 等人的方法之比較：(a) Jones 等人的方法所檢測到的皮膚像素（來源
　　　影像為圖三(a)）；(b)我們的方法之結果；(c) Jones 等人的方法所檢測到的皮膚像素（來源
　　　影像為圖三(b)）；(d)我們的方法之結果

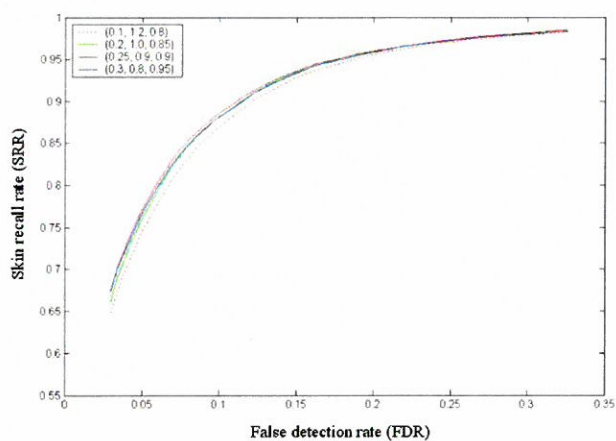圖九　含有皮膚的影像和不含皮膚的影像的處理結果：第一欄是原始影像，第二欄是我們方法的處理結果，第三欄是 Jones 等人的方法所得到的結果

圖十　(f, g, u_l) = (0.1, 1.2, 0.8), (0.2, 1.0, 0.85), (0.25, 0.9, 0.9) 和 (0.3, 0.8, 0.95) 之 ROC 曲線圖（測試影像數目為 4482 張非皮膚影像和 2337 張皮膚影像，測試環境為 PC-P4 2.6G/WindowsXP 和以 C++實作的程式碼）

4.結　論

　　本篇論文提出一個在影像中檢測皮膚的新方法。原來的皮膚檢測技術會受到不同曝光條件的影響，使得皮膚檢測的準確性降低。為了改善這樣的缺點，在一些先前的研究中提出了可調適的膚色模型以追蹤影片中的膚色區域。這些可調適的膚色模型是利用兩個連續影格中的顏色相關性來動態調整膚色模型。但是對於獨立的影像檔案，因為它們之間沒有相關性，所以需要一個新的方法。我們利用一個動態皮膚色彩模型來調整訓練階段所產生的皮膚色彩模型，使得最後的皮膚模型能夠適用於正在處理中的影像。

　　動態皮膚色彩模型是根據影像中所收集到的皮膚像素樣本產生。此法的效果會受到皮膚像素樣本的數目和兩個膚色模型的加權因子所影響。我們將使用不同參數所得到的實驗結果和原來沒有使用動態調適技術的實驗結果加以比較。另外再藉由觀察參數對於實驗結果的影響，以推論出最佳的參數設定並完成測試。實驗結果顯示在低誤判率的條件下，我們的方法的皮膚檢測率明顯高於原來的方法。而在高誤判率的條件下，我們的皮膚檢測率則和原來的方法相近。

5.參考文獻

[1]　M. J. Jones, J. M. Rehg, Statistical color models with application to skin detection, Int. J. of Computer Vision, 46 (1) pp. 81-96 (2002).

[2]　J. Yang, W. Lu, A. Waibel, Skin-color modeling and adaptation, Proc. ACCV98, pp. 687-694 (1998).

[3]　M. Storring, H. J. Andersen, E. Granum, Physics-based modelling of human skin colour under mixed illuminants, Robotics and Autonomous Systems, 35 (3) pp. 131-142 (2001).

[4]　P. Kakumanu, S. Makrogiannis, N. Bourbakis, A survey of skin-color modeling and detection methods, Pattern Recognition, 40 (3) pp. 1106-1122 (2007).

[5]　D. Chai, K. N. Ngan, Face segmentation using skin-color map in videophone applications, IEEE Trans. Circuits and Systems for Video Technology, 9 (4) pp. 551-564 (1999).

[6]　Y. Wang, B. Yuan, A novel approach for human face detection from color images under complex background, Pattern Recognition, 34 (10) pp. 1983-1992 (2001).

[7]　Y. Dai, Y. Nakano, Face-texture model based on SGLD and its application in face detection in a color scene, Pattern Recognition, 29 (6) pp. 1007-1017 (1996).

[8]   M. J. Seow, D. Valaparla, V. K. Asari, Neural network based skin color model for face detection, Proc. 32nd Workshop on Applied Imagery Pattern Recognition, pp. 141-145 (2003).

[9]   S. L. Phung, D. Chai, A. Bouzerdoum, A universal and robust human skin color model using neural networks, Proc. IJCNN01, pp. 2844-2849 (2001).

[10] C. Chen and S.-P. Chiang, Detection of human faces in colour images, IEE Proc. Vision, Image and Signal Processing, 144 (6) pp. 384-388 (1997).

[11] H. Zheng, M. Daoudi, B. Jedynak, Blocking adult images based on statistical skin detection, Electronic Letters on Computer Vision and Image Analysis, 4 (2) pp. 1-14 (2004).

[12] D. Chai, A. Bouzerdoum, A Bayesian approach to skin color classification in YCbCr color space, Proc. IEEE TENCON00, vol. 2, pp. 421-424 (2000).

[13] T.-W. Yoo, I.-S. Oh, A fast algorithm for tracking human faces based on chromatic histograms, Pattern Recognition Lett., 20 (10) pp. 967-978 (1999).

[14] S. Srisuk, W. Kurutach, A new robust face detection in color images, Proc. IEEE AFGR02, pp. 306-311 (2002).

[15] P. Kuchi, P. Gabbur, P. S. Bhat, S. David, Human face detection and tracking using skin color modeling and connected component operators, IETE J. Research, 38 pp. 289-293 (2002).

[16] M.-H. Yang N. Ahuja, Gaussian mixture model for human skin color and its applications in image and video databases, Proc. SPIE Conf. Storage and Retrieval for Image and Video Databases, pp. 458-466 (1999).

[17] H. Greenspan, J. Goldberger, I. Eshet, Mixture model for face-color modeling and segmentation, Pattern Recognition Letters, 22 (14) pp.1525-1536 (2001).

[18] V Vezhnevets, V Sazonov, A Andreeva, A survey on pixel-based skin color detection techniques, Proc. Graphicon, pp. 85-92 (2003).

[19] S. J. Mckenna, S. Gong, Y. Raja, Modelling facial colour and identity with Gaussian mixtures, Pattern Recognition, 31 (12) pp. 1883-1892 (1998).

[20] L. Sigal, S. Sclaroff, V. Athitsos, Skin color-based video segmentation under time-varying illumination, IEEE Trans. PAMI, 26 (7) pp. 862-877 (2004).

[21] N. Oliver, A. P. Pentland, F. Berard, LAFTER: lips and face real time tracker, Proc. Computer Vision and Pattern Recognition, pp. 123-129 (1997).

[22] L. M. Bergasa, M. Mazo, A. Gardel, M. A. Sotelo, L. Boquete, Unsupervised and adaptive Gaussian skin-color model, Image and Vision Computing, 18 (12) pp. 987-1003 (2000).

[23] Y. Chahir, A. Elmoataz, Skin-color detection using fuzzy clustering, Proc. ISCCSP, (2006).

[24] J.-S. Lee, Y.-M. Kuo, P.-C. Chung, E.-L. Chen, Naked image detection based on adaptive and extensible skin color model, Pattern Recognition, 40 (8) pp. 2261-2270 (2007).

Skin segmentation system automatically adapted to image illumination conditions

Hung-Ming Sun   Yi-Ting Wang

Department of Information Management, Kainan University

No. 1 Kainan Road, Luchu, Taoyuan County, 33857, Taiwan, R.O.C.

Abstract

Presentation of skin color in images can be influenced by illumination conditions and thus makes the result of skin segmentation degrade. To solve this problem, a self-adapting method is proposed. It collects some representative skin samples from the input image and uses them to tune a trained skin color model. The adapted skin color model can match better the skin distribution in the input image and increases the skin segmentation accuracy. After testing over 13000 images (including training and test images), it shows that the new method performs better than the original method.

Reducing Crosstalk for Improving Electrostatic Discharge Immunity Using Separated Common Plane in Printed Circuit Board Design

*Yuang-Shung Lee,[1] Cheng-Hsiung Chiang[2]

Abstract

This paper investigates how to improve electrostatic discharge (ESD) immunity in a printed circuit board (PCB) to increase the reliability of electronic products. Firstly, the current waveform standard for the electrostatic discharge generator of IEC61000-4-2 is discussed. An equivalent ESD circuit is then established and its accuracy confirmed using mathematical equations and practical measurements. This equivalent circuit model is applied as the electrostatic discharge source to further analyze various PCB trace structures. In general, crosstalk is one of the main factors causing ESD problems. This study solves this problem by comparing the influences of crosstalk from different PCB trace structures in the time and frequency domains. The results show that the separated common plane has the following major advantages for PCB design: 1) lower crosstalk with excellent ESD immunity; 2) smaller PCB layout spacing requirements; and 3) eliminates the need for great engineering changes in the design. The simulation results are in good agreement with the measurement results.

Keywords : Printed-circuit board, Electrostatic discharge, Crosstalk, Microstripe

[1] Graduate Institute of Applied Science and Engineering, and Department of Electronic Engineering, Fu-Jen Catholic University 510 Chung-Cheng Rd., Hsin-Chuang, Taipei 24205, Taiwan Tel: +886-2-29053791 Fax: +886-2-29042638

[2] Advanced Technology Development Department MICRO-STAR INTERNAL CO., LTD, No.69, Li-De St, Jung-Ho City, Taipei Hsien 235, Taiwan 1) lee@ee.fju.edu.tw 2) williams@msi.com.tw

1. Introduction

In recent years, owing to tighter rise time and smaller geometry spacing, ESD problems have become an increasingly serious issue. Many theoretical analyses have tried to solve this problem [1-4]. However, these analyses had difficulty meeting the actual requirements, especially ESD problems caused by crosstalk. Conventionally, there are techniques for reducing PCB crosstalk. The first method involves maintaining impedance matching in the transmission lines (TL) to avoid reflection [2]. The second method reduces the TL length and drop signal rise time as much as possible [3]. Differential signal design is significantly helpful for decreasing crosstalk [4]. Attaching extra components, such as the transient voltage suppressor diode and varistor, on critical traces, to abate crosstalk is also one of the ESD countermeasures [5]. Using a particular number of ground vias or/and guard traces between adjacent lines was developed for crosstalk reduction [6,7]. Modifying the PCB substrate width to height ratio which is a vast change to the original product design has been presented to reduce crosstalk [8,9]. To expend greater spacing between the aggressor and victim lines as well as the 3W rule is another general solution. However, these methods all have some significant shortcomings. They either consume PCB layout space or increase the cost. In fact, some of them are hard to apply. This paper discusses increasing the PCB layout utility rate, while reducing crosstalk and improving ESD immunity simultaneously through modifying the location of the in common plane separation. This paper adopts the function "Transient" and "S parameter" of Agilent Advanced Design System (ADS) softward package which is a commercial simulation tool for PCB design and analysis [10], and for the actual measurement, digital storage oscilloscope (DSO) and vector network analyzer (VNA) are used to validate the results from simulation tool.

2. MODELS OF ESD GENERATOR

The ESD generator is used for evaluating the ability of equipment or systems related to satisfactory function in an ESD event. Most electronics products must implement ESD testing and meet the IEC61000-4-2 standard. During and after testing the product functions must remain consistent and operate normally as before testing [11]. That standard has provided a typical current ESD waveform with some important parameters in the contact mode, such as consistent rise time, first pulse current maximum amplitude, second peak current at 30ns, and

maximum value of the current at 60ns. As can be seen from Fig. 1, the current tolerances are separately specified for +/-10%, +/-30%, and +/-30%. The standard also insists that various ESD voltage levels must conform to corresponding current values. In practical applications, many ESD generators are made in accordance with the above-mentioned standards but obtain different results during product testing [12].
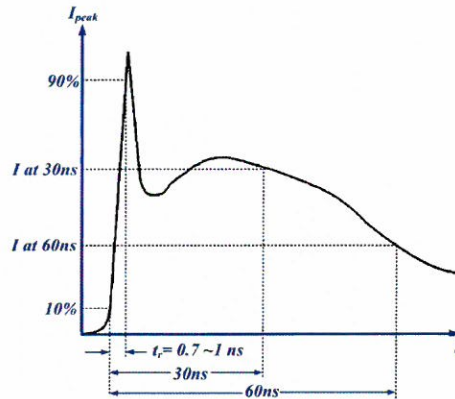
Figure 1.   ESD classification test current waveform in contact mode

The advantage of mathematical equations is that they are able to predict the discharge current and related fields based on the charging voltage and geometry. Hence a variety of mathematical equations have been presented to fit the IEC61000-4-2 ESD specifications [11]. The ESD current waveform is an impulse response and convolved with the nonlinear characteristics. A novel mathematical equation provides the polynomial pulse function with the continuity of the first derivative at time equal zero and time integrable [13]- [14]. The transient current cannot be changed instantly during the ESD discharge. In other words, the radiated field generated by ESD is related to the current and also to the current derivative. On the other hand, time integral-unable is not convenient for the ESD numerical calculations for the radiated fields otherwise the radiated field would not be efficiently calculated. The ESD charge and discharge can be predicted in the time-domain as:

$$i\left(t\right)= I_{0} \cdot \left[1-\exp\left(-\frac{t}{\tau 1}\right)\right]^{p} \cdot \exp\left(-\frac{t}{\tau 2}\right)$$
$$+ I_{1} \cdot \left[1-\exp\left(-\frac{t}{\tau 3}\right)\right]^{q} \cdot \exp\left(-\frac{t}{\tau 4}\right) \qquad (1)$$
$$+ I_{2} \cdot \left[1-\exp\left(-\frac{t}{\tau 5}\right)\right]^{r} \cdot \exp\left(-\frac{t}{\tau 6}\right)$$
$$+ I_{3} \cdot \left[1-\exp\left(-\frac{t}{\tau 7}\right)\right]^{s} \cdot \exp\left(-\frac{t}{\tau 8}\right)$$

where the exponential order p, q, r, and s are integral numbers and $\tau 1 \sim \tau 8$ time constants and $I_0 \sim I_3$ are also the current amplitude constants.

A simulated ESD generator lumped circuit is supposed to synthesize the typical standard ESD waveform through ADS transient analysis [15,16]. Refer to the model as displayed in Fig.2. C1=150pF and R1=330Ω are for fitting into a standard that simulates the charge and discharge in the human body mode (HBM). C2 and L1 are the impedance of the ESD generator grounding wire and these two components are for shaping the second pulse of the current waveform. R2 and C3 extracted from internal network are the parasitic resistor and capacitor for the ESD generator. Otherwise, different brands of ESD generators usually have considerable variation in these parameters. L2 is regarded as the inductance between the ESD generator and its electrodes. This equivalent component determines the amplitude only at the second pulse. Oscilloscope internal impedance consists of C4 and R3; providing a main path that allows the discharge current to return to ground. The simulated current probe is connected between the tip and ground. Practical measurement uses ESS-2000 of NOISEKEN, and its generator is TP-805R. The inner impedance of the digital storage oscilloscope was set to 50ohm and the discharge voltage was captured by it. The discharge current was obtained through dividing the obtained voltage by 50ohm and is presented in Fig.3. To avoid the high ESD voltage damaging the instrument, a 20dB attenuator was used to decay the ESD noise. The equivalent circuit comparison, mathematical equation, and practical measurement all used 6KV injected voltage in the contact mood as presented in Fig. 4. Consequently, the first equivalent circuit rise time can be produced repeatedly and approximates the reference IEC current waveform rise time. The transient spike between the first and second pulses at 30ns is caused by the grounding wire. Its

length may need to be as short as possible in order to reduce the transient spike. According to the IEC61000-4-2 standard, this spike is not described. Similarly, the mathematical equation also formulates this. In fact, the practical measurement results of all ESD generators exhibit the existence of this spike. Therefore, an equivalent circuit will duplicate the measured result in this paper, exposing the transient spike and second pulse. However, most ESD effects are related to the rise time and the peak current at first pulse. The actual result will not be influenced even if the current curve has a small difference at the second and last pulses.
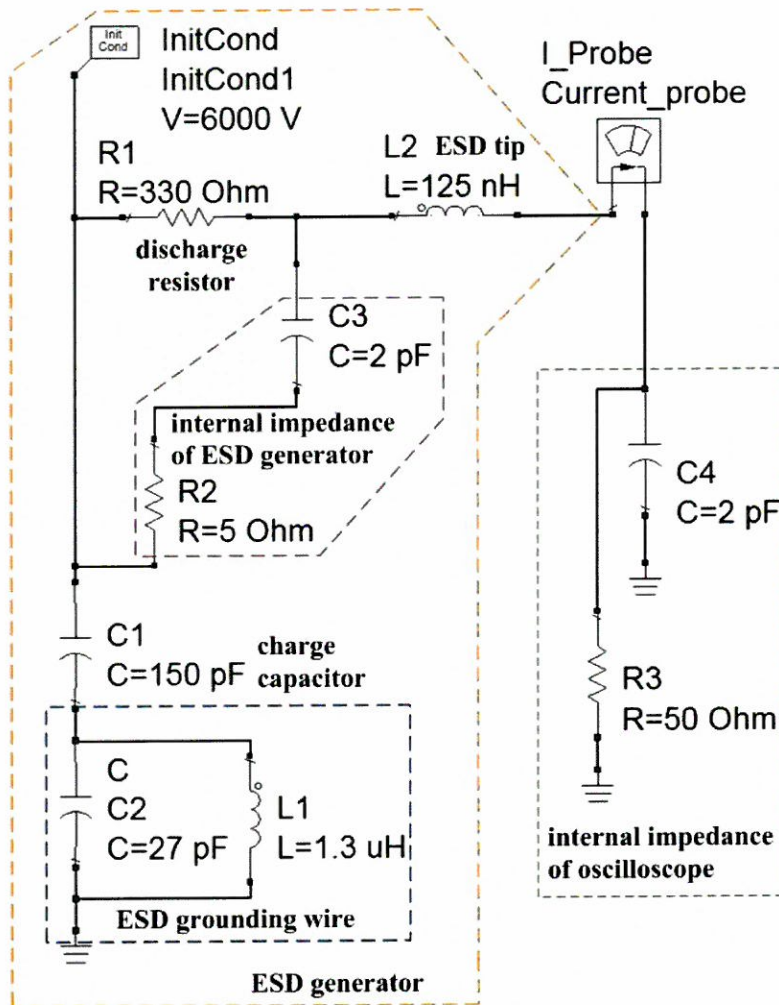

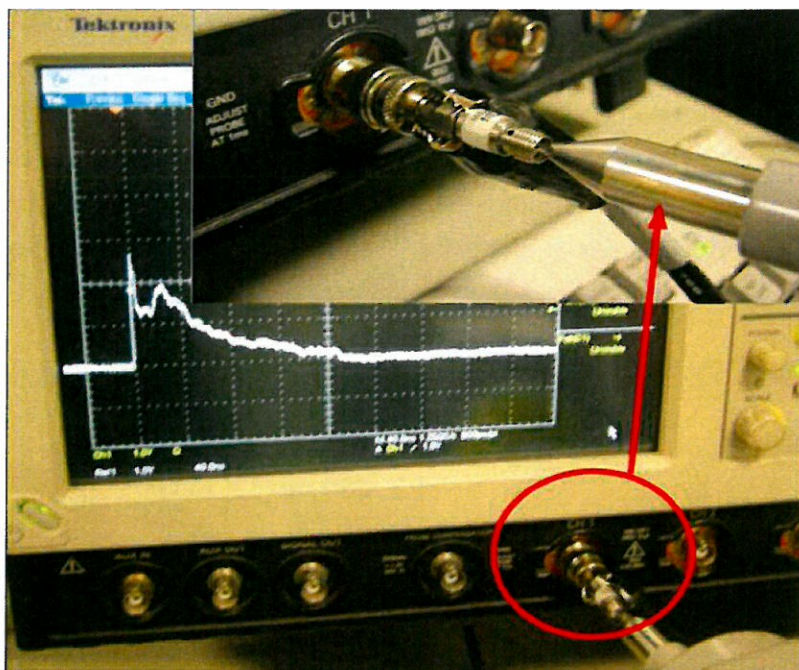Figure 2.   Equivalent circuit of ESD generator

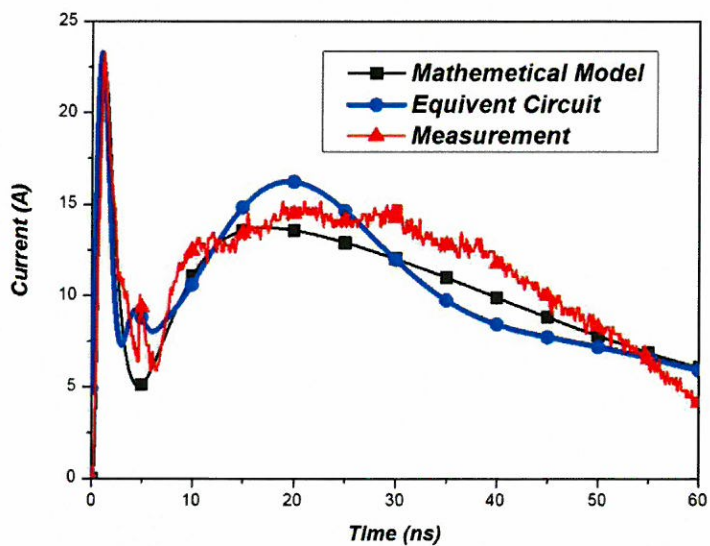Figure 3.   Practical measurement for ESD voltage waveform generator

Figure 4.   Comparison of current waveform for mathematical model, equivalent circuit, and measurement

3. COMMON PLANE SEPARATION

Most crosstalk reduction studies focus on the electromagnetic field coupling because a wider common plane provides a better return path. Hence, decreasing mutual inductances and mutual capacitances are a major method to reduce coupling noise. Unfortunately, that method usually depends on spacing between the adjacent trace. In general, the power plane and ground plane are common plane or the so-call image plane, used as a reference plane for high frequency return path of signal current. The return current always flows through the nearest power or/and ground plane, hence the signal current distribution should be the same as the common plane distribution current. In this paper, the proposed strategy is to decrease the current distribution field to the surrounding traces in their common plane and block the current distribution overlap from each other. The separated common plane incorrectly may make the PCB become a slot antenna and subsequently convert the crosstalk into a more serious problem. Therefore, this method focuses on the signal current density $I(x)$ calculation proposed in [17] and total signal current distribution can be expressed as:

$$I(x) = \frac{I_0}{\pi H} \cdot \frac{1}{1 + (x/H)^2} \tag{2}$$

$$I_D = \int_{-3H}^{3H} I(x)\,dx = \int_{-3H}^{3H} \frac{I_0}{\pi H} \cdot \frac{1}{1 + (x/H)^2}\,dx = \frac{2I_0}{\pi} \cdot \tan^{-1}(3) \approx 0.795\,I_0 \tag{3}$$

where I_0, H and X are the steady state current, dielectric thickness and distance respectively.

Assume that W is the width of PCB trace. The return current distribute to adjacent traces with double width signal trace spacing on the common plane is shown in Fig. 5(a). From equation (3), about eighty percent of the return current on the reference plane is concentrated in the 3H area aside the trace centre. Thus, if the distance between the two microstrip transmission line (MTL) couplings becomes much larger than 3H, the common plane coupling will be significantly reduced, as shown in Fig. 5(c). Similarly, based on the distribution of return current concept, if there is a moat on the reference plane, as shown in Fig. 5(b), the common plane coupling can also be decreased since the overlapped current is almost zero; Comparing Fig. 5(b) with Fig. 5(c), although the common current of coupling traces are both very small, the distance

between the traces in Fig. 5(b) is less than that in Fig. 5(c). Hence, following this rule of thumb, a plane moat is helpful for ESD coupling reduction without additional space requirement.
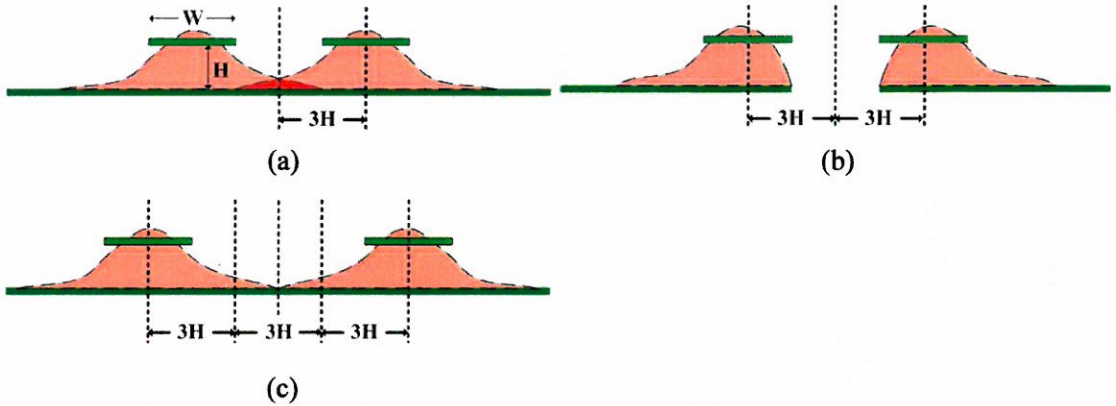

(a)   (b)

(c)

Figure 5.   Return current distributed for (a) adjacent traces with 2W spacing on the common plane (b) adjacent traces with 2W spacing on a separated common plane (c) adjacent traces with 3W spacing on common plane

4. SIMULATION AND EXPERIMENTIAL RESULTS

4.1 Simulation

To investigate the determining variables for the separated common plane design, a parametric study on the effects of various geometrical features of separation was conducted here. The Per-unit-length parameters are needed to determine the particular line cross-sectional configuration to solve the multi-conductor transmission line equations. A model is extracted using the numerical simulation tool ADS in this work, as show in Fig. 6(a). For the case whose spacing is double width between adjacent traces and two separated common inhomogeneous media planes. The proposed simulation structure is composed of ADS mircostrip line and mircostrip gap models, which include two kinds of component materials, effective FR4 dielectric substrate constant is set to 4.47 and 1 for air. The simulated ESD generator injects +6kV into evaluated PCB structure directly, which is 2W spacing between adjacent traces. The PCB structure simulation is combined with 20 segment models from the above evaluated equivalent circuit shown Fig. 6(b). R1, R2, R3, and R4 50 ohm resistors are for impedance matching. Simulated ESD generator force into evaluated PCB equivalent circuit and far-end crosstalk (FEXT) voltage can be obtained. In addition, the 3W rule with lower crosstalk than 2W spacing between adjacent traces is proven via this simulation. The proposed structure,

separated common plan of 2W spacing between adjacent traces, acquires the same performance as the 3W rule, also displayed clearly in Fig. 7 (a). The S41 represents FEXT and its characteristic of the frequency domain is shown in Fig. 7 (b).
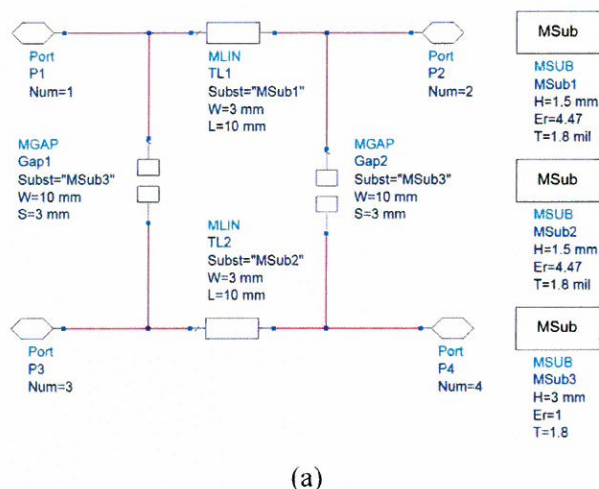
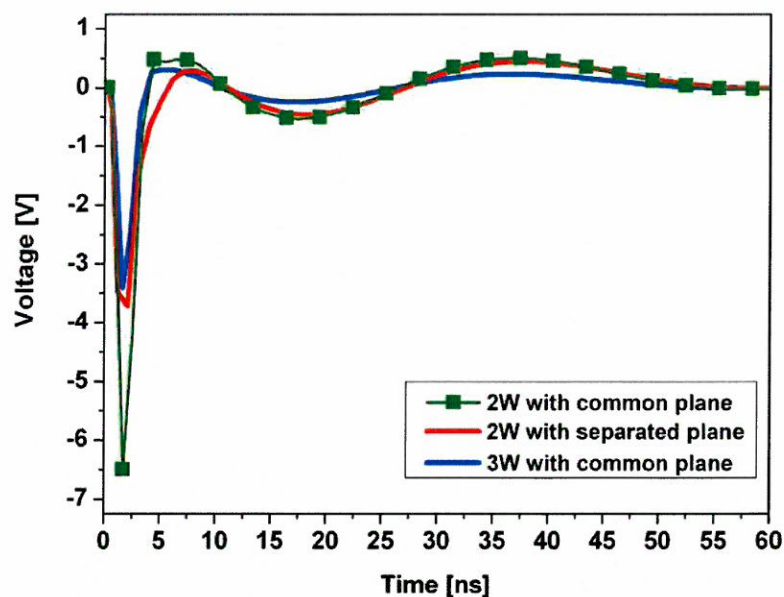

(a)
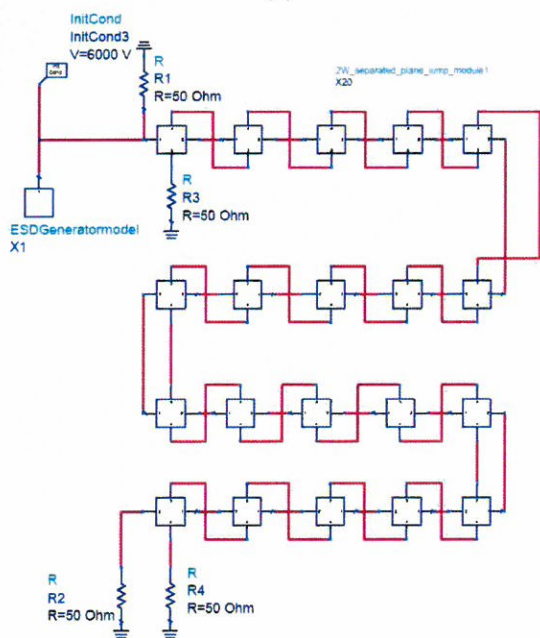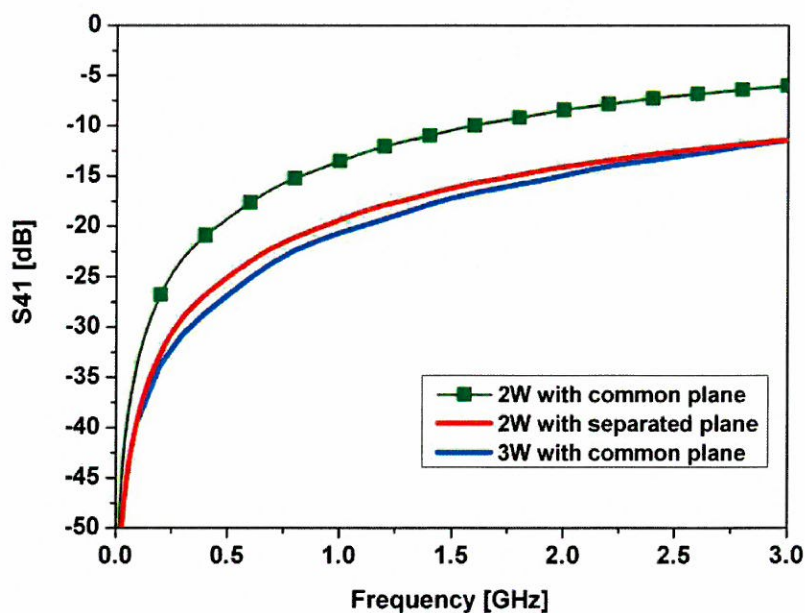

(b)

Figure 6. Separated common plane for (a) Module of 2W spacing (b) ESD simulation of system of 2W spacing

(a)

(b)

Figure 7.   Simulated results for (a) Transient analysis of ADS (b) S41 analysis of ADS

4.2 Experimental results

With the purpose of evaluating the effectiveness of the separated common plane, several experimental setup models, shown in Fig. 8(a) ~8(e), were designed and implemented in FR4 substrate with the height 1.5mm. The width of the traces is all 3mm so that the single-end transmission line impedance is about 50ohm, and the length is 200mm.
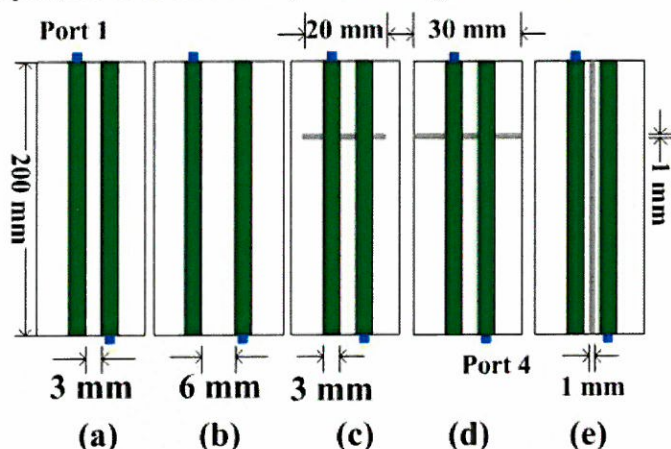
Figure 8. Experimental boards (a) Common plane under the spacing with double trace width (b) Common plane under the spacing with triple trace width (c) Partial slot plane under the spacing with double trace width (d) Whole slot plane under the spacing with double trace width (e) Split plane under the spacing with double trace width

The first experimental case uses 3mm spacing between the aggressor and victim as displayed in Fig. 8 (a). It is constructed using double width signal trace for crosstalk coupling. The second case uses 6mm spacing between the aggressor trace and victim trace, thus this structure exactly meets the general 3W rule design presented in Fig. 8 (b). In Fig. 6 (c), follows the first case but with a separate common plane across through all signal traces and the separated moat width on the reference plane is 0.5mm and the moat length is 20mm. The next case also follows Fig. 6(c) except the moat length is 30mm as shown. The last, separated width and length is the same as in the case in Fig. 6 (d) but the common plane moat is parallel to the signal traces in as displayed in Fig. 6 (d). All traces are terminated at the ends using a 50ohm resistor for impedance matching.

To obtain accurate ESD discharge waveform, a broadband digital oscilloscope Tektronix

74A10 was used to measure the ESD voltage. To avoid interference, both the DUT and DSO were setup inside an EMC chamber. Moreover, the metal walls of the chamber also support an excellent grounding for DSO during measurement. Excellent grounding is also a critical point for the measurement due to different ESD generators having different radiated emissions. Correct and suitable grounding can obtain the same trend in the measured result. The ESD generator was placed outside the chamber with its ground strap connected to the shielding ground of the chamber. Because the DSO maximum input voltage is only 30Vdc, a 20dB attenuator was place near the DSO input port to prevent instrument damage. Port1 induces energy through FEXT to Port4. Enough DSO bandwidth and resolution is another factor for measured result. Injecting 1kV contact ESD energy into the designed PCB structure was performed through a 20dB attenuator with only 1/10 voltage be detected.
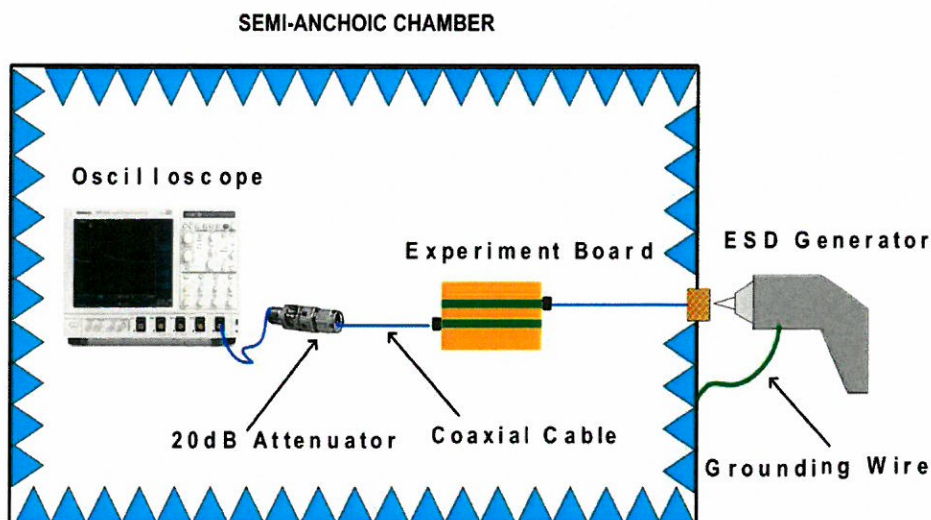

Figure 9.   Configuration of ESD measured system

The ESD generator positive voltage produces negative voltage in the end of victim line due to FEXT. The voltage and current relation of the coupled lines had been described [8] and the FEXT voltage can be calculated as:

$$V_{FEXT}(t) = -\frac{1}{2} \cdot \left(\frac{L_m}{L_s} - \frac{C_m}{C_m + C_s} \right) \cdot t_f \cdot \frac{dV_{in}(t - t_f)}{dt} \quad (4)$$

where C_s and C_m represent the self and mutual capacitances of MTL per unit length respectively. The L_s and L_m represent the self and mutual inductances respectively. The cross section of a coupled MTL pair and the input voltage $V_{in}(t)$ is applied at the active line and is the time of flight along the coupled length is shown in Fig. 10.
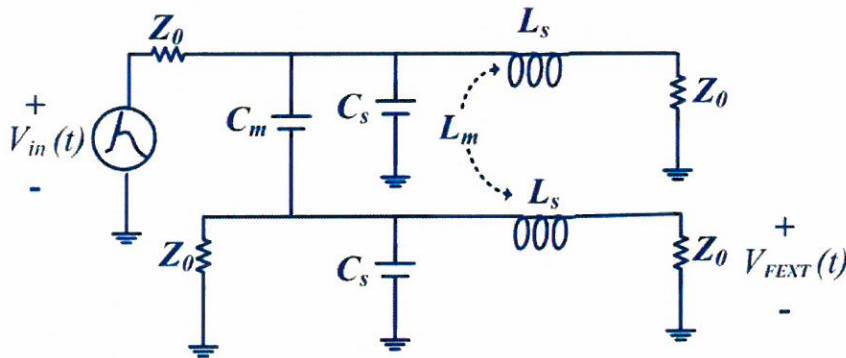
Figure 10.   Equivalent circuit of a coupled MTL pairs

Injecting the ESD positive 1kV using the contact mode delivered to several designed structures and the actual measurement results in the time domain is displayed in Fig. 11. They show that the 2W structure with separated common plan has low FEXT as well as the structure of 3W with the common plan. In other words, the separated plane is a more effective solution than the normal 2W spacing structure for crosstalk reduction in the same PCB 2W spacing layout. Moreover, the 2W structure with partial slot plane is an incorrect separated plane structure. It will induce larger FEXT due to a discontinuous reference plane.   The aggressor's energy cannot return back to the source from the common plane by the shortest path, and moves along the slot into the victim. In the 2W structure with the whole slot plane, the above phenomenon becomes more serious. It rises up to 170% FEXT voltage over the normal 2W spacing structure. That is the worst case for crosstalk reduction in the designed structures. The VNA measured results for the S41 parameter present that the slot common plane produces more serious reflection than the other structures and the aggressor's energy couples to the victim

beginning from low frequency. This is a good explanation for dissimilar contrast as shown in Fig. 12. This comparison demonstrates that the PCB structures in Figs. 8(b) and 8(e) have the lowest crosstalk influence of all designed cases. They obtain about 6dB improvement greater than the normal 2W structure with the common plane.
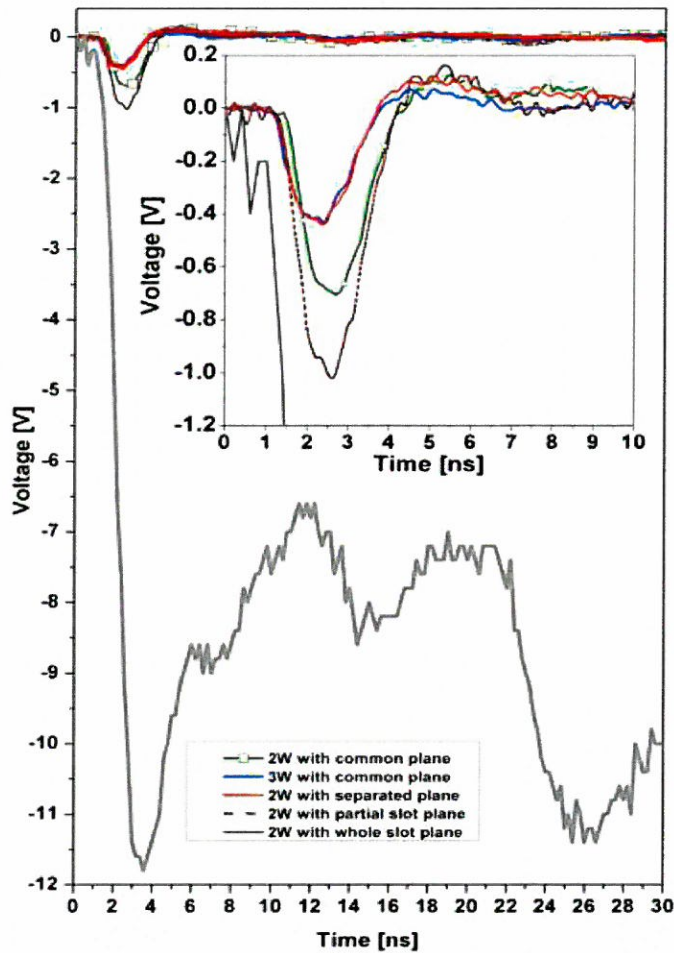
Figure 11.   Measured Results of FEXT voltage
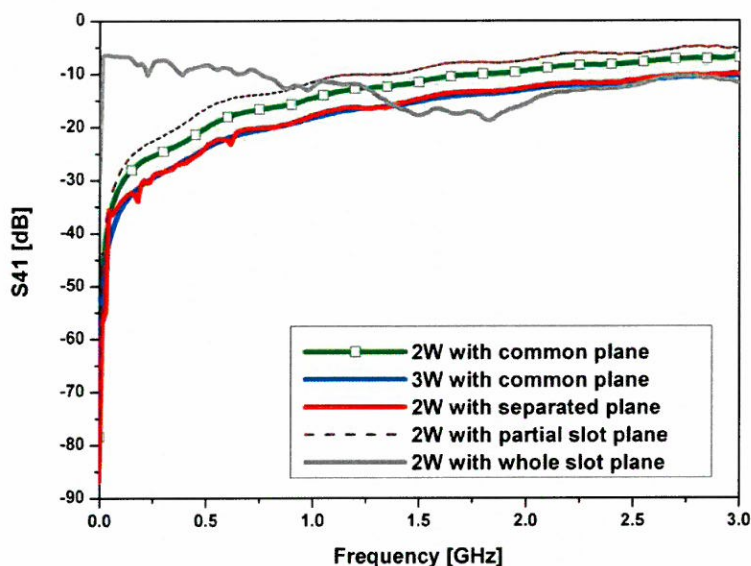
Figure 12.   Measured comparisons for S41

5. Conclusion

This study successfully implemented an equivalent ESD generator circuit model. The proposed model was confirmed accurate after verification against the IEC61000-4-2 standard. An effective ESD measurement system was developed to analyze the ESD phenomenon was another important contribution of this study. The benefit of this approach is that the proposed system can be used to analyze more complex systems. Moreover, this study demonstrates that a separated common plane can be utilized to increase the ESD immunity without extra spacing. The proposed method performed as well as the original design with approximately 4~5dB improved effectiveness in the S41 parameter and falling down about 40% FEXT voltage. This novel technique also performed easily and effectively for practical industrial applications and is helpful for designing a better ESD for PCB. Further research will explore the influence of a separated common plane on signal integrity (SI) and radiated emissions.

Acknowledgments

References

[1] T. Mori and K. Shinozoki,"Analysis of ESD Immunity of Electronic Equipment Based on
Ground Potential Variations," IEICE Trans. on Communication, vol. E79-B, no. 4, 1996,
pp. 515-521.

[2] T. Sudo, H. Sasaki, N. Masuda, and J. L. Drewniak,"Electromagnetic Interference (EMI) of
System-on-package (SOP)," *IEEE Trans. Adv. Packag.*, vol. 27, May 2004, pp. 304-314.

[3] J. F. Legier, E. Paleczny, K. E. Bouazzati, D. Deschacht, and F. Huret,"Imperfect Return
Path Effects on RLCG Model of Single and Coupled Interconnects: Propagation Delay,
Rise Time and Crosstalk Prediction," *9th IEEE Workshop on Signal Propagation on
Interconnects*, 2002, pp.19-21.

[4] G. H. Shiue, S. M. Lin, and R. B. Wu,"Reduction in Reflections and Ground Bounce for
Signal Line Through a Split Power Plane by Using Differential Coupled Microstrip Lines,"
Proc. IEEE 12th Topical Meeting Elect. Performance Electron. Packag., 2003, pp. 107-110.

[5] H. Y. Shim, J. Kim, and J. G. Yook,"Modelling of ESD and EMI Problems in Split Multi-
layer Power Distribution Network," *Proceeding of 2003 IEEE International Symposium on
Electromagnetic Compatibility*, vol. 1, Aug. 2003, pp. 48 - 51.

[6] A. Suntives, A. Khajooeizadeh, and R. Abhari,"Using via Fences for Crosstalk Reduction
in PCB Circuits," *IEEE Int. Symp. Electromagnetic Compat.*, Aug 2006, pp. 34–37.

[7] Y. Kayano, M. Tanaka, and H. Inoue,"PCB Structure with a Ground Band for Suppressing
Electromagnetic Radiation," IEICE Trans. on Communication, vol. E88-B, no. 8, 2005, pp.
3182-3188.

[8] Y. S. Sohn, J. C. Lee, H. J. Park, and S. I. Cho,"Empirical Equations on Electrical
Parameters of Coupled Microstrip Lines for Crosstalk Estimation in Printed Circuit
Board," *IEEE Trans. Adv. Packag.*, vol.24, no. 4, Nov 2001, pp.521–527.

[9] Y. J. Kim, H. S. Yoon, S. Lee, and J. K. Wee,"Measurement Based Line Parameters
Extraction Method for Multiple-Coupled Lines in Print Circuit Boards," IEICE Trans. on
Communication, vol. E86-C, no. 8, 2003, pp. 1649-1656.

[10] Advanced Design System (ADS), Agilent technologies, http://eesof.tm.agilent.com/

[11] IEC61000-4-2: Electromagnetic Compatibility (EMC) Part4: Testing and Measurement Techniques, Section2: Electrostatic Discharge Immunity Test (Basic EMC Publication).

[12] Z. Yuan, J. He, R. Zeng, B, W. Chen, and S. Chen,"Transient Near-Field Effect of Electrostatic Discharge," *IEEE Trans on Magnetics.*, vol. 42, no. 4, pp. 795-798, April 2006.

[13] K. Wang, D. Pommerenke, R. Chundru, T. V. Doren and J. L. Drewniak,"Numerical Modeling of Electrostatic Discharge Generators," *IEEE Trans Electromagn. Compat.*, vol. 45, no. 2, May 2003, pp. 258-271.

[14] Z. Yuan, T. Li, J. He, S. Chen, and R. Zeng,"New Mathematical Descriptions of ESD Current Waveform Based on The Polynomial of Pluse Function," *IEEE Trans. Electromagn. Compat.*, vol. 48, no. 3, pp. 589-591, Aug 2006.

[15] S. Caniggia, and F. Maradei,"Circuit and Numerical Modeling of Electrostatic Discharge Generators," *IEEE Transactions on Industry Applications*, vol. 42, no. 6, Nov/Dec 2006, pp. 1350-1357.

[16] F. Centola, D. Pommerenke, W. Kai, T. V. Doren and S. Caniggia,"ESD Excitation Model for Susceptibility Study," *IEEE Int. Symp. Electromagn. Compat.*, vol. 1, Aug 2003, pp. 58-63.

[17] Stephen H. Hall, Garrett W. Hall and James A. McCall, High-Speed Digital System Design, John Wiley & Sons, Inc. 2000.

使用分離共平面在印刷電路板設計
減少串音改善靜電放電耐受度

李永勳   江正雄

摘　　要

　　本論文主要是針對如何在印刷電路板上改善靜電放電耐受度以加強產品可靠性。首先討論的是 IEC61000-4-2 所規範的靜電放電產生器，其放電電流波形在法規上的要求，再據此建立起靜電放電產生器的等效電路模型，並以數學方程式和實際量測驗證其準確性。然後利用此干擾源在不同的印刷電路板結構上作分析。正因為串音干擾是引起靜電放電導致產品功能受影響的主因之一，所以本文之研究針對降低串音干擾的方法上提出分離共平面的印刷電路板結構，同時在時域和頻域上作比較。最後，理論、模擬和量測數據得到一致結論。此方法至少具體以下幾個優點：(1)較好的靜電放電耐受性和較低的串音干擾；(2)較少的印刷電路板幾何空間需求；(3)無需額外元件增加成本即可達成。

Factor Analysis Based on Co-Area of Distributions

Ven-Shiang Huang[1] , Chien-Chang Yen, Nanping Yang, Shu-Cheng Lee, Mao-Sheng Chang

Department of Mathematics, Fu Jen Catholic University

Abstract

We present a simple factor analysis method which is based on a correlated matrix derived from the co-area of distributions and the connection obtained from a graph induced by the correlated matrix. The application is to analyze the data, the calculus course grades and the entrance examinations of mathematical students. This analysis helps educators understand better the current situation and direction of mathematical teaching.

Keywords : factor analysis, co-area, principal component analysis, co-relation matrix

1. Introduction

Multivariate data are information recorded from the behaviors of humans. It could be wide and various types, such as, for example, the grades of students, the weight of individuals, the age of people, etc. Usually, there are several factors for each person. Once the target factor or goal is determined, people are interested in the significant factors among others. A traditional method is using linear regression to probe the correlation of two factors. The more advanced approach is principal component analysis (PCA) [3].

[1] Corresponding author: Tel :886-2-2905-2574
　　　　　　　　　Fax:886-2-2904-4509
　E-mail address: 001984@mail.fju.edu.tw

We first analyze the factors by the traditional method and demonstrate that the standard deviations are too large to interpret the meaning of the data correctly. Such phenomena often happen in multivariate data from time to time.

The PCA method may cure the drawback and provide us with an exploratory tool. This method would explore correlations between factors. This method is both useful and a way of dimension reduction, but it transforms data into others. The correlation [4] is indicated from the transformed data.

The method for factor analysis [2] proposed here comes from the first principle, that is, "meaning of correlation". The correlation is defined to calculate the correlated coefficients derived from the co-area based on the distributions of data. That is, we calculate the area of the overlap region of distributions. We represent the correlated matrix by a graph through a stop criterion. We verify the result by the PCA method. Both results are consistent. The characteristics of students can provide suggestions to teachers how to help students learn and study.

The sample data used in this paper are introduced as following: Each record contains six components, denoted by $u = (x_1, x_2, x_3, x_4, x_5, x_6)$ which are Calculus, Mathematics (MA), Chinese (CH), English (EN), Physics (PH), and Chemistry (CM) grades, respectively. The component x_1 is the fall semester grade. The other components $x_2 \sim x_6$ are the entrance examination grades. The sample data are from students majored in mathematics. There are 98 students in 2005 academic year, 101 students in 2006 academic year, and 97 students in 2007 academic year. Let E be the collection of all the sample data.

We demonstrate the result analyzed by the linear regression analysis in section 2. The drawback of this method is the large standard deviation. We explain our method in section 3 and the results are shown in section 4. Finally, the conclusion and discussion are given in section 5.

2. A Priori Analysis

We begin to calculate both the mean and the variance for the given dataset E in order to understand the data tendency. The relations between the target factor (calculus) and the others are shown by the linear regression in Figure 1. The linear regression is the line $\ell(x) = mx + b$ in each plot (figure 1). We calculate the standard deviation by
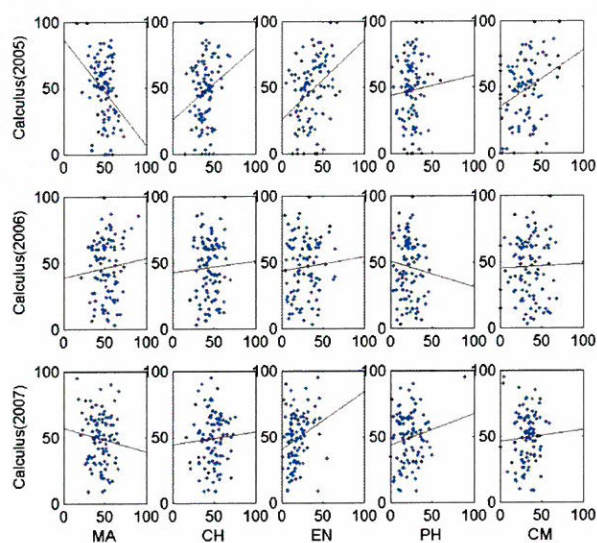
Figure 1.   This figure shows the relationships between calculus and the other five components by means of linear regression. The drawback is that the standard deviation (table 1) are almost the same and can be observed in the plots, Calculus (2005)-PH, Calculus (2006)-MA, Calculus(2007)-CH, etc. The plots from top to bottom are from 2005 to 2007, respectively.

$$\sqrt{\frac{1}{n}\sum_{k=1}^{n}(u_{k,1} - \ell(u_{k,j}))^2}, \, j = 2, \ldots 6,$$

where n is the sample size that the date set involved. The values of the standard deviation given in Table 1 shows that non of the subjects is an essential factor for calculus learning. See Calculus (2005)-PH, Calculus (2006)-MA, Calculus(2007)-CH, etc.

Table 1. This table shows the standard deviation values, which corresponds to Figure 1.

Year	Math	Chinese	English	Physics	Chemistry
2005	22.84	23.64	22.55	24.19	23.02
2006	22.16	22.21	22.17	22.15	22.22
2007	19.30	19.38	18.78	19.14	19.38

3. Factor Analysis Based on the Co-Area of Distributions

An observational data is denoted as $u_k, k = 1, \ldots n$. Each event u_k has λ components, that is, $u_{k,j}$, $j = 1, \ldots \lambda$. Our method is divided into four steps:

<u>Step 1.</u> We calculate the distribution of each factor and normalize it.

<u>Step 2.</u> We calculate the related matrix by co-Area of the distributions.

<u>Step 3.</u> We represent the relation as a graph (edges and vertices).

<u>Step 4.</u> We determine the significant factors.

For step 1, the resolution has to be set and the number of events is calculated on the interval. Hence, distributions are represented as $\{v_{i,j}\}, j = 1, \ldots \lambda$. Step 2 is to calculate the correlated matrix which is defined by

$$R_{j_1, j_2} = [v_{\bullet, j_1}, v_{\bullet, j_2}],$$

where $[v_{\bullet, j_1}, v_{\bullet, j_2}] = \sum_i \min\{v_{i, j_1}, v_{i, j_2}\}$ and $\|v_{\bullet, j}\| = [v_{\bullet, j}, v_{\bullet, j}] = 1$. For step 3, the vertices are the components and the edges are the connections which depend on the values of the correlated matrix. The connection edge is added by the order of the magnitude until the stop criterion happens. Then we represent the connections as a graph. We may demonstrate our method by means of the following example. A dataset is given (not shown here) which has the distribution $v_{i,j}$ in the following table.

Table 2. The distribution of a dataset used as a demonstration

Interval	A	B	C	D
0-10	0	2	7	0
11-20	4	2	1	0
21-30	2	3	8	0
31-41	0	3	0	9
41-51	2	0	0	6
51-60	8	6	0	1

The corresponding related matrix is

$$R = \begin{bmatrix} 1 & 0.69 & 0.19 & 0.19 \\ 0.69 & 1 & 0.38 & 0.25 \\ 0.19 & 0.38 & 1 & 0 \\ 0.19 & 0.25 & 0 & 1 \end{bmatrix} \tag{1}$$

We represent the correlation by a graph below. In the stop criterion, every component at least has an edge and the minimum edge is one. The connection edges are A-B, B-C, and B-D, the corresponding values are 0.69, 0.38, and 0.25.
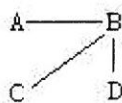
Figure 2. This graph shows the connection edges derived from the related matrix in (1)

For step 4, the significant factor is B because it has the maximum number of edges.

4. Results

We investigate the significant factors for the grades of calculus and the entrance examination data of the years from 2005 to 2007. For the distribution of each factor, the lengths of the intervals are 1, 5 and 10 scores. The correlated matrix (shown in Table 3.1~Table 3.3) is calculated from the distributions.

We observe the following topics: The first one is to probe the significant factors of the entrance examinations. Therefore, the first row is ignored. Those graphs are shown in Figure 3. The stop criterion is set so that a vertex among them has reached 3 edges. The second observation is to understand the significant factors with respect to mathematics. The third observation is to probe the significant factors with respect to calculus.

Table 3.1   Each sub-table shows the correlated coefficients of factors. From the left to right, the sub-tables are the years from 2005 to 2007 years. The resolution interval is1 score. The "*" means that the p-values is less than 0.05 and "**" is less than 0.01.

	2005					2006					2007				
	MA	CH	EN	PH	CM	MA	CH	EN	PH	CM	MA	CH	EN	PH	CM
Calculus	0.29	0.27	0.41	0.27	0.33	0.39	0.43	0.22	0.31	0.37	0.49**	0.47**	0.17	0.26	0.34
MA		0.31	0.33*	0.10	0.21		0.41**	0.12	0.04**	0.29		0.49**	0.13	0.23**	0.34
CH			0.49**	0.31	0.45**			0.24*	0.16	0.39**			0.15	0.26	0.34**
EN				0.39*	0.37				0.43**	0.31				0.57**	0.34
PH					0.45**					0.22					0.45**

Table 3.2   Each sub-table shows the correlated coefficients of factors. From the left to right, the sub-tables are the years from 2005 to 2007 years. The resolution interval is 5 scores. The "*" means that the p-values is less than 0.05 and "**" is less than 0.01.

	2005					2006					2007				
	MA	CH	EN	PH	CM	MA	CH	EN	PH	CM	MA	CH	EN	PH	CM
Calculus	0.43	0.41	0.58	0.43	0.63	0.57**	0.51*	0.55	0.37	0.61*	0.68**	0.62*	0.23	0.38	0.43
MA		0.45	0.49	0.16	0.31		0.63**	0.29	0.10	0.47		0.77**	0.19	0.34	0.43
CH			0.65**	0.45	0.57*			0.43	0.27	0.65**			0.21	0.36	0.40
EN				0.65**	0.71**				0.57**	0.65**				0.81**	0.51
PH					0.69**					0.45					0.68**

Table 3.3   Each sub-table shows the correlated coefficients of factors. From the left to right, the sub-tables are the years from 2005 to 2007 years. The resolution interval is 10 score. The "*" means that the p-values is less than 0.05 and "**" is less than 0.01.

	2005					2006					2007				
	MA	CH	EN	PH	CM	MA	CH	EN	PH	CM	MA	CH	EN	PH	CM
Calculus	0.47	0.43	0.61	0.47	0.63	0.67*	0.55	0.59	0.41	0.72	0.70*	0.66	0.23	0.38	0.47
MA		0.45	0.49	0.16	0.31		0.65*	0.31	0.10	0.51		0.91**	0.19	0.34	0.43
CH			0.67*	0.47	0.61			0.49	0.29	0.65*			0.21	0.36	0.45
EN				0.67**	0.73*				0.65*	0.78*				0.83**	0.57
PH					0.76**					0.49					0.74*

Let us summarize it in Table 4 by means of graphs. The multi-related factors mean the factor reaches the maximum edges. The related Calculus (MA) means the factor has a relation with calculus (mathematics). The results show us that the first three significant factors and the related MA factors are the same for Chinese, English, and Chemistry. The related calculus is the same conclusion, except for the Mathematics factor. The verification of the results for a multivariate data is difficult. Here, we employ the PCA to justify our results. We use the total data and the result is shown in Table 5 below. The results show that that the significant factors are EN, EN and PH related to Calculus and MA, respectively.
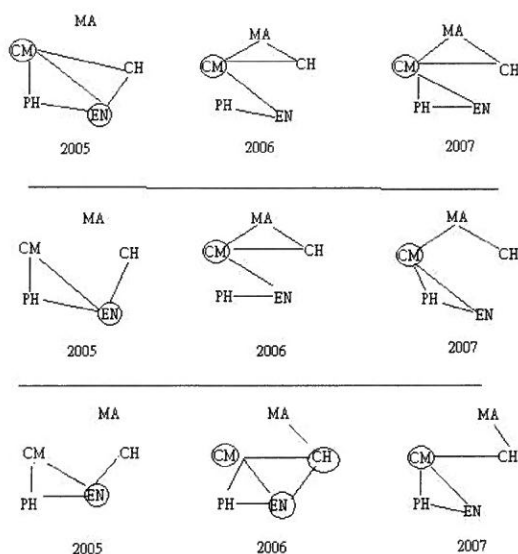
Figure 3. This graph shows the connection edges between the MA, CH, EN, PH, and CM factors from 2005 to 2007. The corresponding intervals of resolution are 1,5,10 from the top to bottom row.

5. Conclusion and discussion

We have presented a simple method of factor analysis based on the first principle, which consists of correlated matrices and a graph representation. Such presentation also shows us the connection relation. The assumption of our method is obvious, but it is truly meaningful and easily understood. For an analysis of the multivariate data, the result is consistent with the PCA.

Table 4.   This table shows the significant factors. The first three significant factors and correlation with an MA are Chinese, Chemistry and English. For correlation with calculus, the result is the same except for Mathematics.

Interval	Year	Significant factor	Related MA	Related Calculus
	2005	CM,EN	EN,CH	EN,CM
1	2006	CM	CH, CM	CH,MA
	2007	CM	CH, CM	MA,CH
	2005	EN	EN,CH	CM,EN
5	2006	CM	CH,CM	CM,MA
	2007	CM	CH,CM	MA,CH
	2005	EN	CH,EN	CM,EN
10	2006	CM,EN,CH	CH,CM	CM,MA
	2007	CM	CH,CM	MA,CH

Table 5.   This table is calculated by PCA. There are two values in each correlation, the upper value is the related coefficient and the lower value is the p-values. The p-values are less than 0.05 which means the related coefficients are strongly meaningful. The results show that that the significant factors are EN, EN and PH related to Calculus and MA, respectively.

|	Calculus	MA	CH	EN	PH
MA	0.031	X	X	X	X
	0.600	X	X	X	X
CH	0.077	-0.112	X	X	X
	0.184	0.053	X	X	X
EN	0.149	-0.139	-0.280	X	X
	0.010*	0.017*	0.000*	X	X
PH	0.036	-0.125	-0.253	0.067	X
	0.531	0.031*	0.000*	0.248	X
CM	0.094	-0.066	0.477	-0.265	-0.067
	0.107	0.255	0.000*	0.000*	0.251

An application our method has been demonstrated and the multivariate data is the grades of students. The result shows us the first three significant factors are Chinese, English, and Chemistry.

We also investigate the resolutions interval for the sample data. The result does not need to be changed too much. The stop criterion may lead to more complicated results and thus be hard to interpret the result. For this point, the user should understand the situation of reality. The scaling factors will occur at the various ranges of factors. We do believe that this effect does not have a lot of influence on our data.

We expect that this method can be applied on analyzing the data of students more deeply. Furthermore, the interpretation of the results can help educators develop the structure of their courses or the goal of their departments [1].

References

[1]   A. Ben-Israel and R. Gilbert, Computer-supported calculus, Springer-Verlag, (2002)

[2]   R. J. Muirhead, *Aspects of Multivariate Statistical Theory*, (1982).

[3]   C. R. Rao, *The Use and Interpretation of Principal Component Analysis in Applied Research*, Sankhya A 26, 329-358 (1964).

[4]   R. J. Wherry, *Contributions To Correlational Analysis*, (1984).

分佈共面積因子分析法

黃文祥　嚴健彰　楊南屏　李樹政　張茂盛

輔仁大學數學系

摘　　要

　　在本論文中我們利用分佈的共面積計算關係矩陣及用其圖形來分析因子。我們將此方法應用於分析學生的微積分成績與入學成績之相關性。所得分析結果有助於教育工作者更明白教學的狀況及方向。

關鍵字：因子分析法，共面積，圖形，關係矩陣

應用有限差分法於神經元動作電位之波形分類

林文彬　黃貞瑛[1]

輔仁大學資訊工程系

嚴健彰[2]

輔仁大學數學系

摘　　要

本文主要探討神經元動作電位（或稱棘波）的波形分類問題，此問題的前置處理中，除了挑選重要的特徵值外，還有降低維度的作用。我們應用有限差分法於棘波分類的特徵選取，此方法主要是針對動作電位而設計的特徵選取法，稱爲極小極大特徵值選取法(Min-max Reduced Feature Set)，以下簡稱爲 mRFS 方法。

mRFS 的主要精神在於透過不同階數的有限差分，挑選出最能突顯出不同種類的動作電位所產生的棘波。本文將於實驗中，驗證 mRFS 方法的有效性，並與其他兩種特徵選取法比較，分別爲主成分分析法 (Principal Component Analysis) 與小波轉換法 (Wavelet Transform)。

本文更延展 mRFS 的方法，利用側影係數(Silhouette Coefficient)的指標，嘗試提供一個最佳範圍的分群數。另外使用 Kolomogorov-Smirnov test (KS Test)挑選合適的特徵值，使得特徵值的選擇個數更加具有彈性。以上所提 mRFS 的延伸，經由實驗後，也都驗證具有不錯的成效。

關鍵詞：動作電位(Action Potential)、棘波(Spikes)、有限差分(Finite Difference)

---

[1] Corresponding author : Email: jihwang@csie.fju.edu.tw

[2] Corresponding author : Email: yen@math.fju.edu.tw

1.簡　介

醫學上，研究大腦的活動一直是很熱門的主題，然而研究大腦活動，需要觀察神經元的活動情況。神經元活動時，會發出微電極可以偵測到的動作電位(Action Potential)或稱棘波(Spike)，不同的動作電位可表示不同神經元的活動情形，所以分離動作電位就成為瞭解神經系統的重要課題之一。

分離動作電位的波形可以分成三個步驟：*1.*棘波偵測(Spike Detection)；*2.*特徵選取(Feature Extraction)；*3.*棘波分類(Spike Sorting)。本文主要重點為第二步驟的特徵選取，探討一個以有限差分為基礎的極小極大特徵選取法(Min-max Reduced Feature Set)[Yen08]，後文將以 mRFS 縮寫稱之。本文於實驗中，並分別使用 K-mean、Fuzzy-C-Mean、超順磁性分群演算法(Super Paramagnetic Clustering; SPC)[Blatt96]，於步驟三的棘波分類。至於步驟一的棘波偵測，將不在本文探討的範圍內。

本文為驗證 mRFS 的成效，是透過與主成分分析法(Principal Component Analysis)[Letelier00, Quiroga04, Yen08]及小波轉換法(Wavelet Transform) [Quiroga04]的結果相比較。以上比較的基準主要使用 Jaccard[Greene04]和側影係數(Silhouette Coefficient) [Tan05]這兩個分群指標。

對於 mRFS 只選取兩個特徵值的特性，我們利用 Kolmogorov-Smirnov test (KS Test) [Marsaglia03]選擇不同階數的極小極大特徵值，使得特徵值個數的選取不再受限兩個，因此更具彈性。另外也利用側影係數判斷不同分群的有效性，提供可能分群數的範圍。

本文的章節結構如下：第二章將介紹棘波和棘波的波形分類所需之三步驟；除此之外並簡介所使用的資料庫；第三章則是介紹 mRFS 方法以及描述 mRFS 方法的延伸；第四章以實驗驗證第三章所探討的主題；最後，第五章為本文的結論及其未來研究的展望。

2.相關背景知識

本章將介紹動作電位的波形，也就是棘波，以及說明棘波的波形分類所需的三個步驟，分別為棘波偵測、特徵選取及棘波分類，並且描述本文中使用的資料庫。

2.1 棘波分類介紹

棘波是指腦電波紀錄中，和背景活動有明顯區別，並且具有短暫尖鋒的波形。棘波與神經元動作電位產生相關，當發生一次動作電位的時候，腦電波紀錄中也會紀錄到一

次棘波波形。因為不同神經元有不同的動作電位大小，所以也會有不同的棘波波形。

在紀錄腦電波時，通常一根微電極會同時紀錄到多個神經元細胞所產生的動作電位。一般研究時，需將不同的神經元細胞所產生的動作電位紀錄分開，這個分開的過程就叫做棘波分類。

分類方法通常是比對動作電位的波形，將不同神經元所發出的動作電位分開。這種做法一般會有兩個基本假設：

　　1.不同神經元細胞所產生的波形紀錄會有所不同。

　　2.同一神經元細胞所產生的波形不會隨時間改變。

實際上第一個假設一定會成立，因為就算是同一個神經元也會因為微電極擺放位置和神經元細胞距離的不同，所紀錄到的腦電波波型紀錄也會有所不同，更何況如果是不同的神經元，其和微電極的距離必定不相同。至於第二個假設，則是為了簡化問題。

實際進行腦電波實驗時，通常所紀錄的除了原始的訊號外，還會有環境雜訊和生物上所產生的雜訊，其中生物上所產生的雜訊來自於生物體內各種活動的干擾，因此這些雜訊的產生也會造成棘波分類的困難。

2.2 棘波分類的步驟

完整的棘波分類流程一般可分為三個步驟，分別為棘波偵測、特徵選取，及棘波分類，以下將針對這三個步驟做詳細的介紹。

2.2.1 棘波偵測

處理原始腦電波訊號的第一個步驟為棘波偵測，其目的是擷取腦電波紀錄中的動作電位。偵測方式可利用帶通濾波器(Bandpass Filter)，然後透過門檻值偵測。如果超出門檻值，就認為是一個棘波。例如：可使用公式(1)[Othman05, Quiroga04]設定門檻值 Thr，而 σ_n 是估計的標準差，median 則是中位數。

$$Thr = 4\sigma_n \quad ; 其中 \quad \sigma_n = median\{\frac{|x|}{0.6745}\} \tag{1}$$

上述的偵測方式，已經隱含同一時間只會產生一個神經元動作電位的假設，如果同時有多個神經元產生動作電位，這種現象稱為重疊(Overlap)，若考慮重疊[Rinberg03]，情況將更為複雜，本文將不考慮有關重疊的問題。

2.2.2 特徵選取

　　棘波偵測後，一般會做特徵選取，以便於步驟三的棘波分類。尤其特徵選取後，資料維度降低，有利於即時呈現分析結果的需求。

　　在棘波分類的問題中，特徵選取最常見的方法有主成分分析法 [Letelier00, Quiroga04]，及資料經過小波轉換後使用 KS test [Marsaglia03]，選擇重要的小波係數 [Quiroga04]，本文所探討的 mRFS 方法[Yen08]是另一種針對棘波分類問題所設計的特徵選取法。

2.2.3 棘波分類

　　經過特徵選取後，便可利用選取出來的特徵，將不同的神經元所產生的棘波分開。在實際問題中，並無法得知棘波的波型是由那個神經元所產生的，因此一般都是使用分群(Clustering)演算法。

　　一般的棘波分類問題，較常使用的分群演算法是 K-mean 分群演算法，本文實驗部分除了使用 K-mean 外，還使用根據物理學理論所推導的超順磁性分群演算法[Blatt96]，另外還有根據 K-mean 演算法改良而成的 Fuzzy-C-Mean 分群演算法。

2.3 資料庫簡介

　　本文中所使用的實際資料庫(Real Data Set)為宜蘭大學蔡孟利博士所提供，除了使用實際資料外，本文還使用人工製造的資料，以利實驗結果的分析。

　　人工資料的製造方式是先製造四種不同分類的棘波，見圖一，其中第一類和第四類代表振幅較小的相似棘波，而第二類和第三類代表振幅較大的相似棘波，每種分類各有五百筆，所以共有兩千筆棘波資料。

　　人工製造的棘波，除了有四種不同的波形，並再加入雜訊。其合成方式乃模仿真實的雜訊，雜訊的取得為實際資料中去除真實棘波的部份，並將所有的雜訊資料連接在一起；而人造棘波加入雜訊的方式，是從上述的雜訊資料中，隨機選取一段加入每個人造棘波的資料，最後再加上高斯雜訊，作為背景雜訊。如此所得到的人工資料(見圖二)，便是加上生物以及背景雜訊所合成的棘波。
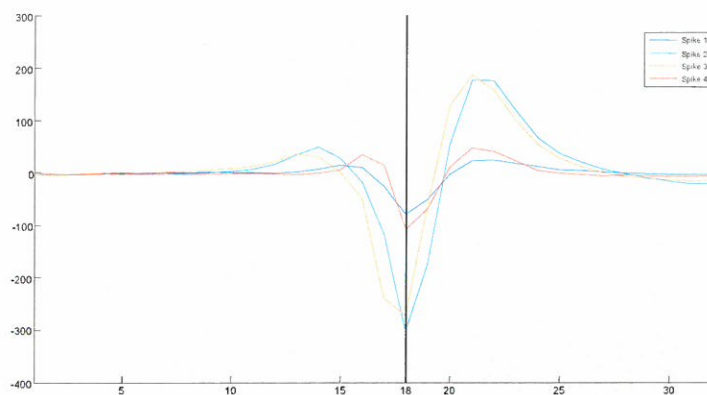
圖一　四個人造的棘波
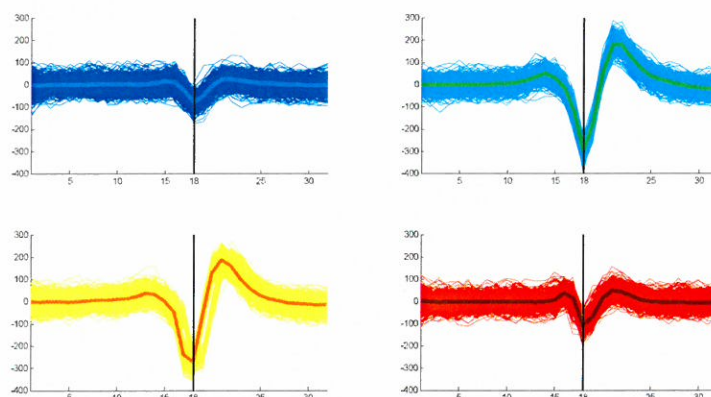
圖二　人造的棘波加上生物雜訊和高斯雜訊

3. mRFS 方法

本章將介紹 mRFS 方法[Yen08]，首先描述其方法及設計理念，最後並介紹如何延伸 mRFS 的方法。

3.1 mRFS 方法的概念

mRFS 方法的構想來自於 Letelier 和 Weber 所提出的 Wavelet Based Spike Classifier(WSC)[Letelier00]，WSC 方法是將原始訊號做小波轉換(Wavelet Transform)，轉

換後的訊號有平均(Average)和差分(Difference)兩個部分，平均的部分會將原始訊號平滑化(Smooth)，而差分的部分會將原始訊號差異的部分放大。棘波的特性之一是和背景的訊號差異很大，所以如果將訊號平滑化，反而違反棘波的特性，所以 mRFS 的設計，只做有限差分而不計算平均，是一個專門針對棘波所設計的特徵選取法，以下將說明 mRFS 的方法。

原始資料經過棘波偵測後，假定得到 N 個事件(Events)，即有 N 個棘波。每個棘波假設有 λ 個樣本點(Samples)，亦即為每個棘波取 λ 個點。經過棘波偵測後的資料可以使用公式(2)表示，其中 v_i 表示第 i 筆棘波資料。

$$V_i = (v_1^i, v_2^i, v_3^i, \cdots, v_\lambda^i)$$
$$V = \begin{bmatrix} V_1 \\ \vdots \\ V_N \end{bmatrix} \tag{2}$$

mRFS 方法將原來每個棘波所使用的 λ 個樣本點，轉換成只用二個特徵值表示，而此兩個特徵值分別代表極小(Minimum)和極大(Maximum)。

其流程可敘述如下：

(1) 將 $v_i, i = 1,2,\cdots, N$ 經過有限差分(Finite Difference)運算後得到 $D_j V$，其中 j 表示有限差分的階數，如公式(3)所示，w 表示經過有限差分運算後所得到的值，而有限差分的過程請見公式(4)。

$$D_j v_i = (w_1, w_2, \cdots, w_\lambda) \tag{3}$$

$$w_l = \sum_{m=0}^{j} (-1)^m C_m^j v_{l-m+j}, \quad l = 1,2,\cdots,\lambda \quad, C_m^j = j!/(m!(j-m)!) \tag{4}$$

其中公式(4)中的有限差分也可以看成是原始訊號 v_{l-m+j} 和 $(-1)^m C_m^j$ 做迴旋積(Convolution)的結果。有限差分的過程中，若超出範圍，則在後面補零(Zero-padded)。

(2) 將 $D_j V$ 中，整個棘波中發生最多次最低點（最高點）的位置值，紀錄為 $p_j(q_j)$。

對每個 $p_j(q_j)$，可畫出以 x 軸為 $(D_j V)_{p_k}$ 和 y 軸為 $(D_j V)_{q_k}$ 的圖形，其中 j 值為 0 到 $p-1$，例如當 $p = 5$ 時，可以畫出圖三。當 $j = 0$ 時，表示其為原始訊號，沒

有經過有限差分運算，$j = 1$ 時則將原始訊號做過一次有限差分，其餘依此類推。

mRFS 之所以選擇極小極大點爲特徵值，乃是針對棘波的特性所設計，因爲動作電位產生的過程，極大值的部分恰好是鉀離子通道的完全開啓，極小值的部分則是鉀離子通道的完全關閉。

原始訊號經過 p-1 階數的有限差分後，將各種不同階數(0～p-1)的極小極大值做各種組合，產生 P^2 對特徵值，如圖三中的第二列第三行所呈現的爲 p_1 及 q_2 兩個特徵值，所分群的結果。
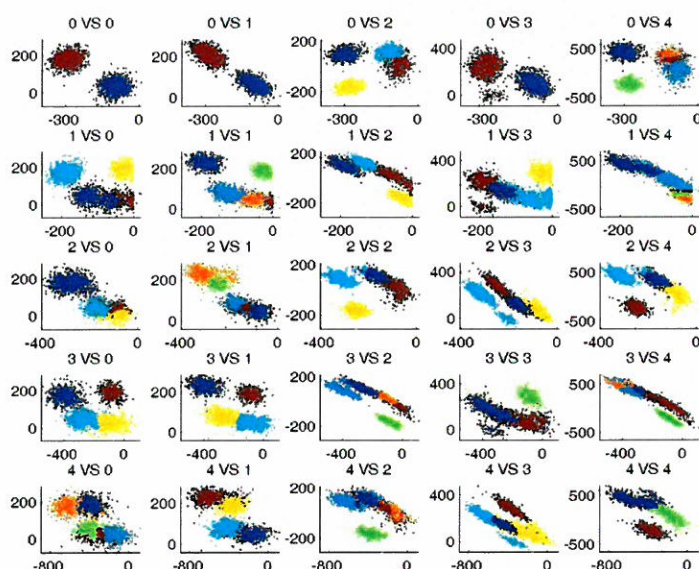
圖三　組合不同階數的 P^2 對特徵值所分群的結果；其中 x 軸為 p_k，y 軸為 q_k

最後 mRFS 採用觀察法於所呈現的圖三，決定使用那一對特徵值較好。由於 mRFS 採用窮舉法列出所有不同階數組合的特徵值配對，並且使用觀察法作爲選取的方式。因此，本文針對窮舉法及觀察法的弱點提出改進。

3.2 mRFS 方法的延伸

前文中曾提到，mRFS 是利用視覺化的圖形，然後採用觀察法採定某組特徵值(p_k, q_k)。針對此缺點，我們將使用分群指標，決定那一組特徵值較好。本文將使用兩種指標

來測度，分別是 Jaccard[Greene04]和側影係數[Tan05]。這兩種指標最大的差異點是 Jaccard 的計算，需要真正的分類結果，而側影係數則不需要事先已知的分類結果，僅靠群和群之間的關係(Between)和同一群內的緊密程度(Within)來計算。

在使用 K-mean 和 Fuzzy-C-Mean 分群演算法時，最困難的問題就是決定群數的個數，本文第四章的實驗將會使用側影係數的分群指標值，提供合適群數的範圍。

特徵選取方法中，Letelier 提出可以用最大平均值、標準差等方法挑選重要的小波係數[Letelier00]；之後 Ben-Shaul 等人，在 2004 年中提出使用 KS test 挑選小波轉換後的小波係數[Quiroga04]。經過實驗驗證後，可以發現使用 KS test 挑選的特徵值，其分群效果較好。因此我們在延伸 mRFS 的方法中，使用同樣的技巧，在 0 到 p-1 階的有限差分中，共有 $2p$ 個特徵值（每一階的有限差分中各有一個極小、極大特徵值），我們使用 KS Test 選擇其中兩個比較重要的特徵值，因此較原始 mRFS 方法客觀。另外，也可以依據不同的需求，使用 KS Test 選擇 3 個或以上的特徵值，因此使得 mRFS 方法更加具有彈性。

4. 實驗結果與討論

本章將使用人工產生的資料和真實資料進行實驗，人工產生 2000 筆資料，每筆資料有 32 個樣本點，即 $N = 2000$、$\lambda = 32$；而真實的資料是，$N = 76$、$\lambda = 29$。

我們首先檢驗 mRFS 的效果，然後提供建議，給予適合的群數，最後使用 KS test 選取適當的特徵值。實驗中使用到下列三種特徵選取法：

(1) 原始及改良後的 mRFS 方法。
(2) Ben-Shual 等人提出的方法，之後將使用 Wavelet 表示。
(3) 主成分分析法，之後將使用 PCA 表示。

另外，實驗將採用下列三種分群演算法：

(1) K-mean 演算法，之後將使用 Kmean 表示。。
(2) Fuzzy-C-Mean 演算法，之後將使用 FCM 表示。
(3) 超順磁性分群演算法，之後將使用 SPC 表示。

4.1 mRFS 的有效性

首先，我們驗證 mRFS 特徵選取方法的確具有成效。因此實驗中會比較 mRFS 和最常見的 PCA 與 Wavelet 的特徵選取法，實驗中利用 Jaccard 指標驗證方法的有效性，之所以選用 Jaccard 指標驗證而不用側影係數，最主要的原因是 Jaccard 指標會參考分類標

準答案。另外，雖然分類正確率也會參考分類標準答案，但是必須分出的群數和實際的群數相同，若以採用的 Jaccard 指標而言，則是公式中的 C 和 K 必須一致，因此 Jaccard 指標的適用性較分類準確率更佳，因此本文採用 Jaccard 指標。

　　圖三爲採用 mRFS 特徵選取法，並使用 SPC 分群演算法後得到的圖形，若利用 Jaccard 分群指標計算，則可得到表一，表中 Jaccard 指標表現最佳的極小極大組合是 4VS1(即最小值採四階有限差分，而最大值採一階有限差分)。爲瞭解 mRFS 與其他特徵選取法的表現，我們也使用相同的 SPC 分群演算法於 PCA 與 Wavelet 萃取後的資料，其中 PCA 使用兩個最大的主成分當作特徵值，而 Wavelet 使用 KS test 挑選兩個最大的小波係數，其分群結果與 mRFS 的最佳分群結果列於表二。實驗中，mRFS 和 Wavelet 萃取後的資料都被 SPC 分成四群，分群群數符合分類標準答案，因此 Jaccard 值均較 PCA 高，其中 mRFS 方法的 Jaccard 指標爲最高，從而驗證 mRFS 方法較 PCA 與 Wavelet 爲佳。

表一　採用 mRFS 特徵選取法，及 SPC 分群法的結果

極小 VS 極大	群數	Jaccard	極小 VS 極大	群數	Jaccard
0VS0	2	0.50	2VS3	4	0.72
0VS1	2	0.50	2VS4	4	0.75
0VS2	4	0.69	3VS0	4	0.74
0VS3	2	0.50	3VS1	4	0.76
0VS4	5	0.64	3VS2	5	0.68
1VS0	4	0.57	3VS3	3	0.44
1VS1	5	0.69	3VS4	5	0.57
1VS2	4	0.74	4VS0	5	0.62
1VS3	4	0.60	4VS1	4	**0.79**
1VS4	5	0.39	4VS2	5	0.57
2VS0	4	0.51	4VS3	4	0.55
2VS1	5	0.62	4VS4	3	0.48
2VS2	4	0.72			

表二　採用 Wavelet、PCA 和 mRFS 的特徵選取法，再使用 SPC 的分群結果

方法	群數	Jaccard	
Wavelet	4	0.62	
PCA	3	0.59	
mRFS	4	**0.79**	4VS1

4.2 適合的群數

　　使用 SPC 分群演算法時，演算法本身會自動決定群數，但是使用 Kmean 和 FCM 分群演算法時，群數是參數之一。在真實情況中，通常沒有辦法先得知實際上應該分成多少群，所以本節將透過人工產生的資料，觀察各種指標的變化，嘗試能否建議適合範圍的群數。

　　表三是使用本文所介紹的三種特徵選取法，分別是 Wavelet、PCA、mRFS，而後使用 Kmean 及 FCM 分群，分群群數由 2 到 10，藉以觀察其變化。觀察表三中較高 Jaccard 值產生的情形，在 Wavelet 特徵選取法時是兩群或三群，PCA 都是三群，mRFS 都是四群。當分群數為兩群時，是因為無法分別將第一類和第四類及第二類和第三類的棘波分離。當分群數為三群時，雖然可以將第二類和第三類分離，可是卻沒有辦法分離第一類和第四類。由於 Jaccard 指標值計算時需要參考分類標準答案，所以在使用實際資料時無法採用，只能用在已知分類的人造資料。根據表三的 Jaccard 指標，mRFS 具有較高指標值，因此也可以驗證 mRFS 優於 PCA 和 Wavelet。

　　另外觀察表三的側影係數，可以瞭解其分群效果。如果三種特徵選取法，只取最高的一個數值，可以發現最佳的分群數是介於兩群到三群之間，可是實際上分群群數應是四群，因此可以瞭解側影係數的最佳值並不一定與實際情形相符。如果要利用側影係數以決定最佳的群數，可能只能建議某一範圍的分群數，而無法建議某一特定分群數。例如我們若取每一特徵選取法的最佳三個值，使用 FCM 分群演算法時，Wavelet 和 PCA 建議的分群範圍都是二到四群，剛好包含正確的分群群數四群，反而 mRFS 建議分為二、三、五群，沒有包含正確群數四群。若使用 Kmean 分群演算法，雖然三種特徵選取法都沒有包含分群群數為四群的情況，至少建議的範圍沒有和真實的分群群數差異過大，因此還是可以作為分群群數的參考。

表三　比較三種特徵選取法，使用 Kmean 與 FCM 分群演算法

分群演算法		Kmean		FCM	
特徵選取	群數	Jaccard	側影係數	Jaccard	側影係數
Wavelet	2	**0.50**	**0.88**	0.50	0.88
	3	0.43	0.65	**0.59**	**0.88**
	4	0.40	0.58	0.53	0.81
	5	0.39	0.601	0.45	0.60
	6	0.43	0.57	0.40	0.49
	7	0.42	0.62	0.32	0.43
	8	0.34	0.57	0.30	0.47
	9	0.38	0.60	0.31	0.47
	10	0.37	0.59	0.28	0.50
PCA	2	0.50	0.87	0.50	0.87
	3	**0.59**	**0.91**	0.59	**0.91**
	4	0.56	0.69	0.58	0.84
	5	0.55	0.79	0.55	0.62
	6	0.39	0.59	0.48	0.55
	7	0.51	0.63	0.41	0.53
	8	0.39	0.59	0.40	0.53
	9	0.33	0.52	0.37	0.55
	10	0.40	0.55	0.30	0.49
mRFS	2	0.50	**0.93**	0.50	**0.93**
	3	0.59	0.82	0.59	0.82
	4	**0.77**	0.70	**0.77**	0.70
	5	0.67	0.77	0.68	0.74
	6	0.65	0.72	0.62	0.72
	7	0.62	0.66	0.60	0.68
	8	0.64	0.72	0.46	0.54
	9	0.45	0.61	0.43	0.61
	10	0.47	0.58	0.39	0.52

4.3 特徵值的選取

　　原始的 mRFS 方法，在選擇那一對組合的極小極大值為特徵值時，是將所有可能的情況列出來，爾後使用觀察法，或者可以使用 Jaccard 指標挑選最好的極小極大組合，相較於 Wavelet 與 PCA 的特徵選取法，此種方法所需時間較長，因為所需執行的分群次數為 p^2 次，而 Wavelet 與 PCA 均執行一次分群演算法。所以本文提出採用 KS test 挑選合適的 mRFS 特徵值組合，以避免使用窮舉法。

　　本節將比較三種不同個數的特徵值，分別是二、三、十個特徵值。挑選二個特徵值的情況，是考慮所有階數的有限差分中的極小值與極大值，採用 KS test 分別挑選一個極小值與極大值；三個特徵值的情況，是挑選兩個極小值，一個極大值，挑選兩個極小值的原因是本文所用的資料庫是屬於電位下降時比較重要的棘波；十個特徵值的情況，則是使用全部的特徵值，也就是五個極小值和五個極大值為特徵值。Wavelet 方法，則是分別用 KS test 挑選兩個、三個、十個特徵值；PCA 則是選出最大的兩個、三個、十個主成分。

<p align="center">表四　比較不同特徵值數目；使用 SPC 分群演算法</p>

特徵值數目	分群指標	Wavelet	PCA	mRFS
2	群數	4	3	4
	Jaccard	0.62	0.59	**0.67**
	側影係數	0.87	0.91	0.75
3	群數	4	3	4
	Jaccard	0.62	0.59	**0.76**
	側影係數	0.87	0.82	0.77
10	群數	4	3	4
	Jaccard	0.62	0.59	**0.75**
	側影係數	0.74	0.63	0.66

　　表四為三種特徵選取方法中使用二、三、十個特徵值，分群演算法都是 SPC 演算法，如果只看 Jaccard 指標，無論是兩、三、十個特徵值都是 mRFS 的表現優於 Wavlet 和 PCA。表四中，無論是 Jaccard 還是側影係數分群指標，都沒有因為使用的特徵個數

越多，具有越好的表現，反而在 10 個特徵值的時候，比只用 3 個特徵值時來的低，這表示有些不重要的特徵反而影響到分群效果。

圖四為分別使用二、三、十個特徵值，以 Kmean 及 FCM 分群演算法所執行的實驗結果，以 x 軸為群數，y 軸為指標數值，藍線表示使用 Wavelet，綠線表示使用 PCA，紅線表示使用 mRFS 特徵選取法。圖形上方文字分別標示特徵值個數、何種分群演算法及指標，例如圖四中最左上角有 F2_Kmean_Jaccard 字樣，表示是使用兩個特徵值，分群演算法使用 Kmean，y 軸為 Jaccard 指標。圖中左欄 y 軸為 Jaccard 指標值，右欄 SC 表示側影係數指標。
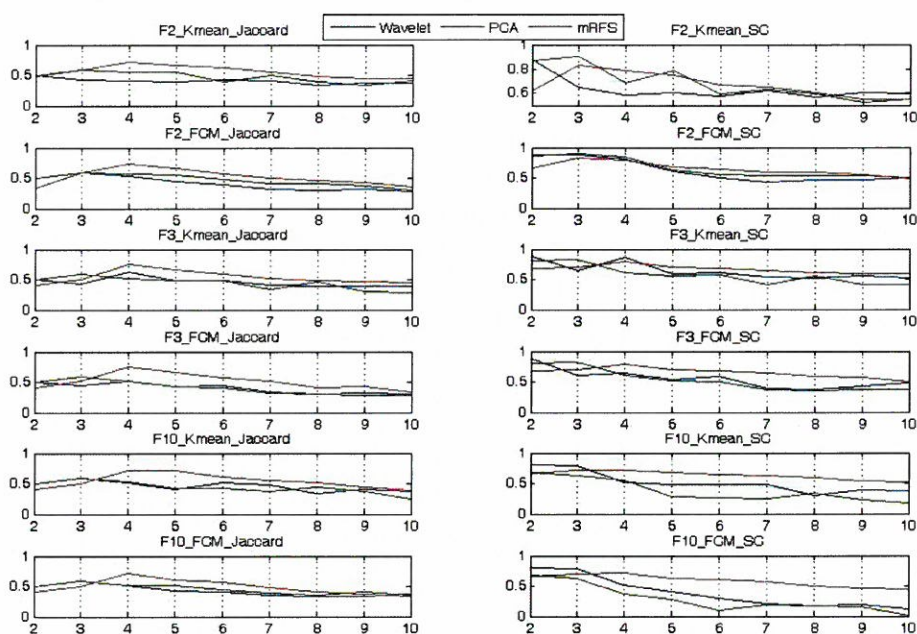

圖四   二個、三個、十個特徵值比較圖

觀察圖四中的 Jaccard 指標，可以發現 mRFS，也就是紅線幾乎都是在其他的線條之上，表示 mRFS 方法在 Kmean 和 FCM 時都有不錯的表現，結合表四的結果，可以驗證出改進後的 mRFS，即採用 KS 挑選特徵值，依然是優於 Wavelet 和 PCA。另外觀察 mRFS 在使用側影係數指標時，產生最高指標值的 x 點，大部分情況都是正確的分群數，即四群時是最好的，由此可驗證 mRFS 的成效。

4.4 真實資料之實驗

　　本文也使用真實資料實驗，我們採用三種不同的特徵選取法，然後使用 SPC 分群演算法。圖五即為實驗結果，左上圖的 Wavelet 和右上圖的 PCA 都只能分成一群，只有左下圖的 mRFS 可以分成兩群。由於左下圖之中央部份，不易觀察其分群情形，因此右下圖為左下圖中央部份的放大情形，圖中可看出其資料分為上下兩群。
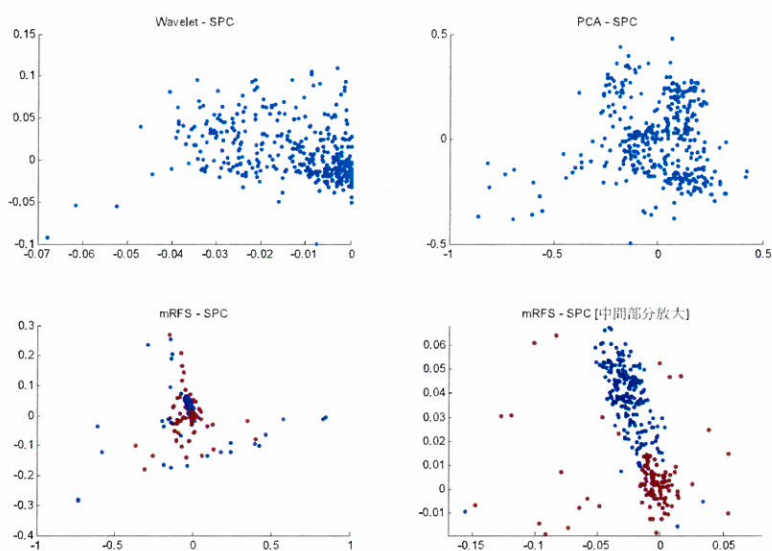
圖五　三個特徵選取法的比較，使用 SPC 分群於萃取兩個特徵值的真實資料
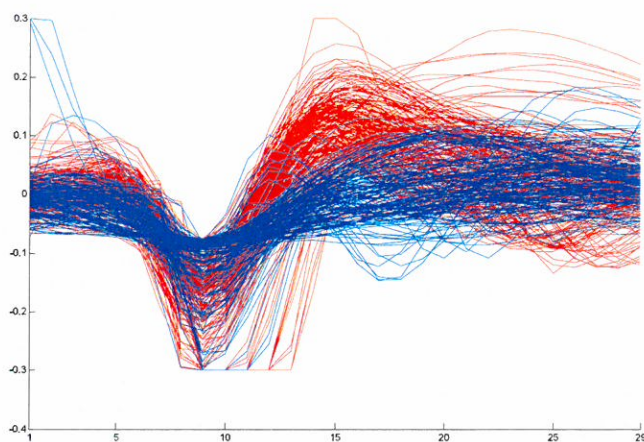
圖六　真實資料採用 mRFS 特徵選取法，並使用 SPC 分群之分類情況

　　爲了更加瞭解真實資料分群的波形分類情況，圖六所示即爲採用 mRFS 特徵選取法，然後採用 SPC 分群的結果，可觀察出對應的兩種波形。

　　爲了比較 mRFS 與其他兩種特徵選取法在不同分群演算法的表現，除了以上實驗是以 SPC 分群外，我們也使用 FCM 與 Kmean 分群。然而 FCM 與 Kmean 不同於 SPC，無法自動決定群數，因此我們在實驗中，設定不同群數參數，以瞭解其分群效果。由於是真實資料，不知其實際分群情形，無法採用 Jaccard 指標值，我們採用側影係數做爲測度指標。表五即爲採用三種特徵選取法，再使用 FCM 和 Kmean 分群，並利用側影係數計算指標值。由表中數據觀察，此真實資料可分成二到三群，或者是四到五群。

　　以上之真實資料實驗採用兩個特徵值，我們也另外進行三個特徵值的實驗。圖七即爲 Wavelet、 PCA 、 mRFS 選用三個特徵值後，再使用 SPC 分群演算法的結果。原本只用兩個特徵值時（圖六），只有 mRFS 可以被 SPC 分成兩群，使用三個特徵值後，Wavelet 和 mRFS 都可以被 SPC 分成兩群，然而 PCA 還是只能分成一群。圖八爲 Wavelet（上圖）和 mRFS（下圖）經過 SPC 分群後，其波形的分群對應情形。

　　對於選用三個特徵值後，除了 SPC 分群之實驗外，我們也使用 FCM 和 Kmean 分群。表六即爲三種特徵選取法使用三個特徵值後，用 FCM 和 Kmean 分群的結果，表中數據爲分群指標之側影係數。

表五　利用側影係數測度三種特徵選取法對於 FCM 和 Kmean 不同群數之分群效果

— 選用兩個特徵值

群數	Wavelet		PCA		mRFS	
	FCM	Kmean	FCM	Kmean	FCM	Kmean
2	0.73	0.73	0.43	0.40	0.22	0.93
3	0.60	0.62	0.52	0.53	0.20	0.95
4	0.46	0.48	0.55	0.57	0.41	0.43
5	0.51	0.49	0.65	0.65	0.50	0.46
6	0.46	0.57	0.60	0.60	0.08	0.44
7	0.49	0.55	0.56	0.57	0.17	0.47
8	0.47	0.58	0.54	0.54	0.12	0.66
9	0.46	0.57	0.51	0.60	0.25	0.51
10	0.45	0.57	0.51	0.54	0.27	0.53
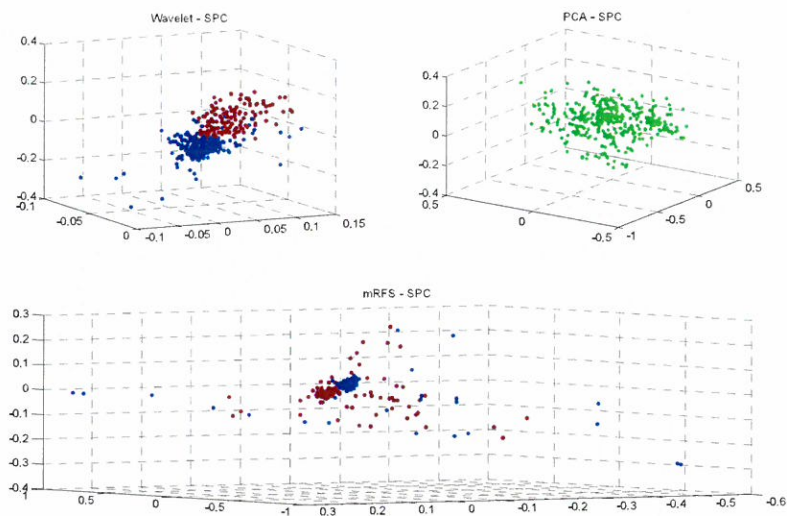
圖七　三個特徵選取法的比較，使用 SPC 分群於萃取三個特徵值的真實資料
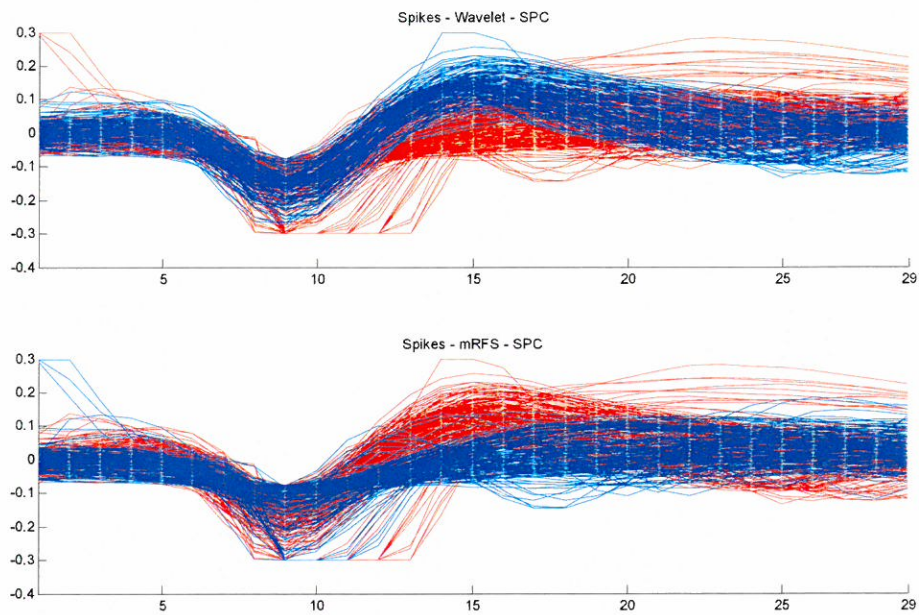
圖八　Wavelet 和 mRFS 經過 SPC 分群後，其波形對應情形

表六　利用側影係數測度三種特徵選取法對於 FCM 和 Kmean 不同群數之分群效果
— 選用三個特徵值

群數	Wavelet		PCA		mRFS	
	FCM	Kmean	FCM	Kmean	FCM	Kmean
2	**0.72**	0.72	0.39	0.46	0.24	0.26
3	0.51	**0.75**	0.47	0.48	0.30	**0.94**
4	0.42	0.63	0.52	0.51	0.28	0.85
5	0.54	0.55	**0.57**	**0.57**	**0.54**	0.54
6	0.49	0.49	0.53	0.54	0.11	0.53
7	0.42	0.51	0.51	0.50	0.10	0.23
8	0.35	0.55	0.48	0.52	0.10	0.48
9	0.31	0.47	0.45	0.53	0.10	0.52
10	0.31	0.44	0.43	0.51	0.15	0.73

5. 結論與未來展望

　　本文探討有關動作電位波型分類的問題，主要描述 mRFS 的方法，除了驗證其成效也延伸其方法。

　　根據實驗結果，三種特徵選取法中，即 mRFS 方法、主成分分析法和基於小波轉換的特徵選取法，無論是 K-mean 和 Fuzzy-C-Mean 及 SPC 分群演算法，在使用具有參考標準答案的 Jaccard 分群指標下，mRFS 特徵選取法都比另外兩種方法更有成效。

　　使用 K-mean 和 Fuzzy-C-Mean 分群演算法時，需要先設定群數，若觀察側影係數指標以決定分群數目時，僅靠側影係數的最佳值，並無法絕對找出最好的對應群數。但我們若根據側影係數的前若干個最佳值，則可指定某一個合理的群數範圍。

　　另外特徵值的選取，可使用 KS test 挑選不同階數的極小極大值。在實驗中，分別使用兩個、三個、十個特徵值做比較，發現三個特徵值的效果最好。同時在以上實驗中，也可以發現 mRFS 的表現一般也比主成分分析及小波轉換好。

　　有關電位波形的分類問題，尚有許多有待探討之處，例如本文並未考慮當棘波發生重疊的情況，還有一些生物上的特性，例如動作電位的「絕對不反應期」，這和棘波的發生位置有關，這些問題在本文中都未加考慮，往後的研究可以往這些方向邁進。

參考文獻

[Blatt96]　　　M. Blatt, S. Wiseman and E. Domany, "Super-paramagetic clustering of data", Phys. Rev. Lett., No. 76, pp. 3251-3254, 1996.

[Greene04]　　D. Greene, A. Tsymbal, N. Bolshakova, and P. Cunningham, "Ensemble clustering in medical diagnostics", In Proc. 17th IEEE Symposium on Computer-Based Medical Systems (CBMS'04), pp. 576-581, 2004.

[Letelier00]　　Juan C. Letelier and Pamela P. Weber, "Spike sorting based on discrete wavelet transform coefficients", Journal of Neuroscience Methods, Vol. 101, pp. 93-106, 2000.

[Marsaglia03]　G. Marsaglia, W. Tsang and J. Wang, "Evaluating Kolmogorov's distribution", Journal of Statistical Software, Vol. 8, issue 18, 2003.

[Othman05]　　Mazin Z. Othman, Maan M. Shaker and Mohammed F. Abdullah, "EEG spikes detection, sorting, and localization", Proceedings of World Academy of Science, Engineering and Technology (PWASE), Vol. 9, pp. 205-208, 2005.

[Quiroga04]　　R. Quian Quiroga, Z. Nadasdy and Y. Ben-Shaul, "Unsupervised spike detection and sorting with wavelets and superparamagnetic clustering.", Neural Computation, No. 16, pp. 1661-1687, 2004.

[Rinberg03]　　D. Rinberg, W. Bialek, H. Davidowitz and N. Tishby, "Spike sorting in the frequency domain with overlap detection", arXiv: physics/0306056v2, 2003.

[Tan05]　　　　Pang-Ning Tan, Michael Steinbach and Vipin Kumar, "Introduction to Data Mining", Addison-Wesley, ISBN: 0321321367, pp. 541-542, 2005.

[Yen08]　　　　Chien-Chang Yen, Wei-Chang Shann, Chen-Tung Yen and Meng-Li Tsai, "Spike sorting by a minimax reduced feature set based on finite differences", J Physiol Sci, No. 59, pp. 143–147, 2009.

Spike Sorting Using a Finite-Difference-Based Method

Wen-Bin Lin[1], Grace J. Hwang[1]   and Chien-Chang Yen[2]

Fu Jen Catholic University Taipei, Taiwan 242, R.O.C

Abstract

In neurophysiology, a neuron is the basic unit in a nervous system. The main function of an action potential or a spike is to transmit messages between neurons. The spikes can be recorded as shapes of waveforms, and the techniques of spike sorting are to distinguish different shapes of waveforms among spikes. In this paper, we focus on the study of feature selection, which is one of the data pre-processing steps of the spike sorting. The use of the feature selection is not only to select the significant features from the dataset but also to reduce the dimension of features.

In this article, we mainly study the Min-max Reduced Feature Set (mRFS) proposed by Yen et al. The mRFS is designed particularly for choosing a pair of features from spike data, and the idea of the method is based on the technique of the finite difference with various orders. We first introduce the mRFS method and then compare its performance with two other techniques, Principal Component Analysis (PCA) and a wavelet transform method. Experimental results show that mRFS is the most efficient method among three.

The mRFS method is also extended in our study, unlike the original mRFS only choosing two features. We apply Kolomogorov-Smirnov test to choose any number of main features. The other extension of mRFS is that we use silhouette coefficient as a cluster validity measure and attempt to

---

[1] Department of Computer Science and Information Engineering
[2] Department of Mathematics

suggest the possible numbers of clusters on the data after mRFS has processed. The validity of both extensions is also demonstrated through the numerical experiments.

Multiscale Decomposition for Nonstationary Data –
Á Trous Wavelets and Empirical Modal Decomposition

[+]Grace J. Hwang, [*]Yeah-Chuan Kuo, [*]Nanping Yang[1] and [*]Chien-Chang Yen

[+]*Department of Computer Science and Information Engineering, Fu Jen Catholic University*

[*]*Department of Mathematics, Fu Jen Catholic University*

Abstract

We present a multiscale decomposition for nonstationary data, which is a unified framework of the empirical modal decomposition (EMD) and á trous wavelets (AWT). The boundary effects due to EMD are either by taking local extreme values or extrapolation values at the endpoints. A comparison between AWT and EMD is presented according as a one/two modal signal, a linear function with two modal signal, and a random signal. Both AWT and EMD are applied on structure detection of astronomical observations.

Keywords : multiscale decomposition, nonstationary data, á trous wavelet, empirical modal decomposition

Section 1.   Introduction

Nonstationary data can be found in various fields, for example, fusion in biological images, structure detections in astronomical observations, and financial stock markets. To deal with nonstationary data, a suitable decomposition is often applied so that the significant information is able to be probed for further analysis.

---

[1] Corresponding author: Tel :886-2-2905-3545
                      Fax :886-2-2904-4509
E-mail address: yang@math.fju.edu.tw

Empirical modal decomposition (EMD) is a method for analyzing nonstationary and nonlinear datasets. It provides a tool to decompose signals into a combination of bases or intrinsic modal functions (IMFs). It is data-driven and has a lower computational complexity with highly effective. This method has been used in numerous fields [5].

It is well-known that wavelets is a tool for a multiscale analysis [4]. There are many types of wavelets that are often used, such as, Daubechies' orthogonal wavelets (Daub) [4], Chui-Wang wavelets (CW)[1], Cohen-Daubechies-Feauveau wavelets (CDF) [3], difference wavelets (Diff) [2], or á trous wavelet (AWT). From the empirical experience, the Daub, CDF, CW and DW are very successful for data compression. However, AWT is better than others in imaging analysis, even when the data is nonstationary. AWT may also be employed on astronomical observations [6].

In section 2, we present two aforementioned methods in a unified frame, called a multiscale decomposition. A comparison between AWT and EMD is investigated for different types of signals in section 3. Section 4 describes an application of AWT and EMD to astronomical observations. A short summary is given in the last section.

Section 2.   Multiscale Decomposition

Let J be a positive integer. A multiscale decomposition for a signal U_0 can be written as

$$U_0 = \sum_{j=1}^{J} W_j + R_{J+1},\tag{1}$$

where W_j is the signal at scale j or at the j-th plane and R_{J+1} is the last plane or the smooth plane. Equation (1) is a unified framework for AWT and EMD described below.

Denote $*$ the convolution operator and define the cubic B-spline function as

$$B_3(x) = B_1 * B_1 * B_1(x)$$

where $B_1(x)$ is the box function on $[0,1]$, that is,

$$B_3(x) = \begin{cases} \dfrac{x^3}{6}, & x \in [0,1] \\ -\dfrac{x^3}{2} + 2x^2 - 2x + \dfrac{2}{3}, & x \in [1,2], \end{cases}$$

and it is symmetric with respect to $x = 2$. By the definition of $B_3(x)$, we have

$$B_3(x) = \frac{1}{8}B_3(2x) + \frac{4}{8}B_3(2x-1) + \frac{6}{8}B_3(2x-2) + \frac{4}{8}B_3(2x-3) + \frac{1}{8}B_3(2x-4). \quad (2)$$

Besides the property shown in equation (2), a cubic *B*-spline has the nice features of a short length of coefficients, smoothness, and symmetry. We therefore choose it to derive the formula of the á trous algorithm and use it to interpolate the local maxima or minima in the EMD.
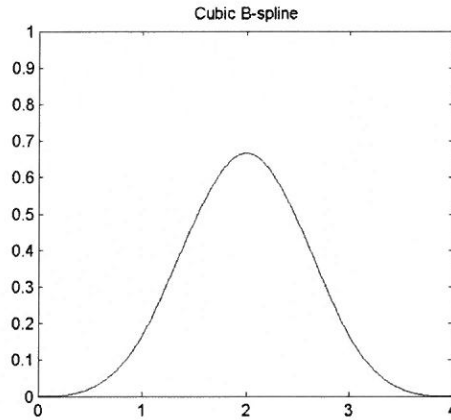

Figure 1.　The Cubic B-spline function.

2.1 Á trous Wavelet

A signal decomposition by AWT is given by

$$c_{j,k} = \ <f(2^j(x+2)-k), B_3(x)> \quad (3)$$

$$w_{j+1,k} = c_{j,k} - c_{j+1,k}$$

The coefficients $w_{j+1,k}$ lies on the ($j+1$)-th wavelet plane and the smooth plane is referred to $c_{j,k}$. We now apply equation (3) to deduce the coefficients c_{j+1} in terms of c_j as follows.

$$c_{j+1,k} = <f(2^{j+1}(x+2)-k), B_3(x)>$$

$$= \int 2^{-j-1} f(x) B_3(2^{-(j+1)}(x+k)-2)dx$$

$$= \int 2^{-j-1} f(x)(\frac{1}{8}B_3(2^{-j}(x+k)-4)+\frac{4}{8}B_3(2^{-j}(x+k)-3)+\frac{6}{8}B_3(2^{-j}(x+k)-2)$$

$$+\frac{1}{8}B_3(2^{-j}(x+k)-1)+\frac{4}{8}B_3(2^{-j}(x+k)))dx$$

$$=\frac{1}{16}\int f(2^j(x+2)-(k-2\cdot2^j))B_3(x)dx + \frac{4}{16}\int f(2^j(x+2)-(k-2^j))B_3(x)dx$$

$$+\frac{6}{16}\int f(2^j(x+2)-k)B_3(x)dx + \frac{4}{16}\int f(2^j(x+2)-(k+2^j))B_3(x)dx$$

$$+\frac{1}{16}\int f(2^j(x+2)-(k+2\cdot2^j))B_3(x)dx$$

$$=\frac{1}{16}c_{j,k-2\cdot2^j}+\frac{4}{16}c_{j,k-2^j}+\frac{6}{16}c_{j,k}+\frac{4}{16}c_{j,k+2^j}+\frac{1}{16}c_{j,k+2\cdot2^j}$$

It is worthwhile to note that the above formula is different to the wavelet transformation. The perfect reconstruction of the given signal can be obtained by adding all wavelet planes.

A data $\{c_{0,k}\}$ is given as $c_{0,k} = \sin(x_k)$, where $x_k = k\frac{2\pi}{256}$ for $k = 1, 2, \ldots, 256$. With the periodic boundary conditions imposed, the smooth planes and the wavelet planes obtained via AWT are shown in Figure 2.
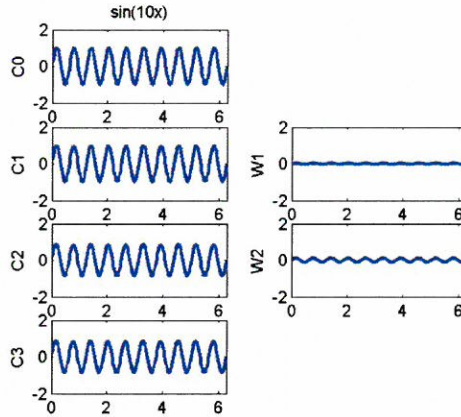

Figure 2. This figure demonstrates the process of AWT. The profiles on the left column are the smooth planes and the wavelet planes are given on the right column.

2.2 Empirical Modal Decomposition

There are some characterizations when empirical modal decomposition is applied to signals analysis. First of all, there are at least one minimum and at least one maximum. Secondly, the characteristic time scale is defined by the time lapse between the extrema. Finally, if the signal is totally devoid of extrema but contained only inflection points, it can be differentiated once or more times to reveal the extrema [5]. To decompose a signal s_0 into IMFs, interpole by a cubic B-spline $B_3(x)$ to s_0 at its local maxima to obtain an envelope t_0^{max} as shown in Figures 3(b) and 3(c), the same interpolation at local minima to obtain another envelope t_0^{min} as shown in Figure 3(d). Let $t_0 = \frac{1}{2}(t_0^{max} + t_0^{min})$ and $u_0 = s_0 - t_0$. Define

$$SD = \| s_0 - t_0 \| / \| s_0 \| = | u_0 | / \| s_0 \|.$$

An IMF $W_1 = u_0$ is obtained if it satisfies the stop criterion on SD. If not, replace s_0 by u_0 and repeat the above process until IMF is obtained. The initial signal for the next IMF is $s_1 = s_0 - W_1$. The algorithm is laid out in Table 1, and the process is called the shifting process. Figure 4 demonstrates EMD for a sine wave which is decomposed into two IMFs.
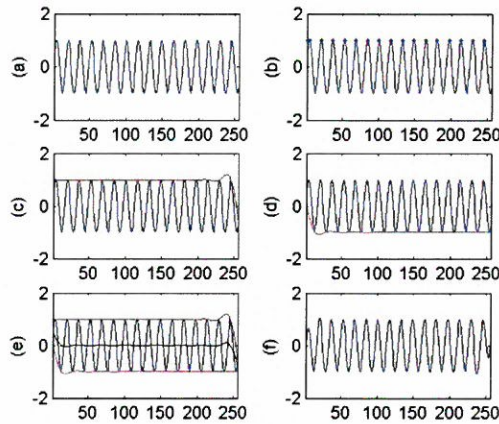

Figure 3. This figure demonstrates the shifting process of EMD. The profile (a) is the given signal.The profile (b) shows the local maxima and (c) is the envelope t_0^{max}. The envelope t_0^{min} for local minima is in profile (d). The profile (e) shows the average $t_0 = \frac{1}{2}(t_0^{max} + t_0^{min})$ and the profile (f) is the difference u_0.
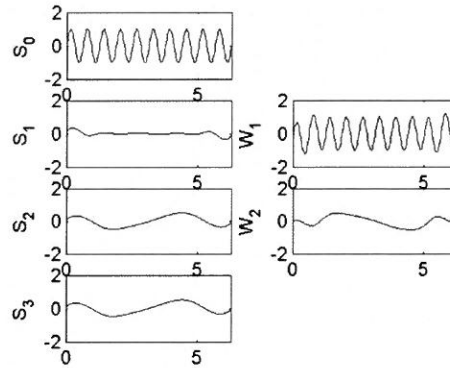
Figure 4.   Each profile on the left column shows the initial signal in each shifting process and their IMFs are on the right column.

$$initial\ data\quad X,\ d$$
$$SD = d+1;$$
$$while\ SD>d$$
$$\quad find\ h\ from\ X,$$
$$\quad SD = \ sum((h(i)/X(i))\wedge 2)$$
$$\quad X = \ X-h$$
$$end$$
$$IMF = X;$$

Table 1.   The algorithm for the shifting process

To avoid overshooting too much on the boundaries, it needs a careful treatment at them when the shifting process is performed. One way is to impose the boundary values as the interpolation points to get envelopes as shown in Figure 5(a). On the other hand, for example, to consider t_0^{max}, we use the existed or the nearest local maximum value as the interpolation point as shown in Figure 5(b). The latter demonstrates the better performance than the former does.
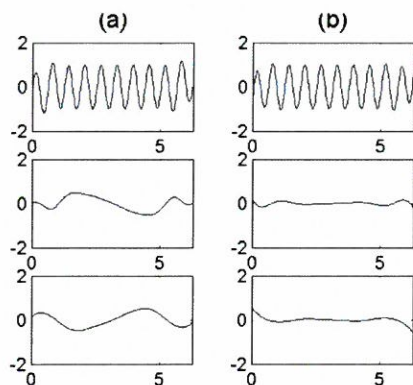
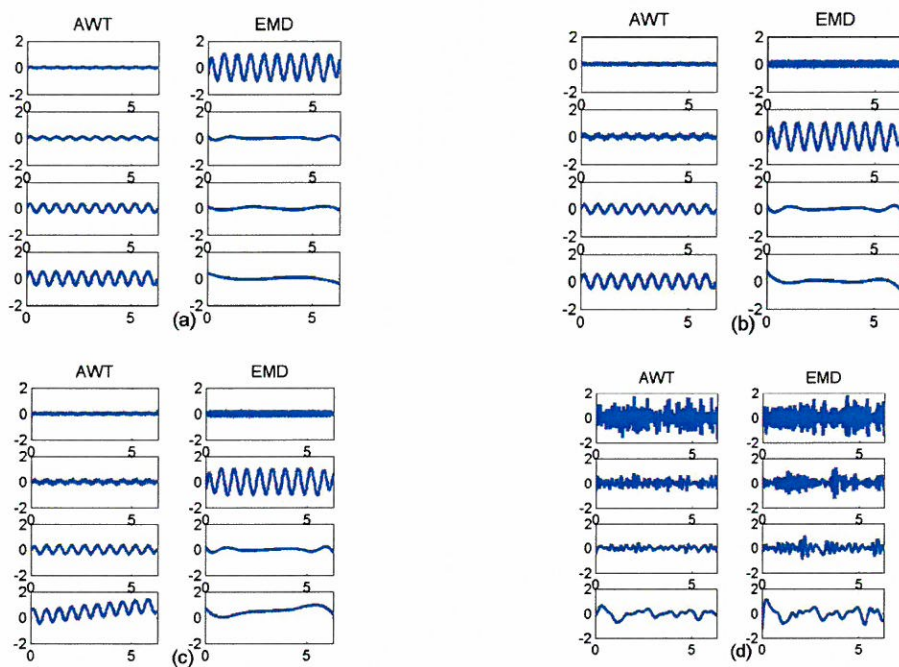Figure 5.   A comparison of boundary effects between two different boundary treatments.

Figure 6.   There are four typical types to investigate the performance of AWT and EMD.

Section 3. A comparison between AWT and EMD

To compare the effects, between AWT and EMD, four types of signals are selected, namely, a one signal $\sin(10x)$, a two modal signal $\sin(10x)+0.25\sin(40x)$, a linear function

with two modal signal $\sin(10x) + 0.25\sin(40x) + \dfrac{x}{2\pi}$, and a random signal. For each type of signal, use AWT to get four wavelet planes and use EMD to get four IMFs with local extreme boundary treatment. The results are shown in Figure 6. The profiles on left and right columns to each type of signals are effects of AWT and EMD, respectively. Each column comprises decompositions from finest to coarsest.

By all profiles shown in Figure 6, the observations are summarized as the following.

(i)   The one modal signal is the simplest one that every one has to know and easy to observe the effects. The concept of multiscale decomposition is a good one that applies to two modal signals. The random signal is accompanied with all kinds of signals.

(ii) EMD is powerful for all types of signals, at least, very effective for types (a) to (c). The only flaw for IMFs is not completely resolved due to boundary effect.

(iii) The AWT sounds not good in dealing with signal decompositions comparing to EMD. It even not completely resolves some certain scales.

Section 4. An Application

The structures of central regions of galaxies using AWT was studied extensively. The results shows that some major spiral arms outside can go all the way into the central regions and some galaxies have bars in the nuclear center. These results are important for us to understand the starburst and AGN phenomena, see [6].

Now, we focus our efforts on the studies of methods for astronomical observations. We take an astronomical image NGC 2903 shown in Figure 7 to compare AWT and EMD.
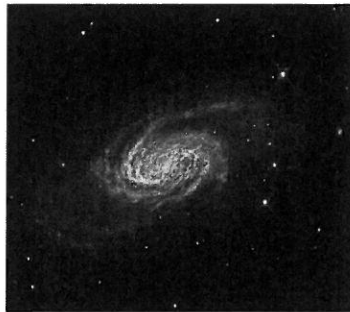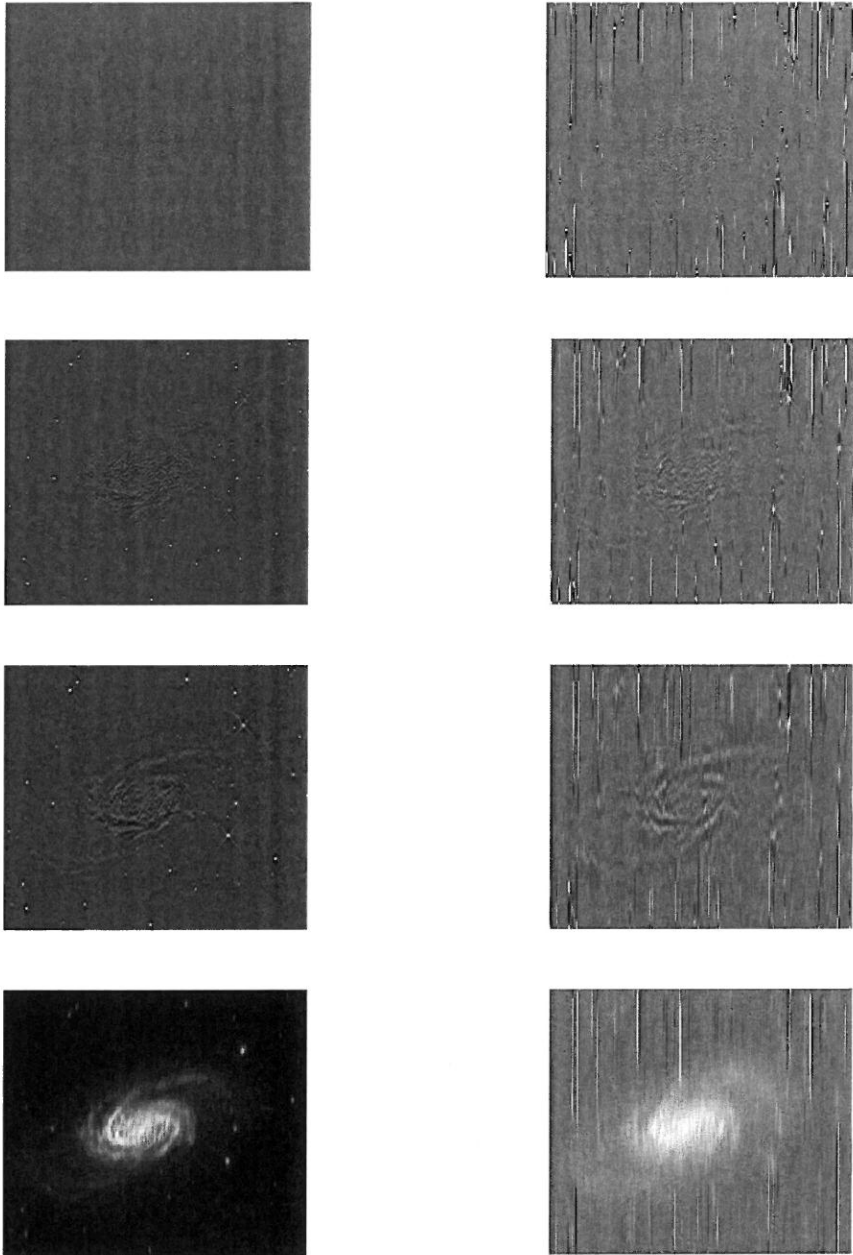

Figure 7. Galaxy NGC 2903.

Figure 8.　These figures demonstrate the results of AWT (left column) and EMD (right column). The results shows that the structures decomposed by AWT and EMD are similar.

To deal with two-dimensional images, the tensor product is used. EMD needs to append zeros when the IMF does not reach the decomposition level. We observe that the behavior of EMD and AWT are about the same as shown in Figure 8. The left and right column of Figure 8 shows the effects of AWT and EMD, respectively. The result of EMD is required to be moderated by grayscale and the clean images should be further studied.

Section 5. Conclusion

We proposed a unified framework of mutiscale decomposition in this article. It was shown that AWT and EMD are effective to deal with nonstationary data. We applied AWT and EMD on structure detections of galaxies, their behavior are very similar. Moreover, we provided and investigated two different boundary treatments for EMD.

From our numerical comparisons, AWT seems to be more suitable in time domain and EMD sounds more effective in frequency domain.

References

[1]   C.K. Chui, *An introduction of wavelets*, Academia Press, New York, 1992.

[2]   I.L. Chern and C.C. Yen, Difference wavelet---Theory and a comparison study, Methods and Appl. of Analysis, 9 (2002), 469.

[3]   A. Cohen, I. Daubechies and J. Feauveau, Biorthogonal bases of compactly supported wavelets, Comm. Pure Appl. Math, 45 (1992), 485.

[4]   I. Daubechies, *Orthonormal bases of compactly supported wavelets*, Comm. Pure Appl. Math., 41 (1988), 909-996.

[5]   N.E. Huang *et al*, The empirical mode decomposition and the Hilbert spectrum for nonlinear and non-stationary time series analysis, Proc. R. Soc. Lond. A 454 (1998), 903-995.

[6]   C.C. Yen, C. Yuan and I.H. Li, *Application of wavelet methods to the detection of galactic central structures*, Fu Jen Studies-Science and Engineering, 38 (2004), 251-261.

非穩定資料的多重尺度分解法–小波與經驗模態分解法

黃貞瑛

輔仁大學資工系

郭曄銓　　楊南屏　　嚴健彰

輔仁大學數學系

摘　　要

　　本論文應用小波與經驗模態分解法於非穩態資料，並提出多重解析的一致表示法。應用經驗模態分解法需考慮邊界為其局部極值或外插值。透過單一頻率、複合頻率、線性函數與複合頻率、及雜訊等訊號，我們比較小波與驗模態分解法的多重解析效果，進而將兩種方法應用於天文觀測，並作實際應用之比較。

關鍵字：多重解析法、非穩態資料、小波、經驗模態分解法